

NUMERICAL ESTIMATION OF SLIPSTREAM CHARACTERISTICS FOR
PROPELLERS OPERATING AT LOW REYNOLDS NUMBERS

A Thesis by

Ramya Bhavana Pampala

Bachelor of Technology, Institute of Aeronautical Engineering, 2013

Submitted to the Department of Aerospace Engineering
and the faculty of the Graduate School of
Wichita State University
in partial fulfillment of
the requirements for the degree of
Master of Science

July 2019

© Copyright 2019 by Ramya Bhavana Pampala

All Rights Reserved

NUMERICAL ESTIMATION OF SLIPSTREAM CHARACTERISTICS FOR
PROPELLERS OPERATING AT LOW REYNOLDS NUMBER

The following faculty members have examined the final copy of this thesis for form and content, and recommend that it be accepted in partial fulfillment of the requirement for the degree of Master of Science with a major in Aerospace Engineering.

Klaus. A. Hoffmann, Committee Chair

Gerardo Olivares, Committee Member

Gisuk Hwang, Committee Member

DEDICATION

To my parents, brothers and Lucky

ABSTRACT

An accurate estimation of propeller slipstream characteristics is essential to evaluate the performance characteristics of airframe components placed within the propeller slipstream. The complicated vortical structures of the propeller slipstreams necessitate the need of using high-fidelity methods such as computational fluid dynamics (CFD) analysis to estimate the slipstream characteristics. The current investigation deals with comparing the CFD predicted propeller thrust, power and slipstream characteristics with the wind tunnel data for a variable pitch propeller operating at a low Reynolds number of approximately 100,000.

In the current study, the CFD solver used was ANSYS Fluent software. Initial numerical analyses were conducted to evaluate the applicability of intermittency transition model available in the solver, to low Reynolds number flows. For assessment purposes, the Eppler 387 airfoil characteristics obtained using XFOIL (low-fidelity code) and time-accurate CFD calculations were compared with wind tunnel data. When compared to XFOIL drag data, the intermittency model had a better quantitative agreement with wind tunnel data at moderate angles of attack. Subsequently, three-dimensional time-accurate CFD simulations were conducted using the intermittency model to estimate the propeller characteristics. The propeller rotational motion was simulated using the sliding mesh approach. The numerical results for parameters such as thrust and nacelle pressures which are dependent only on pressure fields, have a good agreement with wind tunnel data. Whereas, propeller power and slipstream velocities which are based on both pressure and viscous forces are slightly under predicted in the numerical simulations.

TABLE OF CONTENTS

Chapter	Page
1. INTRODUCTION	1
2. PROPELLER TORQUE EFFECTS	6
2.1 Torque Reaction of Engine and Propeller	7
2.2 Gyroscopic Precession	8
2.3 P-Factor	10
2.4 Slipstream.....	11
3. LITERATURE REVIEW	14
3.1 Propeller Low-Fidelity Methods.....	15
3.2 Propeller-Airframe Components Combination	18
3.2.1 Low-Fidelity Methods.....	18
3.2.2 High-Fidelity Methods.....	21
3.2.3 Hybrid Methods	25
3.2.4 Surrogate Methods.....	28
4. OBJECTIVE.....	33
5. THEORETICAL BACKGROUND.....	35
5.1 Propeller Aerodynamic Characteristics	35
5.2 XFOIL	38
5.3 Computational Fluid Dynamics	39
6. NUMERICAL ANALYSIS AND RESULTS.....	43
6.1 Eppler 387 Airfoil	43
6.1.1 XFOIL	46
6.1.2 Computational Fluid Dynamics.....	47
6.1.3 Comparison of Results	60
6.2 COMP Propeller.....	69
6.2.1 Propeller Geometry	69
6.2.2 Secondary Characteristics Measurement Locations	70
6.2.3 Computational Fluid Dynamics.....	73
6.2.4 Comparison of Results	97
7. CONCLUSIONS AND FUTURE WORK.....	118
REFERENCES.....	122

LIST OF FIGURES

Figure	Page
1. Propeller torque reaction yaw moments.	7
2. Propeller gyroscopic effects yaw moments.	9
3. Propeller slipstream yaw moments.....	12
4. Propeller aerodynamic characteristics classification.....	35
5. Eppler 387 airfoil.....	45
6. Numerical model details for Eppler 387 airfoil CFD analysis.....	48
7. Static pressure contour at $\alpha = 4^\circ$	48
8. Eppler 387 airfoil and size box dimensions.	49
9. Schematic of mesh refinement level for Eppler 387 airfoil.....	49
10. Schematic of grid resolutions used for Eppler 387 grid independence study.....	53
11. Time convergence history of laminar model results at $\alpha = 4^\circ$	55
12. Time convergence history of intermittency model results at $\alpha = 4^\circ$	55
13. Time convergence history of k- ω SST with low Reynolds number corrections results at $\alpha = 4^\circ$	55
14. Grid independence study results at $\alpha = 4^\circ$ using intermittency model.	56
15. Grid independence study results at $\alpha = 11^\circ$ using intermittency model.	57
16. Time-step independence study results at $\alpha = 4^\circ$ with medium mesh and intermittency model.	59
17. Variation of Eppler 387 lift coefficient with angle of attack.....	60
18. Variation of Eppler 387 drag coefficient with angle of attack.	60
19. Variation of Eppler 387 pitching moment coefficient with angle of attack.	61
20. X-velocity contours at 0.1 seconds.....	63
21. X-velocity contours at 0.2 seconds.....	64

LIST OF FIGURES (continued)

Figure	Page
22. X-velocity contours at 0.3 seconds.	65
23. Laminar separation bubble on Eppler 387 airfoil.	66
24. Pressure coefficient distributions at 0.1,0.2, and 0.3 seconds.	67
25. COMP geometry.	70
26. Sign conventions for propeller secondary characteristics provided in Reference [15].	70
27. Nacelle pressure measurement locations.	71
28. Slipstream velocity measurement stations.	73
29. Numerical model details for COMP propeller CFD analysis.	74
30. Schematic of fluid domains for sliding mesh technique.	75
31. Rotating fluid domain components and extents.	76
32. Size boxes to capture propeller wake.	77
33. Propeller blade orientation angle.	81
34. Schematic of surface mesh associated with medium mesh.	83
35. Comparison of grid resolution in propeller-wake region.	84
36. Schematic of volume cells transition in medium mesh.	85
37. Time history of propeller thrust variation at $J = 0.67$	86
38. Time history of propeller torque variation at $J = 0.67$	86
39. Variation in thrust force with varying mesh sizes.	87
40. Variation in torque moment with varying mesh sizes.	88
41. Computation time for the three meshes in the grid independence study.	88
42. Comparison of nacelle pressure distribution at station NP_1.	89
43. Comparison of axial slipstream velocity at station SV_1a.	89

LIST OF FIGURES (continued)

Figure	Page
44. Comparison of tangential slipstream velocity at station SV_1a.	90
45. Comparison of radial slipstream velocity at station SV_1a.	90
46. Axial slipstream velocity distribution with wall surface velocity.	93
47. Axial slipstream velocity distribution without wall surface velocity.	93
48. Variation of nacelle pressure during the 8 th rotation at station NP_1.	94
49. Variation of axial slipstream velocity during the 8 th rotation at station SV_1a.	95
50. Variation of tangential slipstream velocity during the 8 th rotation at station SV_1a.	95
51. Variation of radial slipstream velocity during the 8 th rotation at station SV_1a.	96
52. Different flow regions on the propeller blade – isometric view.	96
53. Different flow regions on the upper and lower surfaces of the propeller blade.	97
54. Variation of thrust coefficient with advance ratio.	98
55. Variation of power coefficient with advance ratio.	98
56. Static pressure contour on XZ plane at y = 0 m.	99
57. Nacelle pressure distribution at station NP_1.	100
58. Nacelle pressure distribution at station NP_2.	100
59. Nacelle pressure distribution at station NP_3.	101
60. Nacelle pressure distribution at station NP_4.	101
61. Propeller vorticity visualization.	102
62. Tangential velocity contour on YZ plane at x = 0.014 m.	103
63. Schematic of tangential velocity gradients due to propeller vortex.	103

LIST OF FIGURES (continued)

Figure	Page
64. Axial velocity contour on XZ plane at $y = 0$ m.....	104
65. Radial velocity contour on YZ plane at $x = 0.014$ m	104
66. Comparison of slipstream velocities at station SV_1a.	106
67. Comparison of slipstream velocities at station SV_1b.	106
68. Comparison of slipstream velocities at station SV_1c.	107
69. Comparison of slipstream velocities at station SV_2a.	108
70. Comparison of slipstream velocities at station SV_2b.	108
71. Comparison of slipstream velocities at station SV_2c.	109
72. Comparison of slipstream velocities at station SV_3a.	110
73. Comparison of slipstream velocities at station SV_3b.	110
74. Comparison of slipstream velocities at station SV_3c.	111
75. Swirl angles at $x/L = 0.02$	115
76. Swirl angles at $x/L = 0.49$	116
77. Swirl angles at $x/L = 0.84$	116

LIST OF TABLES

Table	Page
1. Comparison of Different Numerical Approaches in Reference [38]	21
2. Mesh Details in Reference [39].....	23
3. Discretization Schemes Used in Reference [39].....	23
4. Mesh and Solver Details in Reference [41]	27
5. Discretization Schemes Used in Reference [41].....	27
6. Boundary Conditions for Eppler 387 CFD Analysis	51
7. Courant Number and Relaxation Factors for Eppler 387 CFD	52
8. Details of Meshes Used in Eppler 387 Grid Convergence Study.....	54
9. Nacelle Pressure Measurement Stations	71
10. Slipstream Velocity Measurement Stations	72
11. Details of Meshes Used in Propeller Grid Convergence Study.....	83

LIST OF NOMENCLATURE

BEM	Blade Element Momentum
CFD	Computational Fluid Dynamics
LSB	Laminar Separation Bubble
LTPT	Low Turbulence Pressure Tunnel
MRF	Moving Reference Frame
NP	Nacelle Pressure
RANS	Reynolds-Averaged Navier-Stokes
RPM	Rotations Per Minute
SV	Slipstream Velocity
UAV	Unmanned Aerial Vehicle
URANS	Unsteady Reynolds-Averaged Navier-Stokes
VLM	Vortex Lattice Method

LIST OF SYMBOLS

\vec{h}	Propeller angular momentum
ω_x	Propeller angular velocity
$\vec{\omega}_p$	Angular velocity of precession
$I_{(xx)prop}$	Propeller moment of inertia about x-axis
\vec{M}_p	Gyroscopic moments
p_p, q_p, r_p	Aircraft rotation rate about x, y and z-axis respectively
N_p	Propeller yawing moment at high angles of attack
σ	Propeller solidity
q	Dynamic pressure
A	Propeller disk area
R	Radius of propeller blade
J	Propeller advance ratio
\bar{C}_l	Average section lift coefficient
a	Section lift-curve slope
C_d	Drag coefficient
α	Angle of attack
C_T	Propeller thrust coefficient
C_{pow}	Propeller power coefficient
T	Propeller thrust generated
P	Propeller power required
ρ	Fluid density

LIST OF SYMBOLS (continued)

n	Propeller rotational speed in rotations per second
D	Propeller diameter
U	Freestream velocity
Re	Propeller Reynolds number
V_t	Propeller tangential velocity at 0.75 R
c	Airfoil chord length
$c_{0.75}$	Propeller chord length at 0.75 R
μ	Fluid dynamic viscosity
$r_{0.75}$	Propeller radius at 0.75 R
ω	Propeller rotational velocity in radians per second
Φ	Azimuth angle
x	Longitudinal distance from nacelle leading edge
L	Nacelle length
r	Radial distance from COMP x-axis
C_p	Pressure coefficient
P	Local static pressure
P_∞	Freestream static pressure
u_x	Local axial velocity
u_t	Local tangential velocity
u_r	Local radial velocity
ε	Swirl angle

CHAPTER 1

INTRODUCTION

An advancing propeller technology has led to a significant increase in demand for propellers in the aircraft and unmanned aerial vehicle (UAV) industries. In the aircraft industry, for low speed aircraft, there is a recurring interest in using propellers for generating thrust due to its higher fuel efficiency compared to jet engines [1],[2]. In the case of rotor type UAV, propellers are used to generate thrust in the vertical direction as well as in the direction of flight; whereas for fixed-wing type UAV, propellers can be used for thrust in the direction of flight. In addition to aviation industry, a significant propeller research is being carried out in the marine and wind turbine industries as well. Due to the various applications of propellers, there is a continuous effort in understanding propeller aerodynamics in different flight regimes.

One of the major consequences of installing propellers on an aircraft/UAV is the presence of propeller slipstream. Slipstream is the rotating flow with increased velocities (axial and swirl) behind an operating propeller. For fixed-wing aircraft and UAV, the slipstream plays a significant role in aerodynamic interactions between propeller and airframe components [1],[3],[4]. For rotor type UAV, as propellers provide thrust in both vertical and direction of flight, the slipstream affects flight handling qualities along with aerodynamic characteristics.

The aerodynamic characteristics of any object can be obtained by solving the governing equations of fluid dynamics (continuity, momentum and energy equations). These governing equations can be solved using either low-fidelity or high-fidelity methods. In the case of propellers, the primary aerodynamic characteristics are thrust

generated, power required and efficiency. Slipstream velocity is an example of secondary propeller aerodynamic characteristics. These propeller aerodynamic characteristics are obtained using either low-fidelity or high-fidelity methods.

The term “low-fidelity methods” represents a very generalized term. A large variety of low-fidelity methods exist for different airframe components. Examples of low-fidelity methods include semi-empirical methods such as Allen’s or Jorgensen’s method used for predicting fuselage aerodynamic characteristics and potential flow methods such as lifting line theory for predicting wing aerodynamic characteristics [5],[6],[7].

The low-fidelity methods for propellers include potential flows methods and blade element theory. In potential flow methods, the flow is assumed to be steady, inviscid, incompressible and irrotational. These methods solve the simplified form of Navier-Stokes equations analytically to predict a propeller’s primary and secondary characteristics. Examples of potential flow methods for propellers are momentum theory, lifting line theory, lifting surface theory and panel methods. The blade element theory is an interpolation method that calculates only the primary aerodynamic characteristics of the propeller, based on two-dimensional (airfoil) aerodynamic data of airfoil sections at different stations along the propeller blade radius. As blade element theory cannot predict secondary aerodynamic parameters, this theory is generally coupled with other potential flow methods [8]. The most commonly used coupled method is the blade element momentum (BEM) theory, which is a combination of blade element theory and momentum theory.

The high-fidelity methods are computational fluid dynamics (CFD) methods, which directly solve the full Navier-Stokes equations using various numerical approaches. For

any object, if the geometry, mesh and CFD solver settings are well described, an unsteady Reynolds-averaged Navier-Stokes (URANS) CFD simulation provides a detailed and accurate propeller aerodynamic characteristics compared to low-fidelity methods [8]. However, this improved accuracy comes at an increased computational cost.

Propeller flow field interaction with airframe components is usually complex and unsteady in nature [9]. Although low-fidelity methods are limited due to the use of simplified models, there is an extensive literature available demonstrating the use of low-fidelity methods for both propellers and airframe components with steady-state as well as unsteady approaches to rapidly estimate the effect of slipstream on airframe components [10],[11]. However, a time-accurate CFD analysis can capture more details of the unsteady interaction of propeller with airframe components when compared to low-fidelity methods. In case of propeller CFD analysis, a fine mesh is required to represent the propeller blades accurately. In addition, the time-step value used in the analysis is limited to the amount of time required for rotating the propeller by 1° based on the propeller rotation speed [12]. These mesh and time-step requirements make CFD propeller-airframe simulations computationally expensive.

Hybrid methods have been developed to overcome the large computation times and mesh requirements associated with CFD analysis. In terms of propeller-airframe analysis, these methods attempt to incorporate the computational efficiency of low-fidelity methods and accuracy of CFD simulations. In the CFD simulation of hybrid method, the propeller geometry is replaced by a flat disk and the primary aerodynamic results obtained using low-fidelity methods for propellers are specified as source terms in the momentum

equation. This approximation of propeller geometry eliminates the tedious effort of meshing the propeller as well as the simulation of mesh motion.

In recent development, surrogate modeling is also used as an alternative to hybrid methods to achieve computational efficiency and accuracy simultaneously. In surrogate modeling, the propeller characteristics trained from unsteady CFD simulations are provided as momentum source terms in steady-state CFD simulations. Therefore, the surrogate modeling methods will inherently be more accurate than hybrid methods. However, this additional accuracy is at the expense of reduced computational efficiency compared to hybrid methods, as training the source terms from unsteady CFD simulations is expensive.

A brief literature review provided in Section 3.2, indicates the limitations associated with validating propeller slipstream characteristics obtained using low-fidelity and hybrid methods. Furthermore, the literature study also highlights the lack of data comparing the surrogate approach slipstream results with wind tunnel data. It is essential to include accurate slipstream calculations in the early aircraft design phase [13],[14]. Therefore, in spite of the high computation times, CFD may be used in the early design calculations due to its high accuracy. In an attempt to increase the propeller slipstream characteristics database estimated using high-fidelity methods, CFD analysis of a propeller-nacelle combination are carried out in the current investigation. Consequently, the propeller primary and secondary characteristics predicted by unsteady CFD simulations conducted in ANSYS Fluent are compared with wind tunnel data.

In general, there is limited wind tunnel data available that includes both primary and secondary aerodynamic characteristics for a known propeller geometry [15].

Ghoddoussi provides an extensive database of wind tunnel test data for propeller-nacelle combinations operating at low Reynolds numbers [15]. The tests were conducted for two different propellers blades (identified as PD1 and COMP) along with a spinner and nacelle, at different propeller pitch angles and rotation speeds. The test were conducted at the following low-speed wind tunnels: 3 ft x 4 ft tunnel at Wichita State University and 7 ft x 10 ft tunnel at National Institute for Aviation Research [15]. The wind tunnel data consists of primary aerodynamic characteristics such as thrust generated, power required and efficiency for varying advance ratios. In addition, secondary aerodynamic characteristics such as nacelle pressure distribution and slipstream velocities are also provided at a freestream velocity of 67 ft/s. In the wind tunnel repeatability tests, it is observed that the power curves for PD1 propeller varied by 4-5%, whereas, there is no significant variation in thrust and power curves of the COMP propeller [15]. Therefore, as the COMP propeller primary characteristics are comparatively more consistent than PD1 propeller, COMP propeller data is used in the current investigation. The slipstream data for this propeller is available only at a rotational speed of 6,000 RPM and propeller pitch of 20°.

CHAPTER 2

PROPELLER TORQUE EFFECTS

Propellers are rotating lifting surfaces which produce thrust by changing momentum in the direction of flight. In addition to primary aerodynamic characteristics, certain inherent effects caused by the presence of a propeller need to be considered in the aircraft conceptual design phase. These side-effects include torque effects, blockage effects, hub and tip effects, propeller tip high speed effects, skewed wake effects and propeller noise [16]. Based on the above categorization of side-effects, slipstream falls under the torque effects category. It is beyond the scope of the current investigation to describe all the aforementioned propeller side-effects. Therefore, only the propeller torque effects are described briefly in this section.

In case of a tractor configuration aircraft with right-handed engine (propeller rotating in the clockwise direction when viewed from cockpit), the aircraft tends to yaw to the left. The four factors which contribute to this yawing tendency are:

- Torque reaction of engine and propeller
- Gyroscopic precession
- P-factor (Prop-factor)
- Slipstream/prop wash

Section 2 focuses on providing a brief description on origin, prediction and the methods for counteracting the yawing tendency for each individual factor. It also highlights the complexity of predicting slipstream characteristics compared to other propeller torque effects. Although the torque effects in this section are explained for fixed-wing aircraft, these effects are applicable for fixed-wing UAVs as well.

2.1 Torque Reaction of Engine and Propeller

In right-handed engines, the propeller rotates in counter clockwise direction when viewed from front of the aircraft. The yawing tendency associated with torque reaction of engine and propeller is summarized below:

- According to Newton's third law, due to the propellers' rotation in counter clockwise direction, the rest of the airplane has a tendency to rotate in the opposite (clockwise direction when seen from front of the aircraft) direction as shown in Figure 1(a).
- The left wing tends to be pushed down which is counteracted by generating a rolling moment in clockwise direction using ailerons as shown in Figure 1(b).
- The applied aileron deflection makes the aircraft asymmetric in terms of aerodynamic loads because the left wing produces more lift than the right wing. The left wing has additional drag compared to the right wing due to increase in profile drag (increase in surface area) and induced drag (increased lift caused by downward aileron deflection). As the left wing has additional drag, the aircraft experiences adverse yaw, which is counteracted by a right rudder deflection to restore the aircraft to its original position as shown in Figure 1(c).

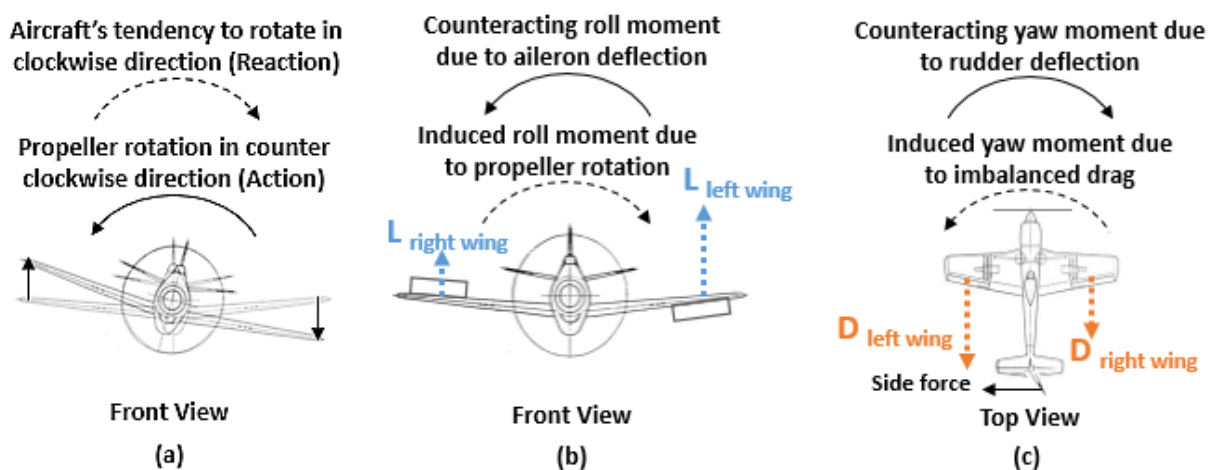


Figure 1. Propeller torque reaction yaw moments.

If the propeller is assumed to rotate about aircraft x-axis with a constant angular velocity ω_x , the angular momentum (\vec{h}) generated by propeller is [16]

$$\vec{h} = (h_x)\hat{i} + (0)\hat{j} + (0)\hat{k} = I_{(xx)prop}\omega_x\hat{i} \quad (1)$$

where $I_{(xx)prop}$ is the propeller's moment of inertia about the x-axis.

An estimate of roll and yaw moments required to counteract the left turning tendency due to engine and propeller torque can be obtained from equation (1).

2.2 Gyroscopic Precession

In case of tractor configuration aircraft, the left turning tendency associated with gyroscopic precession is noticeable only when the aircraft pitch is changed. For example, in case of pitch down, the elevators are deflected downwards to lower the aircraft nose.

Figure 2 shows the following:

- The applied force (elevator deflection) on the tail and aircraft weight generates a twist in the aircraft longitudinal plane. This generated twist has an effective force at point P (in the longitudinal plane) on the propeller.
- Due to gyroscopic precession, the effective force is rotated in the direction of propeller rotation resulting a force at point Q. According to the helicopter flying handbook, gyroscopic precession is defined as the resultant action or deflection of a spinning object when a force is applied to this object [17]. This action occurs approximately 90° in the direction of rotation from the point where the force is applied [17].
- The resultant force at point Q generates a yawing moment and the aircraft tends to yaw to left which is counteracted by a right rudder deflection.

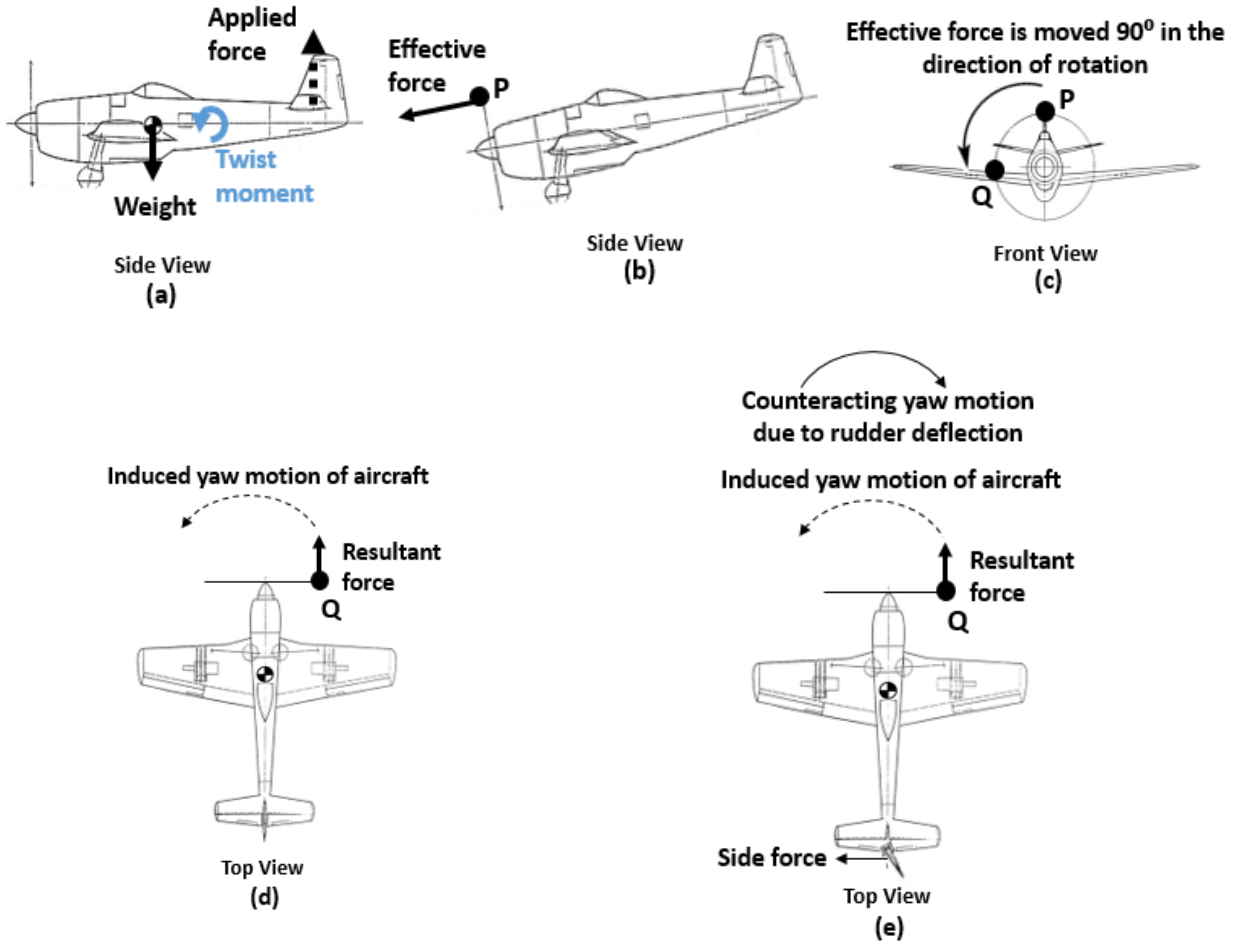


Figure 2. Propeller gyroscopic effects yaw moments.

In Gudmundsson's book [16], the gyroscopic moments are defined by equation (2).

$$\vec{M}_p = \begin{bmatrix} M_x \\ M_y \\ M_z \end{bmatrix} = \vec{\omega}_p \times \vec{h} \quad (2)$$

Where $\vec{\omega}_p$ is the angular velocity of precession

If p_p , q_p and r_p represent the rotation rates of an airplane about its x, y and z-axis, the angular velocity of precession due to these rotation rates is given by equation (3).

$$\vec{\omega}_p = p_p \hat{i} + q_p \hat{j} + r_p \hat{k} \quad (3)$$

The gyroscopic moments can be written as

$$= \begin{bmatrix} \hat{i} & \hat{j} & \hat{k} \\ p_p & q_p & r_p \\ h_x & h_y & h_z \end{bmatrix} \quad (4)$$

In case of just aircraft pitching, equation (4) reduces to

$$\vec{M}_P = \begin{bmatrix} M_x \\ M_y \\ M_z \end{bmatrix} = \begin{bmatrix} \hat{i} & \hat{j} & \hat{k} \\ 0 & q_p & 0 \\ h_x & 0 & 0 \end{bmatrix} \quad (5)$$

$$= -q_p h_x \hat{k} \quad (6)$$

An estimate of yaw moment required from rudder deflection to counter act the yawing moment generated by propeller gyroscopic precession can be obtained from equation (6).

2.3 P-Factor

P-factor is also known as asymmetrical thrust/ asymmetrical yaw effect/ asymmetrical propeller loading. When an aircraft moves at a high angle of attack, the propeller's descending blades have a larger effective angle of attack when compared to the ascending blades. Therefore, the descending blades produces larger thrust than the ascending blades and this imbalance in thrust shifts the thrust center line towards the descending blades.

In case of a right-handed engine, the larger thrust on descending blades tends to turn the aircraft nose to the left and produces a yawing moment which can be counteracted by a right rudder deflection. For aircraft with low thrust-to-weight ratio, the yawing moment generated by P-factor is significant and a large rudder deflection is required to trim the yawing moment [18].

For right-handed engine, the yawing moment (N_P) associated with P-factor can be estimated using equation (7) [19],[20]

$$N_P = \frac{\sigma q A R}{2} \left\{ \frac{2\pi}{3J} \bar{C}_l + \frac{a}{2} \left[1 - \left(\frac{J}{\pi} \right)^2 \ln \left(1 + \left[\frac{\pi}{J} \right]^2 \right) \right] - \frac{\pi}{J} C_d \right\} \alpha \quad (7)$$

where

- σ Propeller solidity which is defined as the ratio of blade and disk area (-)
- q Dynamic pressure (N/m²)
- A Propeller disk area (m²)
- R Radius of propeller blade (m)
- J Propeller advance ratio (-)
- \bar{C}_l Average section lift coefficient (-)
- a Section lift-curve slope (radians⁻¹)
- C_d Average section drag coefficient (-)
- α Angle of attack (radians)

The magnitude of yaw moment by rudder deflection required to counteract the yaw moment produced by P-factor can be estimated using equation (7).

2.4 Slipstream

An aircraft wing produces lift by a pressure imbalance on the upper and lower surfaces of the wing. Due to pressure imbalance at the wing tip, wing tip vortices are formed downstream of the flow which induces a downward component of velocity (downwash). Downwash reduces the effective angle of attack experienced by wing cross sections.

Similarly, propellers produce thrust by a pressure imbalance between the thrust face and flat face; and vortices are formed at the propeller blade tip. In the downstream

region, vortices induce velocity components which will affect the angle of attack at the local sections of the propeller blade as well as airframe components placed behind the propeller. The flow downstream of the propeller is known as propeller slipstream/wake. The propeller slipstream represents a helical pattern due to the propeller's combined forward and rotational motion.

In the case of right-handed engine, the slipstream approaches from left side and changes the angle of attack at the vertical stabilizer [18]. Consequently, a side-force is generated about the vertical stabilizer which is directed towards the right wing, generating a left yawing tendency about the aircraft center of gravity as shown in Figure 3a [18]. This left yawing tendency is counteracted by a right rudder deflection (shown in Figure 3b).

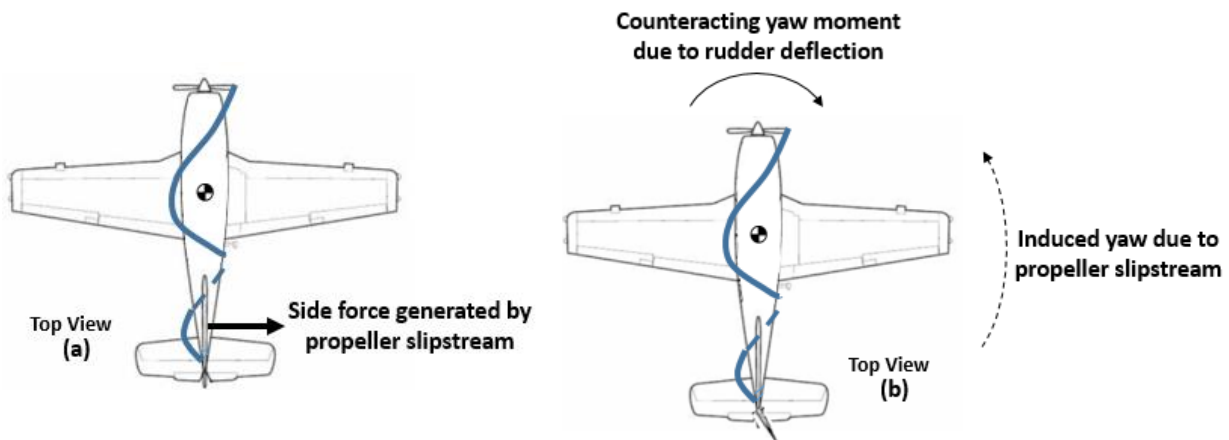


Figure 3. Propeller slipstream yaw moments.

The propeller slipstream interaction with various airframe components, such as fuselage, wing and tail, is complex and unsteady in nature. Therefore, unlike the propeller torque effects described in Section 2.1 to 2.3, the yaw moment generated by propeller slipstream cannot be easily estimated. These effects are generally predicted using either wind tunnel tests, flight tests, analytical or numerical analysis.

The above described slipstream effect is an example of propeller slipstream influence on flight stability and control characteristics. Propeller slipstream also directly affects the aerodynamic characteristics of the airframe components within the slipstream. For example, the portion of wing within the propeller slipstream will produce larger lift and drag components compared to the rest of the wing.

Overall, the propeller slipstream significantly influences aircraft's aerodynamics, stability and control characteristics. Therefore, it is essential to accurately estimate propeller slipstream characteristics which necessitates the need to validate propeller secondary characteristics along with propeller primary characteristics.

CHAPTER 3

LITERATURE REVIEW

As mentioned in in Section 1, the aerodynamic characteristics of propeller-airframe components can be obtained using the following:

- Low-fidelity methods
- High-fidelity methods
- Hybrid methods
- Surrogate methods

A brief literature review was conducted based on estimating propeller-airframe combination characteristics using the above mentioned methods. In low-fidelity methods, the aerodynamic characteristics of both propeller and airframe components are obtained using their respective low-fidelity methods. In terms of literature pertaining to low-fidelity methods for propeller-airframe components, the data presented in this document mostly comprises of propeller-wing combinations. As the low-fidelity methods for wings are well documented [7],[20],[21], these methods are not reviewed in this document.

The hybrid methods are based on estimating primary characteristics of the propeller using low-fidelity methods and providing these results as source terms to the momentum equation in CFD analysis. Therefore, because the propeller low-fidelity methods play a pivotal role in hybrid methods as well as low-fidelity methods of propeller-airframe components, a brief description of these methods is provided in Section 3.1.

The primary focus of the current investigation is to estimate propeller secondary characteristics using unsteady CFD simulations. Therefore, to gain acquaintance with

propeller CFD setup, the information pertaining to propeller CFD settings was reviewed in detail whenever applicable.

3.1 Propeller Low-Fidelity Methods

Rankine introduced the first mathematical model of a propeller in 1865 [22],[23],[24]. Rankine's theory was based on the assumption that a propeller can be represented as an infinite-blade actuator disk and this disk is enclosed within a streamtube. This actuator disk of infinitesimal thickness is placed in an incompressible and inviscid flow. The disk is assumed to absorb engine power and dissipate it in the form of a pressure drop across the disk, which increases kinetic energy in the propeller slipstream [22]. This theory only considers conservation of momentum in axial direction i.e., the actuator disk produces thrust without imparting any rotation in the propeller slipstream. Rankine's theory based on the above assumptions is known as axial momentum theory or one-dimensional momentum theory. This theory can be used to calculate approximate values of propeller thrust, slipstream axial velocity and ideal efficiency.

In 1887, R.E. Froude extended the axial momentum theory to calculate propeller slipstream velocity by considering rotational motion in the slipstream. This theory is known as Rankine-Froude momentum theory or general momentum theory of propellers [22],[25].

Rankine's and Froude's actuator disk theory assumes an actuator disk with uniform loading (constant thrust across the actuator disk). In case of propellers with non-uniform loading, an actuator disk mathematical model with vorticity distribution can be used. In 1962, Wu proposed the first actuator disk model with non-uniform loading [26].

Furthermore, Conway's work provides significant insight over actuator disk models with non-uniform loading [27].

In 1878, W. Froude introduced a mathematical model which accounts for the propeller geometry and number of propeller blades to predict the propeller thrust and torque characteristics [22],[28]. According to this theory, the propeller thrust and torque are determined by integrating the lift and drag characteristics of the airfoils along the propeller blade radius. Unlike the momentum theories, the blade element theory is not based on conservation of momentum. Therefore, this theory cannot predict induced velocities in the propeller's upstream and downstream region.

As mentioned previously, the momentum theories can estimate propeller slipstream velocities but an inherent limitation lies in the assumption of modelling propeller using an infinite-blade actuator disk. Consequently, propeller shape and number of blades are not taken into account for estimating the propeller primary and secondary characteristics. Although the blade element theory accounts for propeller geometry, it is limited to calculate only the propeller primary characteristics. In the early 19th century, these two theories were combined to predict local forces (primary aerodynamic characteristics) using blade element theory and induced velocities using momentum theory. This combination of the two theories is known as the blade element momentum theory [22]. This theory may provide an accurate initial estimate of propeller primary and secondary characteristics. Although BEM theory is simple to use, one of the disadvantages associated with this method includes the necessity to incorporate correction factors such as hub and tip loss corrections to account for three-dimensional flow effects on blade performance.

Due to the limitations associated with blade-element momentum theory, research was carried out to estimate propeller characteristics utilizing the propeller blade circulation distribution. Lifting line theory, originally developed for wings, was extended to lightly loaded propellers by Prandtl. In propeller lifting line theory, a propeller blade is replaced by bound vortex and the slipstream is represented by a trailing vortex. The initial lifting line theory results for propellers were obtained using Betz condition which implies that in uniform flow, an infinite bladed propeller generates the least induced drag when the propeller wake reaches a constant pitch in the ultimate wake [22]. As the Betz condition was only applicable to infinite number of blades assumption, Goldstein considered the effect of number of blades in calculating propeller characteristics by including correction factors [29]. Based on Betz condition and Helmholtz laws, the propeller blade geometrical characteristics can be obtained using lifting line theory by estimating the radial circulation distributions. The early use of lifting line theory was limited to design problems (i.e., inverse design applications — to obtain the blade geometry for given performance characteristics). Lerbs [30] extended the lifting line theory to moderately loaded propellers and Strscheletsky [31] developed the lifting line theory for heavily loaded propellers.

In lifting surface theories, the propeller is approximated by vortices in span-wise and chord-wise directions on the propeller mean camber surface. The slipstream is approximated using free vortices emanating from the span-wise bound vortices. To account for blade thickness, singularity elements such as source and sink are placed along the blade chord-wise direction [22]. These methods can be used for design and analysis problems. Unlike the previously discussed low-fidelity methods which follow a steady-state approach, the lifting surface theories can be modeled using both steady and

unsteady approaches. The propeller Vortex Lattice Method (VLM) is a simplified version of lifting surface methods for propellers.

Panel method is the most accurate low-fidelity method as it does not include geometric approximations like the other low-fidelity methods. This method is also known as boundary element method. In this method, the propeller blade surface and propeller slipstream are discretized using quadrilateral panels with singularity distributions. The singularity elements used for propeller surface are source and doublet whereas for slipstream, doublets are used. Similar to lifting surface methods, the panel methods can also be implemented using both steady-state and time-dependent approaches [32].

A detailed explanation on propeller lifting line, lifting surface, vortex lattice and panel methods is provided in Carlton's book [22].

3.2 Propeller-Airframe Components Combination

3.2.1 Low-Fidelity Methods

Agostinelli et al. [33] developed a method to rapidly predict the propeller slipstream effects on wing aerodynamics, suitable for early design stages. The propeller characteristics were obtained from BEM theory and the wing characteristics were based on a database obtained using RANS simulations. The wing aerodynamic database consisted of lumped force and moments along the wing span. For a given flight condition, this method implements an iterative process of data exchange from wing aerodynamics database and BEM calculations to estimate the propeller-wing interference effects. The overall lift coefficient obtained from this rapid method were compared with the results of a hybrid method. The hybrid method was based on modeling the propeller as a flat disk and the propeller characteristics obtained using BEM theory were provided as source

terms to RANS simulations. The rapid method results were in good correlation with the hybrid method results.

Bohari et al. [34] also developed an aerodynamic characteristics prediction tool suitable for early design stages. This study focuses on predicting the effect of propeller slipstream on wing longitudinal characteristics (lift and drag) within the linear aerodynamic region. In the process of developing the aerodynamic tool, the authors explored three different methods to study effect of propellers on the wing aerodynamics. The first method was based on the implementation of VSPAERO module in OpenVSP. In this software, the propeller characteristics obtained from actuator disk theory was coupled with wing characteristics obtained using the VLM. The second method was implemented using a MATLAB code to couple the propeller characteristics obtained using BEM theory with the lifting line theory for wing characteristics. The third method was also based on MATLAB code to couple the propeller BEM calculations with the VLM for wing characteristics. The computational results were compared with wind tunnel data available for a transport aircraft configuration with four propellers and two variations of wing span (short and medium span). The results were compared for Reynolds number varying from 2.7×10^6 to 4.1×10^6 . The overall lift curve characteristics from all the three methods were compared for varying advance ratios for medium wing span configuration and it was concluded that the third method provided accurate results compared to the first two methods. The authors also highlighted the limitations of the first two methodologies. Furthermore, the overall lift and induced drag predicted from the third method showed a good correlation with wind tunnel results for both medium and short span aircraft variations with varying advance ratios.

Stone [35] developed a rapid aerodynamic prediction tool suitable for conducting multi-disciplinary optimization calculations and building a comprehensive aerodynamic database for a tail-sitter UAV. In this unconventional aircraft configuration, the propeller slipstream plays a crucial role in the overall performance characteristics. The propeller aerodynamic characteristics were obtained using blade element theory with a customized slipstream development methodology. The aerodynamic characteristics of airframe components were estimated by a low-order fixed-wake panel method. In this panel method, the singularity element was a vortex ring and the trailing vortices were represented using horse shoe vortex. To account for viscous effects, the mathematical model utilizes wind tunnel data (which includes post-stall data) for airfoil look up tables. The numerical lift and drag coefficients were compared with wind tunnel data available for a similar unconventional aircraft for angle of attack varying from -10° to 90° . It was observed that the computational results were in good correlation with wind tunnel data at low angles of attack and predicted satisfactory results at high angles of attack.

Although the first reviewed case in this section does not use low-fidelity methods to obtain the wing aerodynamic characteristics, this case was classified under “low-fidelity” to showcase a different approach to easily and rapidly predict propeller effects on wing aerodynamics. The above literature data suggested that low-fidelity methods could be used to predict propeller-aircraft component interaction with reasonable accuracy. However, the propeller slipstream effect is estimated only on the global aerodynamic forces such as wing lift and drag. A detailed information of propeller effects on the aircraft components “surface” cannot be obtained using most of the low-fidelity methods. For example, it may not be possible to obtain pressure distribution of a wing surface in

propeller slipstream using the VLM, as the wing thickness is ignored. Among low-fidelity methods, panel methods may potentially provide detailed characteristics information as it does not include any geometric approximations. Another limitation of these methods is that they are applicable only to inviscid flow fields and tend to rely on post-stall airfoil aerodynamic data (obtained from experiments or high-fidelity methods) to incorporate viscous effects.

3.2.2 High-Fidelity Methods

A significant amount of literature is available pertaining to calculation of propeller primary aerodynamic characteristics using CFD analysis [12],[36],[37]. As the current investigation focuses on estimating propeller secondary characteristics, literature which is relevant for estimating the propeller secondary characteristics using CFD analysis is provided in this document.

Stuermer and Rakowitz [38] compared the propeller slipstream velocities for an eight bladed isolated propeller with wind tunnel data. The numerical investigation consists of two different methodologies. The numerical settings for both approaches are provided in Table 1.

TABLE 1

COMPARISON OF DIFFERENT NUMERICAL APPROACHES IN REFERENCE [38]

	Approach 1	Approach 2
Mesh type	Structured (Multi-Block)	Unstructured (Chimera)
Flow solver	DLR FLOWer	DLR TAU
Viscous type	Viscous	Inviscid
Governing equations	Navier-Stokes	Euler
Mesh size	≈ 11.45 million nodes	≈ 2.00 million nodes

TABLE 1 (continued)

	Approach 1	Approach 2
Governing equations	Navier-Stokes	Euler
Mesh size	≈ 11.45 million nodes	≈ 2.00 million nodes
Turbulence model	Wilcox k-w (KoK modified)	-
Spatial discretization	Central scheme	Central scheme
Scalar dissipation coefficients (k2, k4)	0.5, 1/128	0.5, 1/64
Time-Step size	Time taken to rotate propeller by 1°	Time taken to rotate propeller by 1°
Number of inner iterations	30	50

The numerical model did not include wind tunnel walls and supports. The simulations were performed to complete at least 4 rotations, at angles of attack of 0° and 10°. In this study, the propeller slipstream characteristics were quantified using axial velocity components. The numerical axial velocity components were compared with wind tunnel data for an angle of attack of 10° at two axial positions ($x/R = 0.2, 0.656$). The numerical results obtained from both approaches have a good qualitative agreement with the wind tunnel data. However, Approach 2 over predicts the maximum axial velocity which was attributed to the inviscid assumption, coarser mesh resolution, no matrix dissipation and higher scalar dissipation coefficients compared to Approach 1.

Roosenboom et al. [39] compared the propeller slipstream experimental and time-accurate numerical investigation results for a transport aircraft configuration with 4 turboprop propellers. This study focused on estimating the propeller slipstream characteristics at low speed and high angle of attack flight conditions. The wind tunnel data consists of Particle Image Velocimetry data which includes slipstream velocity and vorticity data for 5 spanwise stations located in the vicinity of starboard side – outboard

propeller. The numerical operating conditions correspond to the wind tunnel test operating conditions at a Reynolds Number of 1.25×10^6 . The numerical model represents the wind tunnel model without wind tunnel walls and support structures. The CFD solver - DLR TAU code, was used for the unsteady CFD simulations, which utilizes a dual-time approach for time-dependent solutions. The mesh and discretization scheme details are summarized in Tables 2 and 3 respectively.

TABLE 2
MESH DETAILS IN REFERENCE [39]

Mesh Details	
Type:	Chimera-Unstructured
# Chimera blocks:	3
Wall Y^+ :	< 1 (except propellers)
# Prism layer cells:	25
Total mesh size:	≈ 36.44 million nodes

TABLE 3
DISCRETIZATION SCHEMES USED IN REFERENCE [39]

Spatial Discretization Schemes	
Convective terms:	Second order central differencing with matrix dissipation
Viscous terms:	Central differences

In the numerical model, the propeller surfaces were modeled as “inviscid” walls to limit the number of mesh elements. Consequently, prism layers were generated to resolve the boundary layer on all the aircraft components except the propeller surfaces. A sufficient grid resolution was included to capture the propeller slipstream accurately. The flow was assumed to be fully turbulent and the Spalart-Allmaras turbulence model

modified by Edwards and Chandra was used. The simulations were carried out for 55 rotations on 96 CPUs. During the final rotations, to increase the accuracy of results, the time-step value corresponding to the time taken to rotate the propeller by 1° and 200 inner rotations were specified. The numerical results have an overall good agreement with the wind tunnel data. The authors also highlighted the limitations of using unstructured grids, inviscid models and RANS formulation for obtaining propeller slipstream characteristics. It was observed that the numerical vorticity contours were not as well defined like the wind tunnel data which was attributed to the numerical dissipation effects. Further, the numerical velocity was slightly higher compared to the wind tunnel data which was identified as a by-product of modeling the propellers as inviscid surfaces.

Thom and Duraisamy [10] compared the slipstream characteristics estimated using CFD with wind tunnel data. In this study, numerical simulations were conducted for two different propeller airframe component combinations: propeller-nacelle and propeller-wing. Furthermore, two different numerical approaches were implemented: time-accurate Euler calculations and surrogate approach. The Euler calculations were conducted only for the propeller-nacelle combination. A chimera mesh was generated for a numerically higher order accurate (WENO) CFD solver. The simulations were conducted at a freestream velocity of 50 m/s. A time-accurate Euler approach was implemented to eliminate the numerical diffusion introduced by viscous and turbulence effects. The time-step size used for the time-accurate Euler simulations was not explicitly specified. It is assumed that the time-step size used for the unsteady Euler simulations was the same as the one used for unsteady surrogate model (which corresponds to the time taken to

rotate the propeller by 0.5°). The numerical axial velocity and swirl angle predicted by unsteady Euler simulations, have a good agreement with the wind tunnel data.

The above literature pertaining to estimating propeller slipstream using CFD analyses provides significant insight about the mesh types, numerical discretization accuracy and time-step size used for predicting propeller secondary characteristics. It also highlights, that unlike low-fidelity methods, the high-fidelity methods can provide detailed propeller slipstream characteristics. The slipstream characteristics presented by Thom and Duraisamy has a better correlation with test data compared to the other reviewed cases. This better correlation is assumed to be due to the use of fifth-order accurate scheme solver which may have reduced the numerical dissipation effects.

3.2.3 Hybrid Methods

Malki et al [40] used a BEM-CFD hybrid method to predict the performance characteristics of a tidal stream turbine. In this hybrid method application, the propeller characteristics were obtained using BEM theory and provided as source terms in RANS simulations. In general, propeller performance characteristics are expressed in terms of varying advance ratio. However, in this study, the implemented BEM theory provides blade performance characteristics for varying tip speed ratio. The source terms were varied radially and expressed in terms of local aerodynamic coefficients (lift and drag), flow inclination angle and chord length. The Navier-Stokes equations were solved using PHYSICA software. A pressure-based solver with Rhie-Chow interpolation method for pressure derivative and SIMPLEC algorithm was used. The hybrid method results were compared with available tow-tank experimental data and verified with classic BEM theory results. Experimental airfoil aerodynamic data was used for the BEM calculations. The

turbine experimental data consisted of performance characteristics for two scenarios: shallow and deep immersion. Blockage correction factors were applied to the hybrid method results to be consistent with the procedure followed for experimental data corrections. The wind tunnel data indicated distinct performance characteristics for the different immersion scenarios. However, the implemented hybrid methodology was unable to distinguish between the two scenarios due to the steady state approximation in evaluating propeller characteristics (BEM) as well as RANS simulations (assuming the flow-field around the turbine has significant unsteady effects). The hybrid method results with blockage effects have satisfactory correlation with wind tunnel data for deep immersion scenario.

Stuhlpfarrer et al [41] conducted experimental and numerical investigations of propellers used in electrically powered aircraft. The wind tunnel model consists of propeller and fuselage only. In the wind tunnel tests, the model forces were recorded for Reynolds number varying from 4.74×10^5 to 7.97×10^5 . For preliminary CFD analysis, the performance characteristics of propeller only with a customized nacelle were conducted in ANSYS FLUENT using two methodologies: URANS simulations and BEM-CFD hybrid method. The propeller primary characteristics obtained from these two methods were compared with wind tunnel data. The propeller tip speed operates at a Mach number greater than 0.3. Therefore, in the full URANS simulations, compressible flow governing equations were solved. The full URANS simulation settings are summarized below in Tables 4 and 5.

TABLE 4
MESH AND SOLVER DETAILS IN REFERENCE [41]

Mesh Details	Solver Settings
Type: Structured	Solver type: Pressure-Based
Wall Y ⁺ : <1	Turbulence model: SST <i>k-ω</i>
# Prism layer cells: 20	Pressure-Velocity coupling: SIMPLE

TABLE 5
DISCRETIZATION SCHEMES USED IN REFERENCE [41]

Discretization Schemes	
	Gradients: Least squares cell based
	Temporal: Bounded second order implicit
Spatial	Momentum, density and energy: Second order upwind
	Viscous terms: First order upwind

In addition to the above settings, the under-relaxation factors were also varied. In the hybrid method, the airfoil aerodynamic characteristics required for BEM calculations were obtained from inviscid vortex panel method coupled with boundary layer integration method to account for viscous effects (viscous drag). The thrust and tangential force obtained from BEM were provided as momentum source terms to the RANS simulation. The solver settings for hybrid method RANS simulation was similar to the URANS settings. A detailed grid and temporal independence study were conducted for full URANS simulations whereas only a grid independence study was conducted for hybrid methods as these simulations follow steady-state approach. Based on the grid and time-step independence study, the full URANS simulations were implemented for a mesh with approximately 13 million cells and performed for 5 complete rotations with 2° rotation every time-step. In terms of thrust, the full URANS has a better correlation with wind

tunnel data for varying advance ratios and blade pitch angle compared to hybrid method. The local characteristics predictions by the numerical methods were quantified in terms of pressure distribution along multiple cross sections of blade radius and normalized axial slipstream velocity along the nacelle (at climb and cruise flight conditions). These pressure and normal axial slipstream velocity data predicted using hybrid method were in good correlation with the full URANS simulation data. The computation time for the hybrid methods was 400 times lesser than the full URANS simulations, indicating the computational efficiency achieved by using hybrid methods. The author also suggested that the hybrid method results can be improved by improving the BEM results.

In the above literature for hybrid methods, the first case showcases the limitations of hybrid method implementation for flow-fields with strong transient effects. The second case represents the dependency of hybrid method accuracy on the accuracy of BEM (propeller low-fidelity method) results. Therefore, despite of coupling propeller low-fidelity method with RANS simulations to obtain detailed propeller slipstream characteristics with better computational efficiency, the desired accuracy may not be achieved. This data also showcases the different ways to define source terms. It is observed that there is paucity of data comparing the propeller secondary characteristics obtained from hybrid methods with wind tunnel data.

3.2.4 Surrogate Methods

Although the following reference does not deal with propeller slipstream characteristics, it is included in the current document as it provides valuable information about setting up propeller full URANS and surrogate model simulations. Carroll [42] implemented the surrogate modeling approach, in which a 2-bladed Micro Air Vehicle

(MAV) propeller primary aerodynamic characteristics obtained from full URANS simulation were provided as momentum source terms to RANS simulations. The preliminary study focuses on highlighting the difference in thrust distribution along the propeller blade radius obtained using URANS simulations and the BEM theory. The airfoil aerodynamic data required for the BEM calculations were obtained from CFD simulations. The Navier-Stokes equations were solved using the CHEM software which is second-order accurate. The viscous approximations for airfoil and propeller simulations were implemented using Menter's SST turbulence model with a wall Y^+ less than 5. Unstructured meshes were generated for airfoil and propeller. When compared to the propeller URANS results, the BEM under predicts thrust near the blade root and over predicts thrust near the blade tip which highlights the limitations of BEM, although the BEM calculations include hub and tip loss correction factors. Further CFD analyses were conducted as training simulations to collect the information required to implement a surrogate model. In this case, each propeller blade is divided into 30 spanwise segments, and thrust and swirl components were measured for each of these segments. The CFD settings used for the training simulations were the same as the preliminary CFD analysis. The time-step used corresponds to the time taken to rotate the propeller by 1° and the analysis was carried out to have at least 5 rotations. In addition, the angle of attack and Reynolds number at each blade segment were measured on a plane (placed slightly upstream of the propeller blades), were extracted from the last time-step. The angle of attack and Reynolds number were provided as inputs to surrogate model to enable local adaptability (accounts for local changes if the surrogate model is placed in a different flow field). In the numerical model for surrogate model, the propeller blades were not included,

instead the thrust and swirl components from training simulations were modeled as momentum source terms to RANS simulations in ANSYS FLUENT using user defined functions. This application represents a steady-state surrogate model. The mesh size used for the surrogate models was approximately 10 times lesser than the mesh used for full URANS simulations. The surrogate model results were verified with full URANS simulations in terms of thrust and swirl distributions along the propeller blade. These results have a good correlation with full URANS simulations. Similar work conducted by Christina et al [43] compare the surrogate model results in terms of thrust and tangential forces for varying rotational speeds with full URANS simulations. The surrogate model results have a good correlation with the full URANS results.

Thom and Duraisamy [10] implemented unsteady and steady surrogate models. A description about the propeller-nacelle unsteady Euler CFD analysis was discussed in Section 3.2.2. The surrogate method was implemented for analyzing the propeller-wing combination, in which, the propeller was approximated by a flat disk. Two different methodologies were used for the surrogate approach: unsteady and steady. In case of unsteady surrogate model, the propeller velocities calculated during the propeller-nacelle unsteady Euler simulations were measured about a plane located slightly downstream of the propeller. These measured velocities were provided as time-dependent boundary condition in the numerical model. The time-step used for the simulation corresponds to the time taken to rotate the propeller by 0.5° . The pressure coefficients obtained using unsteady surrogate numerical simulations were compared with wind tunnel data at two wing-spanwise stations. The unsteady surrogate model results have a good correlation with the wind tunnel data. In case of steady surrogate model, the averaged results for

propeller-nacelle unsteady calculations were provided as steady boundary conditions. The results from steady surrogate case are compared with the unsteady surrogate case in terms of spanwise wing lift and drag distributions. There is a satisfactory correlation for lift and a 40% difference in drag at the wing spanwise location where the propeller tip vortex was expected to meet the wing. Based on these results, it was observed that the steady surrogate model is unable to accurately capture the unsteady tip vortex effects on the wing.

Ying et al [44] implemented the surrogate methodology for two different propeller-airframe component combinations: propeller-nacelle and propeller-wing. The propeller-wing combination represents a turbo-prop configuration. This study was conducted to check the applicability of surrogate method and full URANS methods for different stages of aircraft design. The software used for grid generation as well as flow solution were not mentioned. A structured overset grid technique was used for all the studies. The unsteady calculations were performed using a time-step size of $1/1440$ rotating period and Spalart-Allmaras turbulence model. The spatial discretization was obtained using second-order upwind schemes and for temporal discretization, the Lower-Upper Symmetric Gauss-Seidel (LU-SGS) scheme was used. In terms of surrogate model for the two configurations, the propeller was approximated by an actuator disk and the unsteady CFD results for their respective configurations were given as source terms to the RANS solver. The propeller-nacelle combination was analyzed for a freestream velocity of 30 m/s with four different propeller rotational speeds ranging from 4,992 RPM to 6,560 RPM. The computational thrust was slightly higher compared to the experimental data. However, it was not clear whether the computational thrust corresponds to unsteady CFD calculations

or surrogate model results. For verification purposes, the averaged axial and tangential velocities were measured about 4 stations along the nacelle length. The surrogate axial velocities have good agreement with the unsteady calculations. The discrepancy observed in surrogate tangential velocity comparison was attributed to the inability of capturing propeller torque accurately and simulating the propeller hub to be stationary. For the propeller-wing combination, the surrogate model results were verified with unsteady CFD results in terms of wing spanwise-lift, pressure coefficient and axial velocity distributions. In addition, the CFD results for the isolated wing were compared against the propeller-wing surrogate and unsteady CFD results to study the difference in aerodynamic parameters due to the presence of a propeller. The surrogate model results have a good agreement with the unsteady CFD results for the propeller-wing combination. Based on the surrogate model results for the two configurations, it was suggested that surrogate modeling approach could be used in early design phase.

The above literature for surrogate methods depicts the different approaches to develop a surrogate method. Although the surrogate methodology is promising in terms of obtaining propeller slipstream characteristics with good computational efficiency, sufficient data is not available showcasing the numerical method applications and comparison of the surrogate model results with wind tunnel data. The summarized references only deal with comparing the surrogate model slipstream characteristics with other numerical investigation results.

CHAPTER 4

OBJECTIVE

The main aim of this thesis investigation is to compare the propeller secondary characteristics estimated using high-fidelity methods, such as CFD, with wind tunnel data. The flow solver used is ANSYS Fluent. As mentioned in Section 1, the COMP propeller provided in Ghoudoussi's work is used as the numerical model. This propeller is chosen due to the ease of availability of propeller geometry and wind tunnel test conditions. In terms of propeller secondary characteristics, the wind tunnel data consists of nacelle pressure distribution, slipstream velocities and swirl angle. Therefore, the current investigation is based on comparing the aforementioned propeller secondary characteristics estimated using ANSYS Fluent, with wind tunnel data.

The propeller wind tunnel tests were carried out at low Reynolds numbers ranging from 65,000 to 130,000 [15]. Due to the low Reynolds number, a transition viscous model is used for the propeller full URANS solution. However, due to inexperience in using transition viscous models within ANSYS Fluent, preliminary two-dimensional calculations are conducted which are based on estimating the aerodynamic characteristics of a low Reynolds number airfoil. For this two-dimensional study, Eppler 387 airfoil is chosen for two reasons: availability of wind tunnel data and the COMP propeller consists of Eppler 387 airfoil with varying chord and pitch along the blade radius [15].

In addition to ANSYS Fluent, the airfoil characteristics are also estimated using a low-fidelity method code, XFOIL. Subsequently, the Eppler 387 airfoil lift, drag and pitching moment obtained using XFOIL and ANSYS Fluent are compared with wind tunnel data. This comparison will provide an assessment of ANSYS Fluent transition modeling

capabilities. In addition, the comparison will also highlight the difference in accuracy of results obtained using low and high-fidelity methods for low Reynolds number airfoils.

Overall, the current investigation consists of 2 major segments:

- Estimation of Eppler 387 characteristics in XFOIL as well as ANSYS Fluent and comparing the obtained results with wind tunnel data.
- Estimation of COMP propeller primary and secondary characteristics in ANSYS Fluent and comparing the obtained results with wind tunnel data.

CHAPTER 5

THEORETICAL BACKGROUND

5.1 Propeller Aerodynamic Characteristics

In the current investigation, the propeller aerodynamic characteristics are classified based on wind tunnel data provided in Ghoudoussi's work [15]. The propeller characteristics classification is shown in Figure 4.

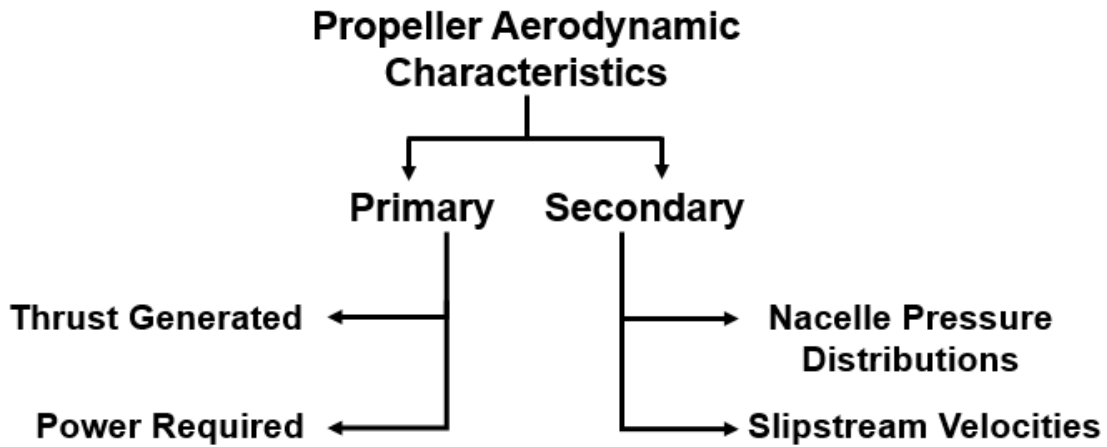


Figure 4. Propeller aerodynamic characteristics classification.

A propeller generates thrust by converting engine torque into a change in momentum in the direction of flight. The propeller power required is the amount of power supplied by the engine to generate thrust. The definitions of propeller thrust generated (C_T) and power required (C_{pow}) coefficients used in the current investigation are provided in equations (8) and (9):

$$C_T = \frac{T}{\rho n^2 D^4} \quad (8)$$

$$C_{pow} = \frac{P_{prop}}{\rho n^3 D^5} \quad (9)$$

where

T	Propeller thrust generated (N)
P_{prop}	Propeller power required (W)
ρ	Fluid density (kg/m ³)
n	Propeller rotational speed in rotations per second
D	Propeller diameter (m)

In general, propeller primary aerodynamics characteristics are measured for varying advance ratio. As shown in equation (10), advance ratio (J) is defined as the ratio of forward velocity to the propeller rotational velocity. For a constant rotational velocity, at a low advance ratio, a propeller experiences stall due to low forward velocity. Therefore, the massive flow separation at stall leads to difficulty in accurately predicting propeller characteristics at low advance ratios.

$$J = \frac{U}{nD} \quad (10)$$

where

U	Freestream velocity (m/s)
-----	---------------------------

The Reynolds number (Re) of the propeller is calculated using equation (11). The velocity and reference length (c) are measured about the blade section located at a radial distance of 0.75 times the blade radius (R) from the propeller hub.

$$Re = \frac{\rho V_t c_{0.75}}{\mu} \quad (11)$$

where

V_t	Propeller tangential velocity at 0.75 R (m/s)
$c_{0.75}$	Propeller chord at 0.75 R (m)
μ	Fluid dynamic viscosity (N-s/m ²)

In the above definition of propeller Reynolds number, the tangential velocity (V_t) is defined as

$$V_t = r_{0.75} \omega \quad (12)$$

where

$r_{0.75}$ Propeller radius at 0.75 R (m)

ω Propeller rotational velocity (radians per second)

The propeller rotation may alter the flow field around the components placed within the propeller slipstream. In the current investigation, the numerical model consists of a nacelle within the propeller slipstream. The nacelle pressure distributions are expressed in terms of pressure coefficient on the nacelle. The pressure coefficient (C_p) is calculated using equation (13).

$$C_p = \frac{P - P_\infty}{\frac{1}{2} \rho U^2} \quad (13)$$

where

P Local static pressure (Pa)

P_∞ Freestream static pressure (Pa)

A brief explanation of propeller slipstream is provided in Section 2.4. The change in momentum due to propeller rotation leads to increased axial and tangential velocities in the propeller downstream region (slipstream region). During the propeller rotation, there is a continuous shedding of trailing edge vortices and a prominent tip vortex from the propeller blade. These vortices lead to significant velocity gradients along the radial direction in the slipstream region. Therefore, the slipstream velocities are generally expressed in terms of radial distributions rather than a single averaged value. In the

current investigation, in accordance with propeller wind tunnel data [15], the slipstream velocities are dealt in cylindrical coordinate system.

5.2 XFOIL

A detailed explanation of XFOIL is beyond the scope of this documentation. In this section, a brief overview of XFOIL and the method used for determining the transition point location is highlighted.

XFOIL is a two-dimensional low-fidelity method code used for designing and/or predicting aerodynamic characteristics of airfoils operating at low Reynolds number [45]. This code is based on a zonal aerodynamic approach – an iterative coupling of inviscid and viscous calculations.

The inviscid flow fields are computed using linear vorticity panel method. The viscous regions include boundary layer, airfoil wake and transitional bubbles on the airfoil upper surface. The viscous flow parameters are obtained by solving integral boundary layer equations. A detailed explanation of implementation of the integral momentum equation, kinetic energy shape parameter and the associated closure terms modeling in XFOIL, is provided in Drela and Giles work [46].

XFOIL can model both free and forced transition scenarios. In the case of free transition, the flow transition point is evaluated based on linear stability analysis approach known as the spatial amplification theory – e^n method. In XFOIL, the flow is assumed to transition from laminar flow when the disturbance of spatial waves (Tollmien-Schlichting waves) in the boundary layers exceed a user specified value of e^n . For transition cases, the value of 'n' typically varies from 7 to 9 [47]. For XFOIL, the suggested value for "n" is 9 which corresponds to an average wind tunnel condition [48].

5.3 Computational Fluid Dynamics

The following information is written from Reference [49], to provide a brief overview of the governing equations solved in ANSYS Fluent.

In ANSYS Fluent, for single-phase flows, the continuity and momentum equations solved for laminar flows are:

$$\frac{\partial \rho}{\partial t} + \nabla \cdot (\rho \vec{v}) = 0 \quad (14)$$

$$\frac{\partial(\rho \vec{v})}{\partial t} + \nabla \cdot (\rho \vec{v} \vec{v}) = -\nabla p + \nabla \cdot (\bar{\tau}) + \rho \vec{g} + \vec{F} \quad (15)$$

where

- \vec{v} Velocity vector
- p Static pressure
- $\bar{\tau}$ Stress tensor
- $\rho \vec{g}$ Gravitational body forces
- \vec{F} External body forces

For turbulent flows, the flow properties fluctuate randomly. In ANSYS Fluent, one of the methods to model the turbulence effects is the Reynolds averaging approach. In this method, the instantaneous values of flow properties are expressed as the sum of mean and fluctuating quantities. For example, the velocity components are expressed as,

$$u_i = \bar{u}_i + u'_i \quad (i = 1, 2, 3) \quad (16)$$

where

- u_i Instantaneous velocity component
- \bar{u}_i Mean velocity component
- u'_i Fluctuating velocity component

Following the Reynolds averaging approach, for single-phase flows and in Cartesian tensor form, the continuity and momentum equations are:

$$\frac{\partial \rho}{\partial t} + \frac{\partial(\rho u_i)}{\partial x_i} = 0 \quad (17)$$

$$\frac{\partial(\rho u_i)}{\partial t} + \frac{\partial(\rho u_i u_j)}{\partial x_j} = -\frac{\partial p}{\partial x_i} + \frac{\partial}{\partial x_j} \left[\mu \left(\frac{\partial u_i}{\partial x_j} + \frac{\partial u_j}{\partial x_i} - \frac{2}{3} \delta_{ij} \frac{\partial u_l}{\partial x_l} \right) \right] + \frac{\partial}{\partial x_j} (-\rho \overline{u'_i u'_j}) \quad (18)$$

where

μ	Viscosity coefficient
δ_{ij}	Kronecker delta
$-\rho \overline{u'_i u'_j}$	Reynolds stresses

In the current investigation, the transition and fully turbulent viscous models that were considered employ turbulence closure term using Boussinesq approach (linear eddy viscosity models). According to Boussinesq hypothesis, Reynolds stresses are expressed in terms of turbulent/eddy viscosity (μ_t). Various fully turbulent viscous models are available in the ANSYS Fluent which compute the turbulent viscosity by solving 1 or 2 additional transport equations. However, an inherent limitation of this approach is that the turbulent viscosity is assumed to be isotropic, which does not represent true turbulence characteristics [49].

In Section 6.1.2, k - ω SST turbulence model with Low Reynolds number corrections was used for Eppler 387 airfoil calculations. In this turbulence model, the turbulence viscosity is computed by solving two additional transport equations: One for turbulent kinetic energy (k) and one for specific dissipation rate (ω). In addition to k and ω , the effects of turbulent shear stress are also included in the turbulent viscosity calculations. When the low Reynolds number correction option is enabled in ANSYS

FLUENT for this turbulence model, a damping coefficient is introduced to the calculation of ω , which will consequently affect the turbulent viscosity calculations. The damped turbulent viscosity may delay the formation of turbulent boundary layer which makes the $k-\omega$ SST viscous model applicable for predicting the laminar to turbulent flow transition [49].

The three viscous (RANS) models in ANSYS Fluent which are specifically available to model the transition from laminar to turbulent flow are:

- $k-k_l-\omega$ transition model (Walters model)
- Transition SST model ($\gamma-Re_\theta$ model)
- Intermittency transition model (γ model)

The aforementioned transition viscous models are based on including additional turbulence transport equations (in addition to fully-turbulent flow turbulence transport equations) to compute turbulence viscosity. In other words, these transition models are based on coupling additional transport equations to fully-turbulent viscous models.

The $k-k_l-\omega$ is a three equation model based on coupling the standard $k-\omega$ fully-turbulent viscous model with an additional transport (turbulence) quantity known as laminar kinetic energy (k_l). k_l represents the energy scales of Tollmien-Schlichting waves in the boundary layer transition region. This transition model is based on the energy transfer from laminar (k_l) to fully-turbulent (k) waves in the boundary layer. The transition onset is based on empirical correlations.

The transition SST viscous model ($\gamma-Re_\theta$) is a four equation model based on coupling the $k-\omega$ SST fully-turbulent viscous model with two additional transport (turbulence) quantities: intermittency (γ) and momentum-thickness Reynolds number

(Re_θ). It is a local correlation based transition model, i.e., the flow transition onset is determined based on local flow-field values. The transition effects are introduced to the full turbulent k - ω SST viscous model by including modifications in terms of intermittency to the turbulence production transport equation (k - equation in the k - ω SST viscous model). The momentum-thickness Reynolds number transport equation which includes empirical correlations, is used to predict the transition onset and length parameters. This transition model cannot be employed for numerical models in which the wall surfaces move with respect to the coordinate system. As the current investigation is based on estimating time-accurate propeller aerodynamic characteristics using sliding mesh technique (rotation of propeller blades), the transition SST model cannot be used.

The intermittency transition model (γ model) is a three equation model based on coupling the k - ω SST fully-turbulent viscous model with only one additional transport equation (intermittency transport equation). This viscous model is a simplified version of the transition SST model. Unlike the transition SST model, the intermittency transition model:

- Includes empirical correlations for determining the transition parameters within the intermittency transport equation itself and eliminates the need of momentum-thickness Reynolds number transport equation.
- Can be used for numerical models in which the wall surfaces move with respect to the coordinate system.

In the current investigation, the intermittency transition model is used for both airfoil and propeller CFD analysis.

CHAPTER 6

NUMERICAL ANALYSIS AND RESULTS

6.1 Eppler 387 Airfoil

The COMP propeller blades consist of Eppler 387 airfoil varying in chord and twist angle along the blade radius [15]. The wind tunnel tests for the COMP propeller were conducted at a low Reynolds number of 100,000. At these low Reynolds numbers, the flow field is laminar, i.e., the flow field is dominated by viscous forces and the flow may transition to turbulent flow with increase in angle of attack. The numerical simulation of such mixed laminar-turbulent flow fields require the use of transition viscous models. Therefore, to assess the transition model capabilities of ANSYS Fluent at low Reynolds number, preliminary analyses were carried to compare the Eppler 387 airfoil CFD results with wind tunnel data.

In the current investigation, the numerical simulations for the Eppler 387 airfoil were conducted at the same wind tunnel Reynolds number used for the COMP propeller experimental investigations ($Re = 100,000$) [15]. The wind tunnel results for the Eppler 387 airfoil which are available at a Reynolds number of 100,000, indicates the presence of a laminar separation bubble (LSB) on the airfoil [50],[51]. A LSB occurs at low angles of attack and low Reynolds number, when the laminar flow on the airfoil detaches along the airfoil curvature due to strong pressure gradients, and transitions to turbulent flow. As the turbulent flow is more stable compared to laminar flow, the turbulent shear layer thickens rapidly and reattaches back to the airfoil surface. An attached turbulent flow exists aft of the reattachment point. This region of laminar flow detachment and turbulent flow reattachment, forms a transition separation bubble.

In general, when compared to lift and pitching moment data, a LSB significantly increases the airfoil drag for low to moderate angles of attack.

At low Reynolds number, the airfoil flow fields are highly sensitive to any flow disturbances. Therefore, it is challenging to obtain accurate and consistent aerodynamic characteristics measurements for low Reynolds number airfoils in wind tunnel tests. Tank et al [52], and Selig and McGranahan [50] showcase the differences in wind tunnel results for the Eppler 387 airfoil at a Reynolds number of 100,000. For example, in Selig and McGrahan's work [50], the difference in drag data at an angle of attack of 4° measured in two different wind tunnels varied by approximately 22% for the 100,000 Reynolds number case. These differences in measured aerodynamic data highlight the uncertainties associated with wind tunnels tests conducted at low Reynolds number. Due to discrepancies in measured data in different wind tunnels, a single set of wind tunnel results cannot be assumed to be correct for Eppler 387 airfoil at a Reynolds number of 100,000. Therefore, in the current investigation, the numerical results of the Eppler 387 airfoil were compared against two wind tunnel data results: University of Illinois at Urbana-Champaign data (UIUC) [50] and NASA Low-Turbulence Pressure Tunnel data (NASA LTPT) [51].

The airfoil coordinates provided in both these wind tunnel test reports were compared and it was observed that in the NASA LTPT report, one of the airfoil lower surface coordinate deviates from the remaining coordinates. Therefore, in the current investigation, the two-dimensional numerical analysis were carried out on the airfoil generated using the "actual coordinates" for the Eppler 387 airfoil provided in the UIUC report [50] (plotted in Figure 5).

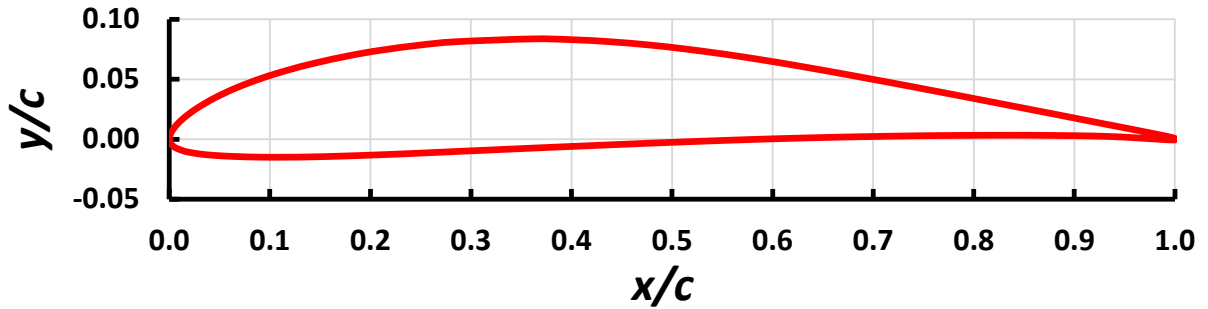


Figure 5. Eppler 387 airfoil.

A detailed assessment of the LSB involves predicting the separation (transition) point, reattachment point and bubble height of the separation bubble, and the prediction of airfoil drag increment due to the LSB. However, a detailed assessment of the LSB was beyond the scope of the current investigation and only the effect of turbulence model selection on the airfoil drag prediction was studied.

Abobaker et al [53] highlights the use of low-fidelity method codes to estimate low Reynolds number airfoil aerodynamic characteristics. XFOIL is a widely used airfoil low-fidelity method code which is based on zonal aerodynamic approach. In general, low-fidelity methods take a significantly lower computational time to predict results when compared to high-fidelity methods. In the current investigation, in addition to CFD, the Eppler 387 aerodynamic characteristics were estimated using XFOIL tool. Subsequently, the XFOIL and CFD results were compared with wind tunnel data. This comparison was done to evaluate the accuracy of results obtained using low and high-fidelity methods.

The numerical simulations were conducted at sea level (ICAO standard atmosphere) conditions. Based on sea level kinematic viscosity of $1.46 \times 10^{-5} \text{ m}^2/\text{s}$ and an airfoil with a chord length of 0.3048 m (1 foot), a freestream velocity of approximately 4.8 m/s was required to achieve a Reynolds number of 100,000.

In the current investigation, basic aerodynamic parameters such as the airfoil lift, drag and pitching moments obtained from XFOIL and ANSYS Fluent were compared with wind tunnel data. In the wind tunnel tests, the pitching moment was measured about the quarter chord point. Therefore, in the numerical analysis the pitching moment was measured at 0.0762 m from the airfoil leading edge.

6.1.1 XFOIL

In the current investigation, XFOIL version 6.96 was used. The analysis was conducted at a Mach number of 0.014 and Reynolds Number of 100,000. The imported airfoil coordinates were normalized, de-rotated and adjusted to have 250 panel nodes. In addition, the number of iterations limit was changed to 500 iterations. The default critical value of 9 is used for defining the transition point location. It is observed that for analyzing an airfoil with varying angle of attack, the XFOIL results were highly dependent on the solver convergence for the first few angles of attack (due to the implementation of Newton solution method [48]). While analyzing the Eppler 387 characteristics for angles of attack varying from -5° to 15° , the solver failed to reach convergence within 500 iterations for -5° and -4° , and although the solver convergence was met from -3° onwards, the results were unrealistic. As the flow exhibits significant separation beyond 13° , the solver convergence was again not met for angles of attack greater than 13° . Therefore, in the current investigation, the XFOIL analysis starts from -3° and ends at 13° with 1° intervals. The XFOIL results for Eppler 387 airfoil are shown in Figures 17 to 19. The XFOIL analysis was conducted on an Intel Xeon X5660 machine and the results were obtained in less than 60 seconds for the complete angle of attack range.

6.1.2 Computational Fluid Dynamics

The CFD analysis were carried out in ANSYS Fluent with double precision enabled. Due to computational resources limitations, only RANS turbulence models were considered. In the current investigation, the Eppler 387 aerodynamic characteristics were obtained using three different RANS turbulence models: laminar, intermittency transition model, and $k-\omega$ SST with low Reynolds number corrections. These three turbulence models represent the numerical models applicable for the low Reynolds number flows. In the laminar model, the flow is assumed to be fully laminar. As explained in Section 5.3, the intermittency transition model can capture both laminar and turbulent flow fields. The $k-\omega$ SST model is a fully turbulent viscous model. However, enabling the low Reynolds number corrections dampens the turbulent viscosity and facilitates its use for low Reynolds number applications.

The numerical model used for the airfoil CFD analyses is shown in Figure 6. As the operating velocity represents a low subsonic Mach number, the flow disturbances caused by the airfoil will tend to propagate in all directions. In general, for external aerodynamics problems, the CFD boundaries are placed such that the flow disturbances reflected near the boundaries do not affect the flow solution. Therefore, in the current investigation, the computational domain extents were located at least 50 times the airfoil chord length away from the airfoil itself in each direction. To verify if the domain extents were sufficiently far from the flow disturbances, the pressure gradients near the upstream and downstream boundaries (represented by velocity inlet and pressure outlet respectively in Figure 6) were checked for the preliminary CFD analysis. The pressure contour in Figure 7 indicates that there are no significant pressure gradients about the

computation domain boundaries. Therefore, the domain boundaries are located sufficiently far from the airfoil and this domain was used for all the airfoil CFD analysis.

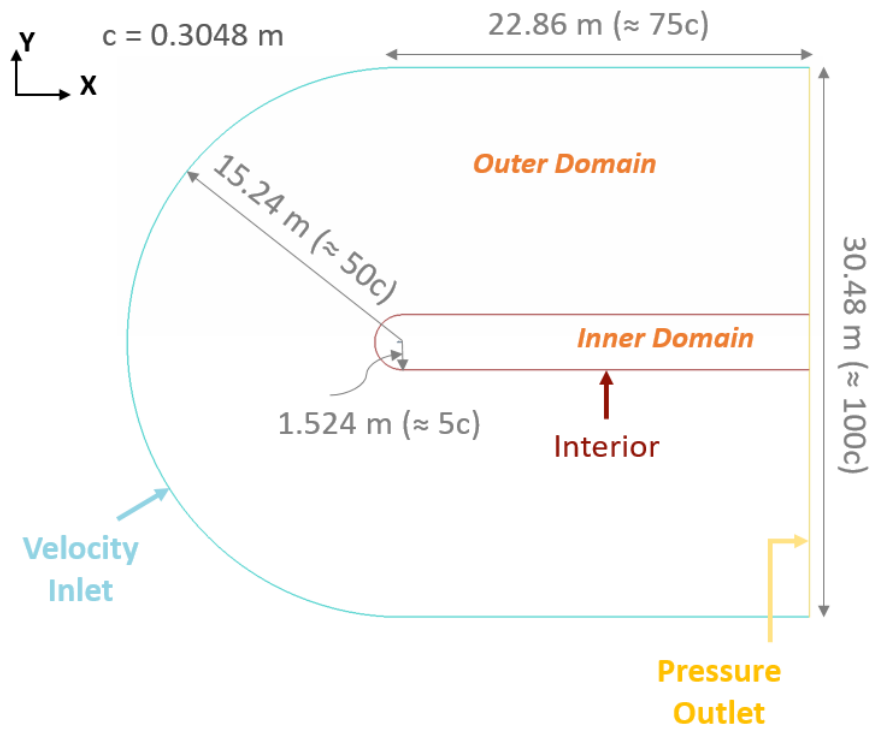


Figure 6. Numerical model details for Eppler 387 airfoil CFD analysis.

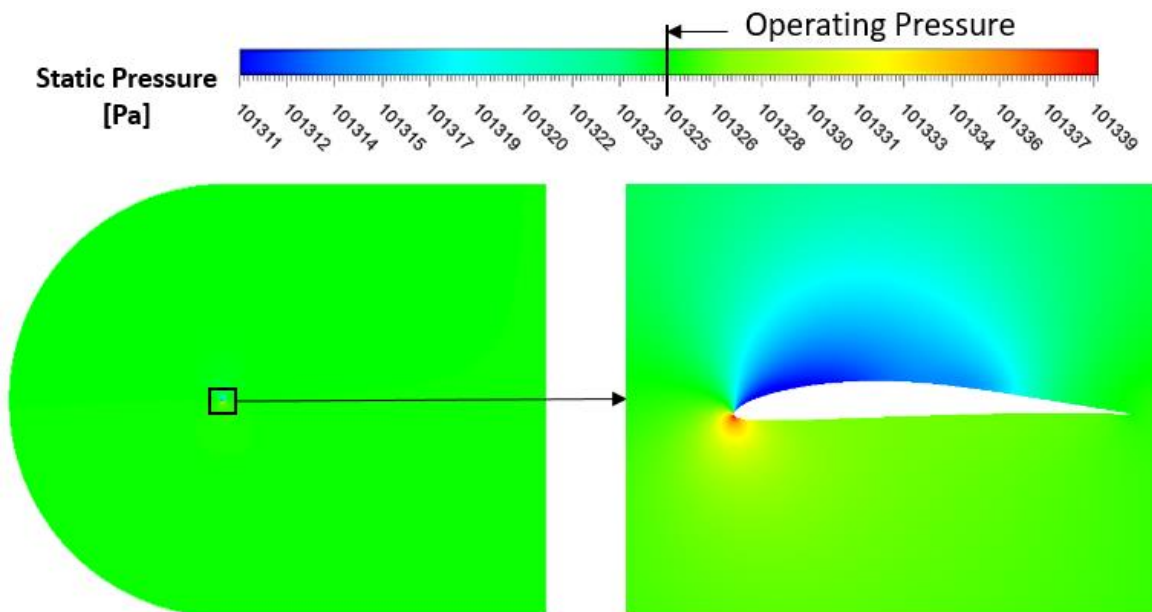


Figure 7. Static pressure contour at $\alpha = 4^\circ$
(Contour corresponds to medium mesh and intermittency model at 0.3 seconds).

In the current investigation, the airfoil hybrid meshes were generated in BETA-CAE ANSA v17.0.3 software. This software uses a bottom-up meshing approach. As shown in Figure 6, the computational domain fluid region consists of two major parts: outer and inner domains. This domain decomposition was done to limit the total mesh size, because the mesh within the inner domain was specified to have a smaller element size compared to the outer domain to capture the airfoil wake. ANSA incorporates a mesh refinement feature using “size box.” In addition to the finer mesh in inner domain, further mesh refinement was included in the vicinity of the airfoil surfaces to facilitate better capturing of the LSB by including a size box. The size box dimensions are shown in Figure 8. A typical mesh refinement obtained in inner domain and size box is shown in Figure 9.

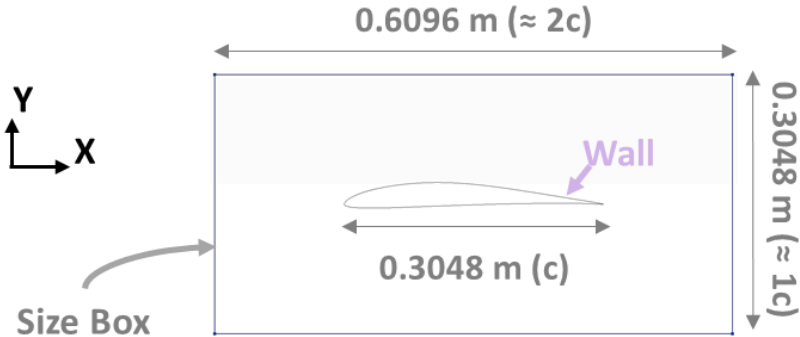


Figure 8. Eppler 387 airfoil and size box dimensions.

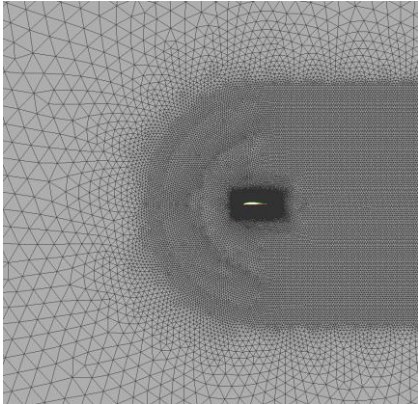


Figure 9. Schematic of mesh refinement level for Eppler 387 airfoil.

The boundary conditions used for the analysis are shown in Figures 6 and 8. In a hybrid mesh, the region within the immediate vicinity of the geometry surface is discretized using quadrilateral elements and the remaining region is discretized using triangular elements. The quadrilateral elements are used because they tend to capture the boundary layer accurately by aligning the flow parallel to the wall surface using less number of cells. In ANSA, for two-dimensional geometries, first the unstructured mesh (triangular elements) was generated for the complete domain and then the unstructured mesh in the vicinity of the geometry wall was replaced by inflation layers (quadrilateral elements) using the zone cut feature in ANSA. The transition from quadrilateral elements to the triangular elements near the airfoil is shown in Figure 10.

In an attempt to resolve the boundary layer completely, hybrid meshes were generated with a wall Y^+ of 0.1. For the Eppler 387 airfoil operating at a Reynolds number of 100,000, the first inflation layer had to be placed at a distance of 0.006 mm normal to the airfoil wall to achieve a Y^+ of 0.1. At a Reynolds number of 100,000, for a flat plate with a length equal to the airfoil chord length, the laminar boundary layer thickness is approximately 4.5 mm. It was assumed that modeling one-third of the boundary layer height will be sufficient to capture the viscous effects. Therefore, in all the airfoil CFD cases, the inflation layers extend up to 1.5 mm from the airfoil wall.

The airfoil time-accurate CFD analysis were conducted in ANSYS Fluent Release 18.2 with double precision enabled. Since the fluid operating velocity is low, the pressure-based solver with incompressible-ideal-gas law density model was used. A constant viscosity of 1.789×10^{-5} kg/m-s and operating pressure of 101,325 N/m² were specified. For the case of intermittency transition model, a pressure-based coupled algorithm is

recommended to aid in achieving a converged solution. Therefore, for consistency, the coupled algorithm was used for all the three turbulence model cases. For all scalar variables, the spatial discretization was based on the second-order upwind scheme. Their gradients and derivatives were evaluated using the least squares cell-based scheme. The pressure gradient term in the momentum equation was discretized using the second-order interpolation scheme. The temporal discretization was achieved using a second-order implicit formulation. The solver convergence criteria were based on the residuals decreasing to the default value of 0.001 for all transport equations except the energy equation (which uses a value of 10^{-6}). In addition to transport equations residual convergence, the variation of lift, drag and pitching moment coefficients with time were also monitored to ensure solver convergence. The boundary condition inputs specified for the three turbulence models are provided in Table 6. The wall boundary conditions were specified to have no-slip shear condition with zero heat flux and zero heat generation rate.

TABLE 6
BOUNDARY CONDITIONS FOR EPPLER 387 CFD ANALYSIS

		Velocity (m/s)	Gauge pressure (Pa)	Thermal (K)	Turbulence intensity (%)	Turbulence viscosity ratio (-)	Intermittency (-)
Laminar	Inlet	V_{∞}	0	288.15	-	-	-
	Outlet	-	0	288.15	-	-	-
Intermittency	Inlet	V_{∞}	0	288.15	0.1	1	0.5
	Outlet	-	0	288.15	0.1	1	0.5
<i>k-ω</i> SST with low Re corrections	Inlet	V_{∞}	0	288.15	0.1	1	-
	Outlet	-	0	288.15	0.1	1	-

In the UIUC wind tunnel report, at a Reynolds number of 100,000 the turbulence intensity varied from 0.0968% to 0.1248% [50]. Therefore, a turbulence intensity of 0.1% was specified for the numerical simulations. The turbulence parameter, viscosity ratio, and the transition model parameter, intermittency, were not known. Based on initial CFD parametric analysis for intermittency transition model at an angle of attack of 4°, it was observed that the variation in airfoil characteristics with these varying turbulence and transition parameters were less than 5%. Therefore, a turbulent viscosity ratio of 1 and intermittency of 0.5 were specified whenever applicable. The Courant number and relaxation factors specified for the three turbulence models are provided in Table 7.

TABLE 7

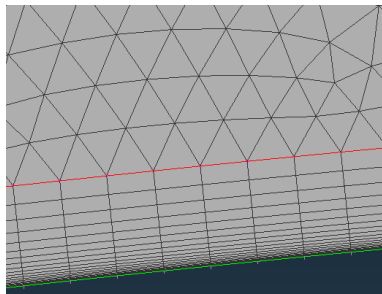
COURANT NUMBER AND RELAXATION FACTORS FOR EPPLER 387 CFD

		Laminar	Intermittency	<i>k-ω</i> SST with low Re corrections
Flow Courant number		10	10	10
Explicit relaxation factors	Momentum	0.6	0.6	0.6
	Pressure	0.75	0.75	0.75
Under-Relaxation factors	Density	0.8	0.8	0.8
	Body forces	1	1	1
	Turbulent kinetic energy	-	0.8	0.8
	Specific dissipation rate	-	0.8	0.8
	Intermittency	-	0.8	-
	Momentum thickness Re	-	0.8	-
	Turbulent viscosity	-	1	1
	Energy	1	1	1

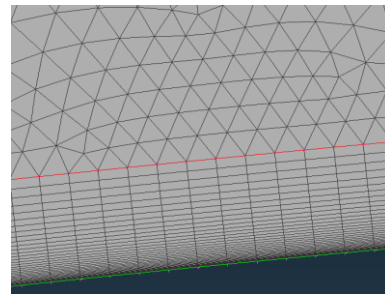
The non-dimensionalization of lift, drag and pitching moment coefficients were based on the reference values computed from the velocity inlet. In addition, the reference length and area used were 0.3048 m and 0.3048 m² respectively. The origin for this numerical model is located at the airfoil leading edge. Therefore, the pitching moment was measured at (0.0762 m, 0 m) — quarter chord point location.

6.1.2.1 Grid Independence Study

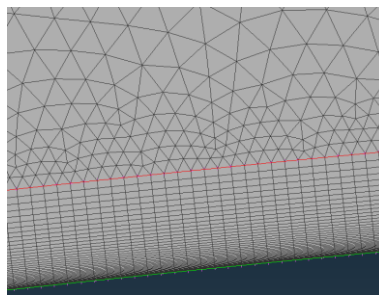
A grid independence study was conducted to check the effect of spatial discretization errors on the airfoil characteristics. In this study, three grids (coarse, medium and fine) with increasing spatial resolution were used. The grid resolution was increased by reducing the element size on all the computation model boundaries and reducing the inflation layer growth rate. In addition, the size box mesh element length was also reduced. A section of the three grids near the airfoil wall is shown in Figure 10.



(a) Coarse mesh.



(b) Medium mesh.



(c) Fine mesh.

Figure 10. Schematic of grid resolutions used for Eppler 387 grid independence study.

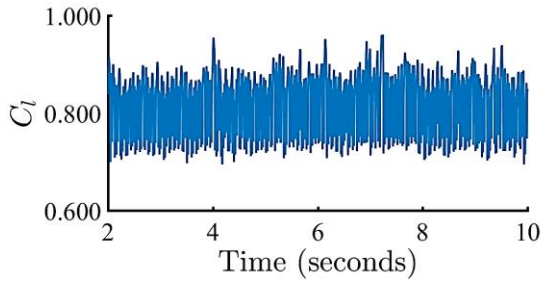
As mentioned previously, the boundary layer height of 1.5 mm was used for all the airfoil CFD simulations. Therefore, to maintain a constant total inflation layer height, with reducing inflation layer growth rate, the number of inflation layers were increased. The number of inflation layers were calculated based on exponential growth law. The details for the three meshes used are provided in Table 8.

TABLE 8

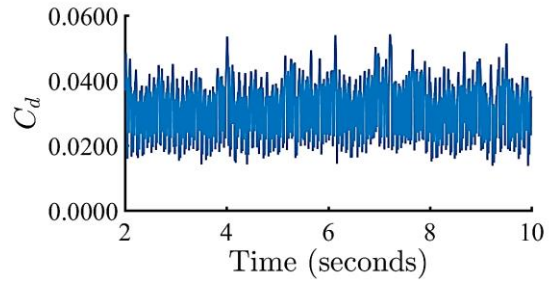
DETAILS OF MESHES USED IN EPPLER 387 GRID CONVERGENCE STUDY

		Coarse	Medium	Fine
Maximum element size (mm)	Outer domain	500	250	150
	Inner domain	60	30	18
	Size box	1.62	1.46	1.32
Inflation layer details	First layer height (mm)	0.006	0.006	0.006
	Growth rate (-)	1.2	1.1	1.08
	Number of inflation layers (-)	22	35	40
Mesh size (million cells)	Tri	≈ 0.24	≈ 0.46	≈ 0.90
	Quad	≈ 0.01	≈ 0.04	≈ 0.10
	Total	≈ 0.25	≈ 0.50	≈ 1.00

The grid independence study was conducted at an angle of attack of 4°, using all the three turbulence models. However, for brevity, only the intermittency model results are provided in this document. A time-step size of 0.001 seconds was specified with a maximum of 20 inner iterations for each time-step. The aerodynamic coefficients time convergence history (from 2 to 10 seconds) obtained with the three viscous models are shown in Figures 11 to 13 for the medium mesh.

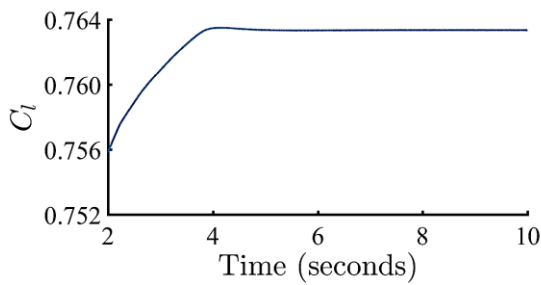


(a) Lift coefficient.

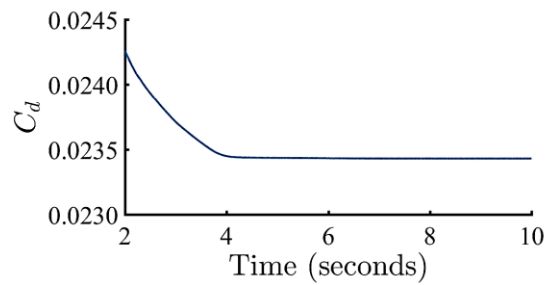


(b) Drag coefficient.

Figure 11. Time convergence history of laminar model results at $\alpha = 4^\circ$.

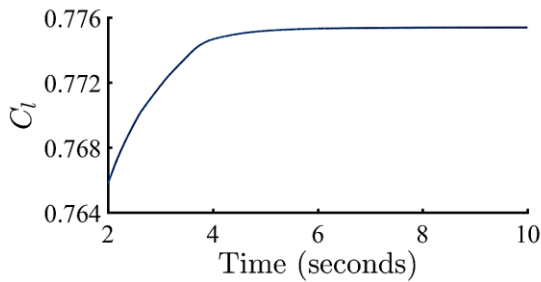


(a) Lift coefficient.

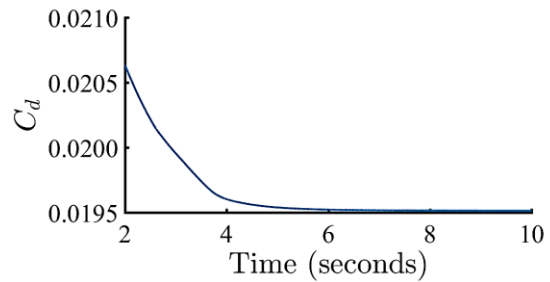


(b) Drag coefficient.

Figure 12. Time convergence history of intermittency model results at $\alpha = 4^\circ$.



(a) Lift coefficient.



(b) Drag coefficient.

Figure 13. Time convergence history of k- ω SST with low Reynolds number corrections results at $\alpha = 4^\circ$.

The simulations were terminated at 10 seconds as the results did not change significantly beyond this point. As seen from Figure 11, the airfoil lift and drag coefficients varied with similar amplitude from 4 to 10 seconds for the laminar. Due to this pattern, the laminar model results had to be averaged. This oscillating behavior of laminar results is

representative of the periodic vortex shedding and is further discussed in Section 6.1.3. The lift and drag results from the remaining turbulence models were flat from 6 to 10 seconds. As there are no detrimental effects of averaging intermittency and $k-\omega$ results, for consistency, all Eppler 387 CFD results were averaged from 6 to 10 seconds.

These CFD analysis were carried out using 8 cores on Intel Xeon X5660 machine. The grid convergence study results obtained using intermittency model at angle of attack of 4° is shown in Figure 14. It was observed that the results did not vary by more than 5% with increasing grid resolution. The grid independence studies using the other two turbulence models also have similar results and trends. Due to implementation of implicit temporal discretization scheme, the solver may need to perform multiple iterations at each time-step known as inner iterations [49]. As mentioned previously, a limit of 20 inner iterations were specified. If the solver convergence criteria are met before the 20th inner iteration, the solver advances to the next time-step. The laminar solver required more number of inner iterations to converge within each time-step when compared to the other two turbulence models. Therefore, computational time required by laminar cases was comparatively higher.

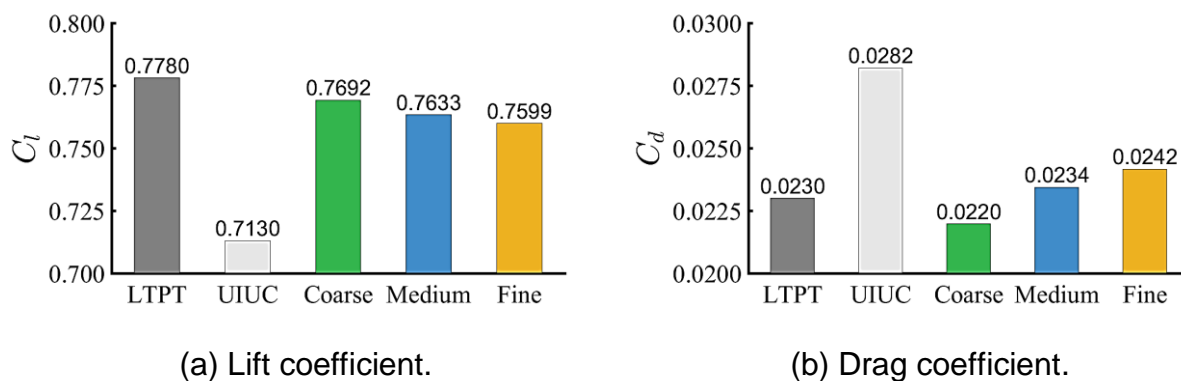
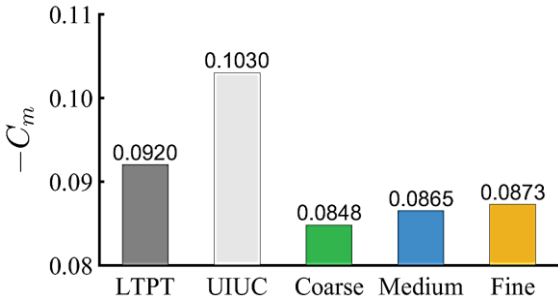
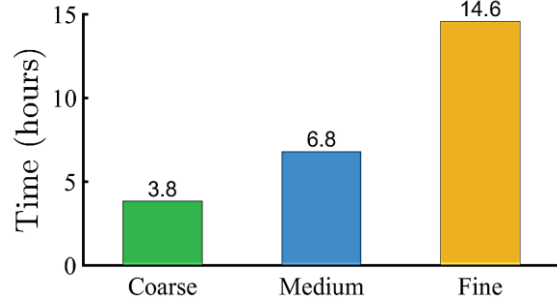


Figure 14. Grid independence study results at $\alpha = 4^\circ$ using intermittency model. (Time-step = 0.001 seconds)



(c) Pitching moment coefficient.

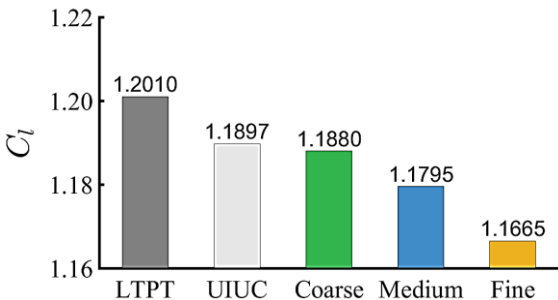


(d) Computation time.

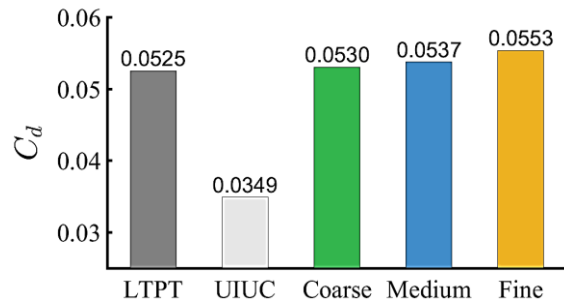
Figure 14 (continued)

In addition to angle of attack of 4° , a grid independence study was also conducted at an angle of attack of 11° . This study was conducted to check the effect of discretization errors on the airfoil characteristics when there is significant flow separation (at high angles of attack). The CFD analysis were conducted with a time-step size of 0.001 seconds and 20 inner iterations for each time-step and terminated at 10 seconds. The grid independence study results for the intermittency model at angle of attack of 11° is shown in Figure 15. These CFD analysis were also performed using 8 cores on Intel Xeon X5660 machine.

Similar to the low angle of attack grid convergence study, even at an angle of attack of 11° , the aerodynamic coefficients do not vary by more than 5%.

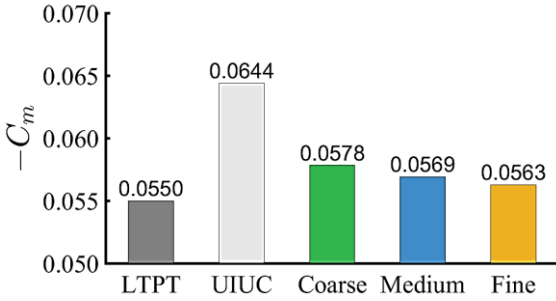


(a) Lift coefficient.

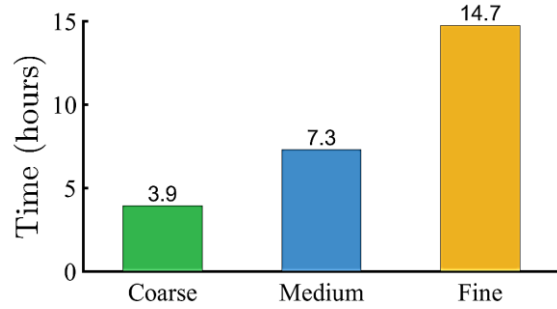


(b) Drag coefficient.

Figure 15. Grid independence study results at $\alpha = 11^\circ$ using intermittency model. (Time-step = 0.001 seconds)



(c) Pitching moment coefficient.



(d) Computation time.

Figure 15 (continued)

The grid convergence results using $k-\omega$ SST with low Reynold number corrections has similar trends as well. However, in the case of laminar model, the airfoil pitching moment varied by 15% from medium to fine mesh. This variation was likely due to the comparatively better turbulence resolution in the fine mesh compared to the medium mesh. As this better turbulence resolution cannot be handled by laminar turbulence model, the aerodynamic coefficient predictions might be erroneous. In addition, the computation time for laminar cases at 11° were also higher compared to the other two turbulence models.

Based on the two grid convergence studies results, the coarse mesh was able to predict the airfoil aerodynamic characteristics accurately. However, being conservative, the medium mesh would capture the separation bubble better due to higher grid resolution. The computation time required for medium mesh was reasonable as well. Therefore, the medium mesh was used for all the remaining airfoil CFD analysis.

6.1.2.2 Time-Step Independence Study

The airfoil simulations were based on solving the time-dependent Navier-Stokes equations. Therefore, in addition to checking for spatial discretization errors, temporal

discretization effects on the results were also checked. This study was based on checking the variation in airfoil aerodynamic coefficients with variation in time-step size. The medium mesh was used for this study and includes three different time-steps which are 0.01, 0.001, and 0.0001 seconds, up to a total of 10 seconds. Unlike the grid independence study, this time-step independence study was carried out only for the intermittency viscous model.

The results obtained using intermittency model at angle of attack of 4° are shown in Figure 16. The simulations were performed using 8 cores on Intel Xeon X5660 machine. The aerodynamics coefficients did not vary by more than 5% with variation in time-step size. The time-step size of 0.001 seconds was used for the remaining airfoil CFD simulations.

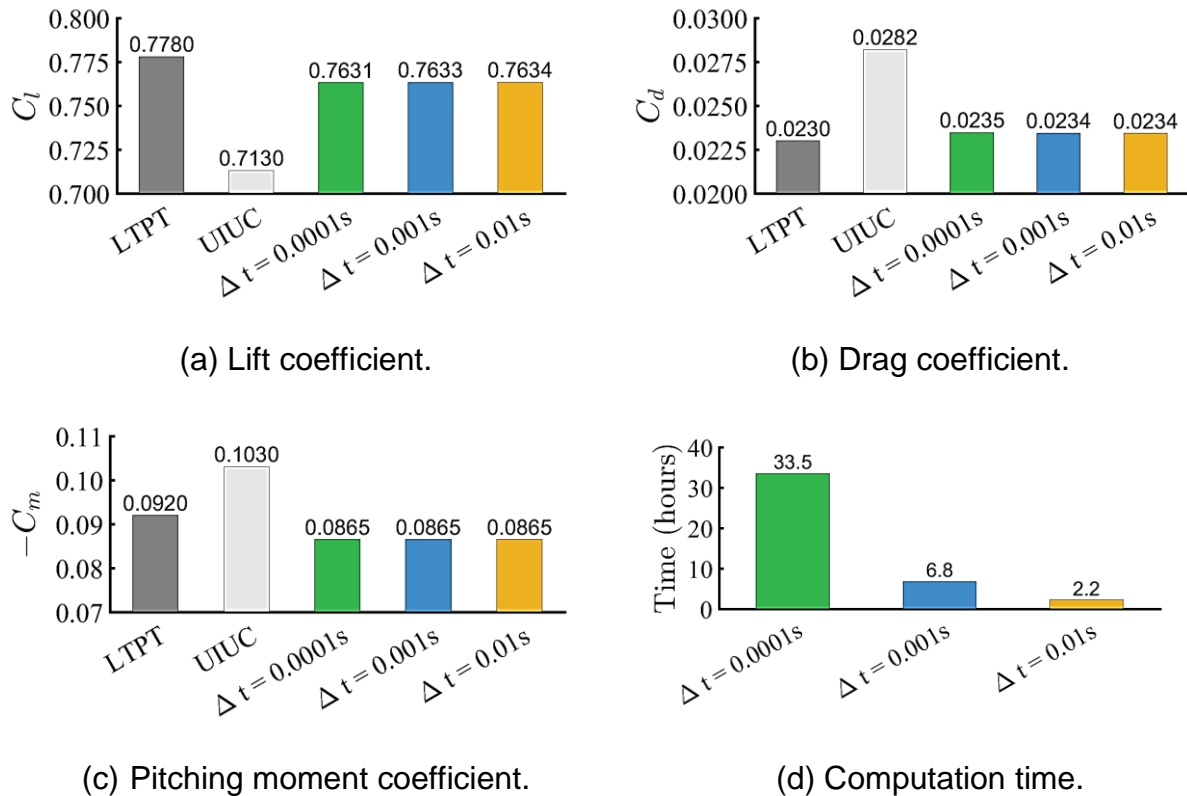


Figure 16. Time-step independence study results at $\alpha = 4^\circ$ with medium mesh and intermittency model.

Based on spatial and temporal discretization error investigations, the medium mesh with a time-step size of 0.001 seconds was used for Eppler 387 CFD analysis. The CFD results for varying angle of attack are provided in Section 6.1.3.

6.1.3 Comparison of Results

The Eppler 387 CFD results are compared with two sets of wind tunnel data and XFOIL data in Figures 17 to 19.

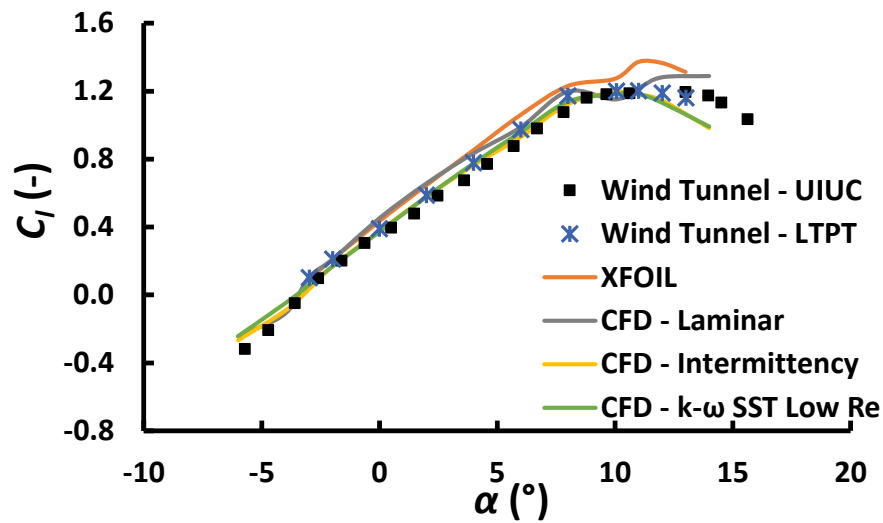


Figure 17. Variation of Eppler 387 lift coefficient with angle of attack.

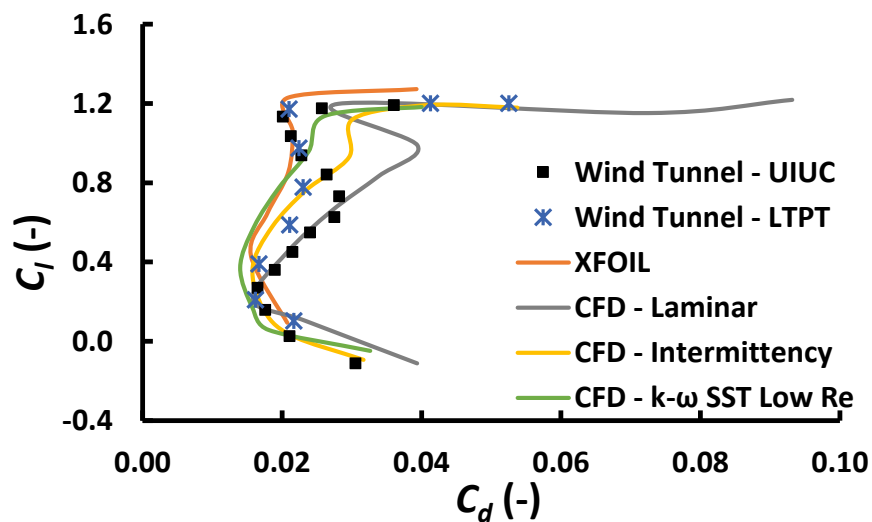


Figure 18. Variation of Eppler 387 drag coefficient with angle of attack.

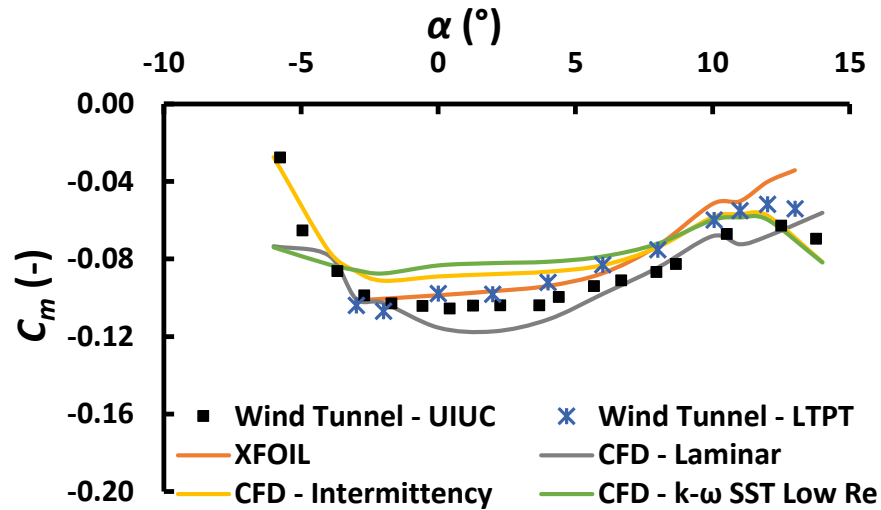


Figure 19. Variation of Eppler 387 pitching moment coefficient with angle of attack.

In these comparisons, the NASA LTPT data varies from approximately -3° to 13° for lift and pitching moment coefficients and -3° to -11° for drag coefficient. The UIUC data varies from approximately -6° to 15.5° for lift and pitching moment coefficients and -4° to 12° for drag coefficient.

As observed in Figure 17, the lift coefficient predicted by XFOIL and all the three CFD turbulence models have a good quantitative and qualitative agreement with both wind tunnel data in the linear angle of attack range. Based on both the wind tunnel data, the stall angle of attack is approximately at 11° because lift coefficient reduces with further increase in angle of attack. In the post-stall region, XFOIL and laminar models tend to slightly over predict the lift values, whereas, the intermittency and $k-\omega$ SST with low Reynolds number correction models tend to slightly under predict the lift values.

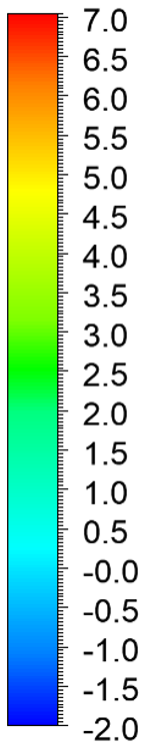
As shown in Figure 19, the pitching moment data computed by XFOIL has a good quantitative and qualitative agreement with NASA LTPT data up to stall angle of attack and under predicts magnitude beyond this point. All the CFD viscous models have qualitative agreement with either of the wind tunnel data at moderate to high angles of

attack. However, only the intermittency model has a good qualitative correlation with wind tunnel data for low angles of attack.

In the case of drag, as shown in Figure 18, for all the numerical models, the results for angles of attack varying from -4° to 11° are compared with wind tunnel data. It is to be noted that for moderate to high angles of attack, there is a significant difference between UIUC and LTPT data. Although the reason for this discrepancy is unknown, this discrepancy indicates the difficulties and uncertainties associated with accurately measuring the drag data of Eppler 387 airfoil at low Reynolds number. The drag coefficient predicted by XFOIL has a good qualitative agreement with LTPT data and under predicts the drag coefficients for angle of attack varying from 0° to 8° . The intermittency and $k-\omega$ SST with low Reynolds number correction models have a reasonable qualitative agreement with LTPT data starting from low angles of attack to approximately 6° . The LTPT data indicates a reduction in drag at approximately 8° which is not well captured by intermittency and $k-\omega$ SST with corrections models.

The laminar model data has good qualitative agreement with UIUC data for low angle of attack. However, at angles of attack greater than 4° , the drag prediction deteriorates significantly. In theory, during the LSB formation, the laminar flow transitions to turbulent flow and reattaches back to the airfoil surface. The laminar model does not capture the LSB. The difference in flow fields simulated by the three turbulence models are discussed in detail for an angle of attack of 4° . A negative value of X-component of velocity indicates flow reversal (separation). In Figures 20 to 22, the X-component of velocity contours at 4° angle of attack for all the three turbulence models at 0.1, 0.2, and 0.3 seconds are shown.

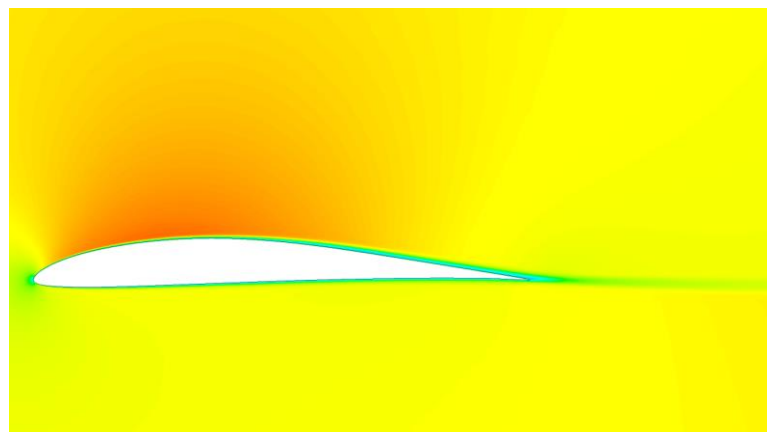
X – Velocity [m/s]



Laminar.



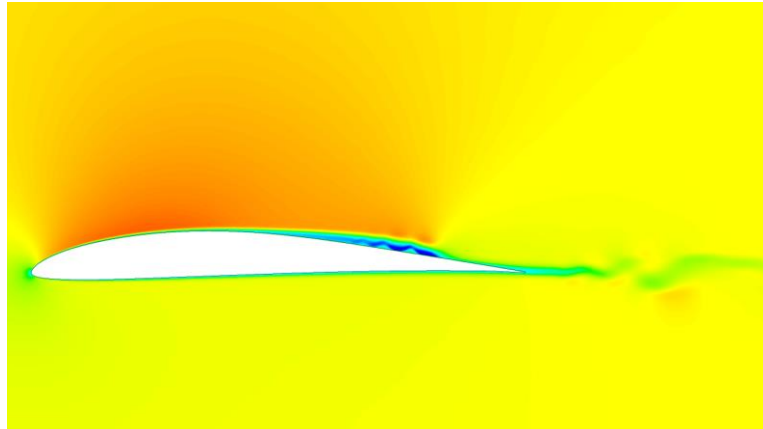
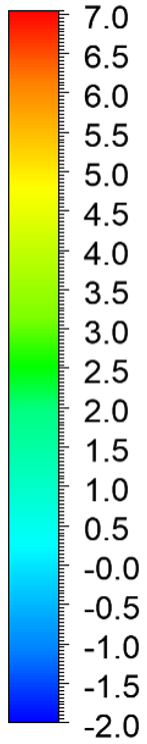
Intermittency.



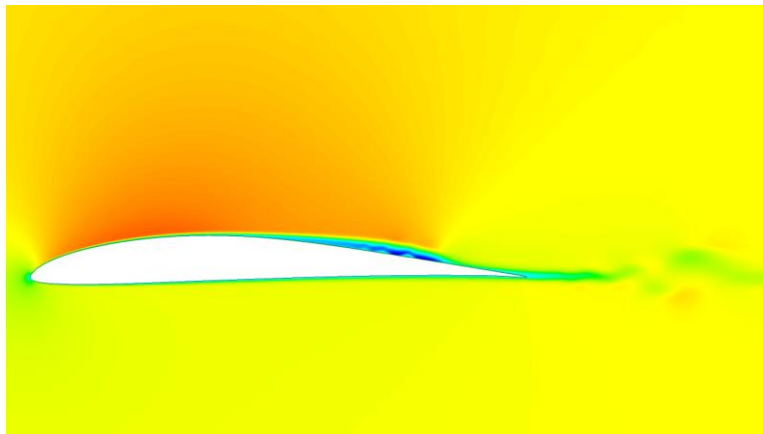
$k-\omega$ SST with low Reynolds number corrections.

Figure 20. X-velocity contours at 0.1 seconds.

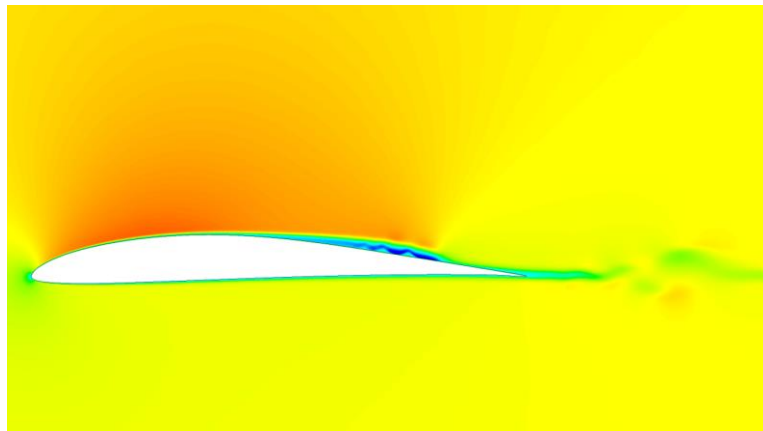
X – Velocity [m/s]



Laminar.



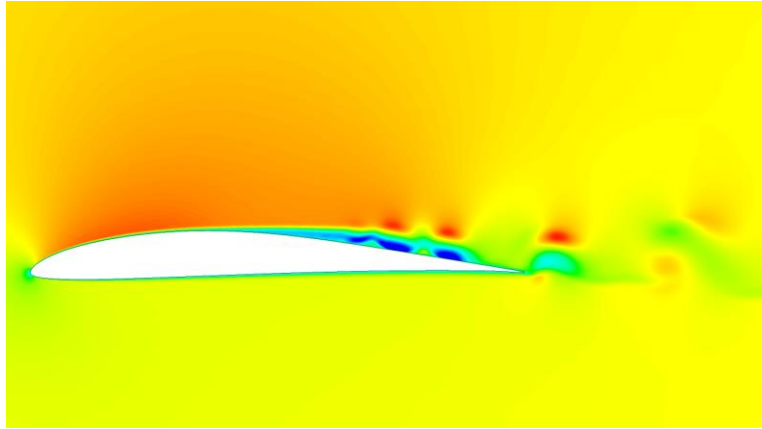
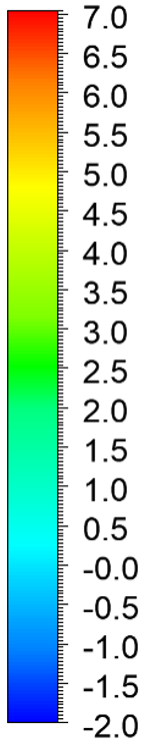
Intermittency.



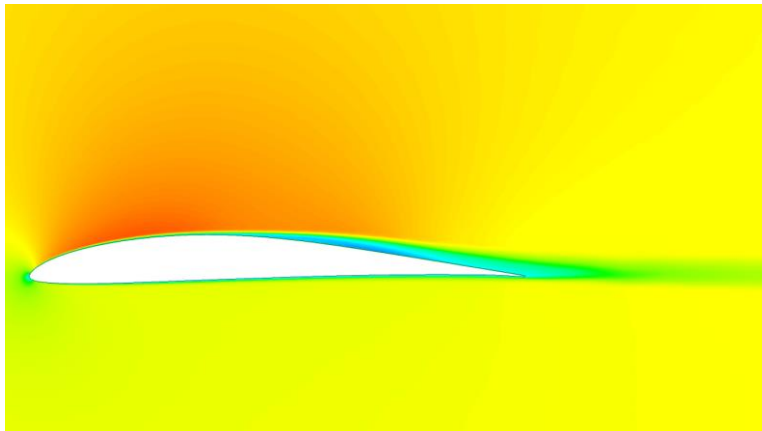
k- ω SST with low Reynolds number corrections.

Figure 21. X-velocity contours at 0.2 seconds.

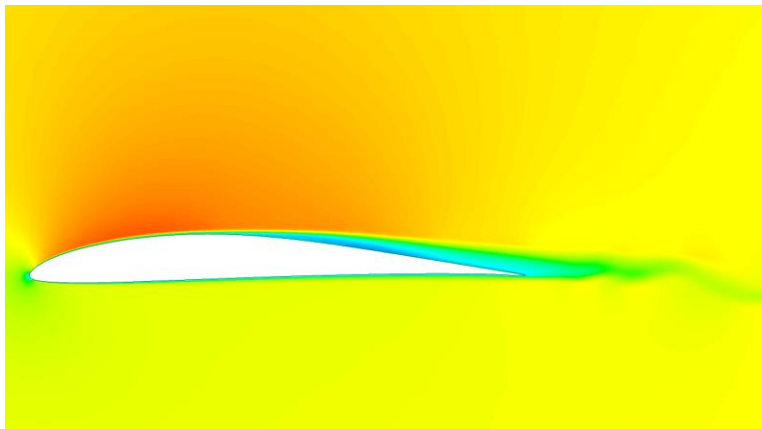
X – Velocity [m/s]



Laminar.



Intermittency.



k- ω SST with low Reynolds number corrections.

Figure 22. X-velocity contours at 0.3 seconds.

At 0.1 seconds, all the turbulence models exhibit smooth laminar flow characteristics and at 0.2 seconds, a laminar separation is visible in all the three cases. As shown in Figure 22, the intermittency and $k-\omega$ SST with low Reynolds number correction models are able to capture the turbulent boundary layer and its reattachment to the airfoil surface. However, the laminar model fails to capture the turbulence characteristics and generates periodic vortex shedding post the laminar separation.

Furthermore, the LSB visualized using velocity streamlines is shown in Figure 23. These velocity streamlines correspond to the numerical results obtained using intermittency model at angle of attack of 4° .

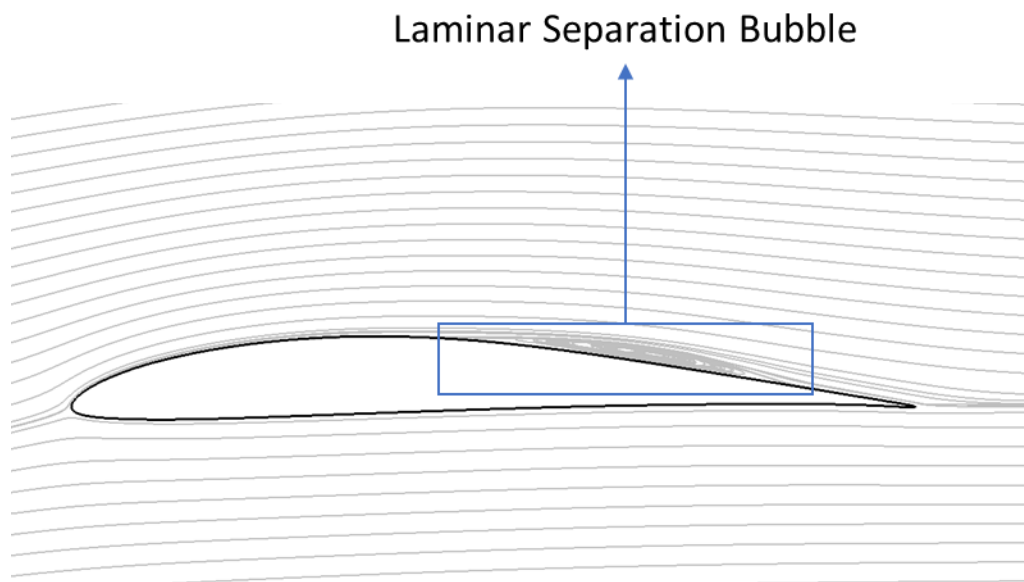


Figure 23. Laminar separation bubble on Eppler 387 airfoil.

In addition to X-component of velocity contour, the above discussed laminar separation and turbulence reattachment is shown in terms of pressure coefficient distribution as well. In Figure 24, the pressure coefficient distributions of laminar model at 0.3 seconds, depicts the vortex shedding with sinusoidal pattern in the airfoil pressure recovery region.

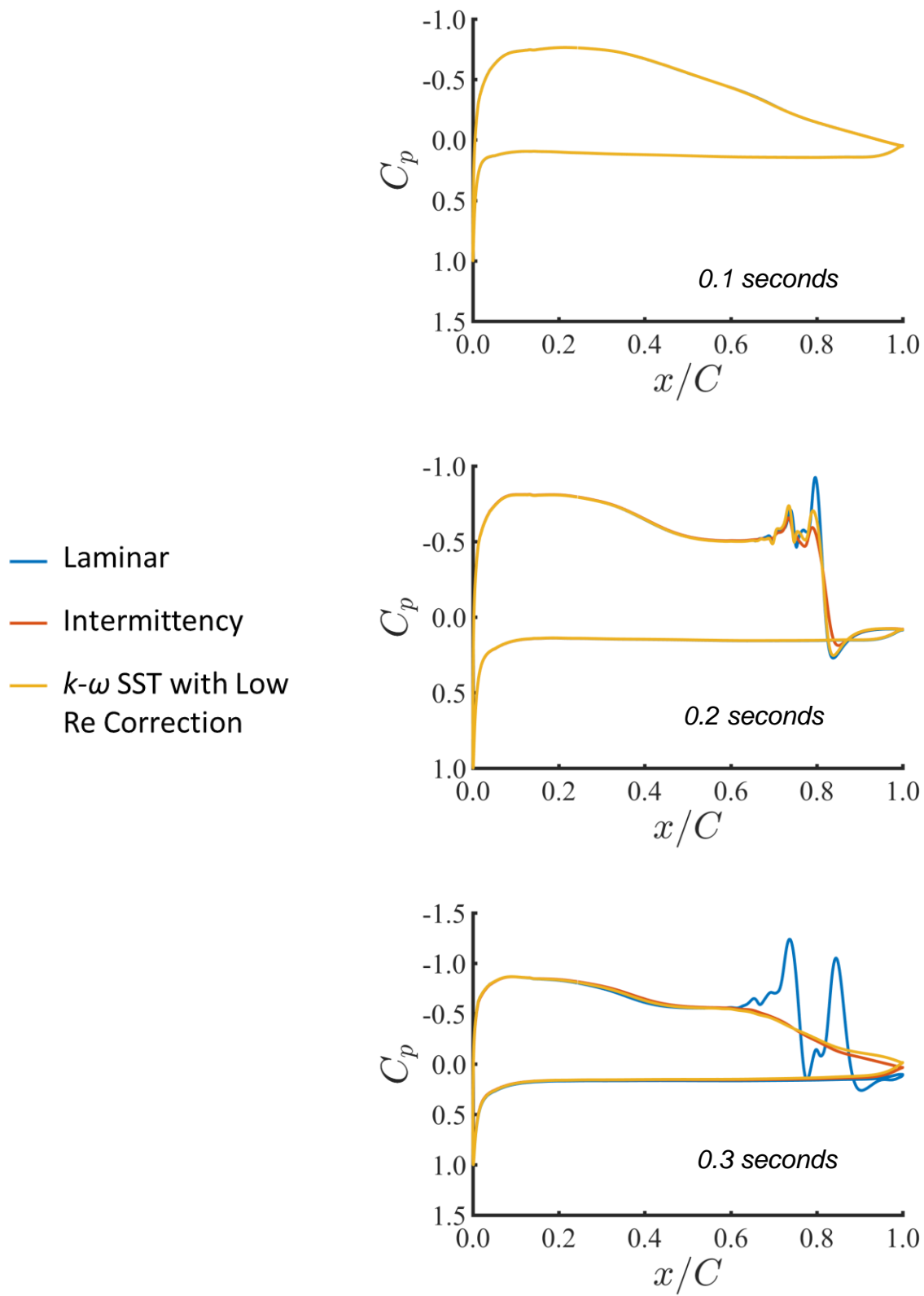


Figure 24. Pressure coefficient distributions at 0.1,0.2, and 0.3 seconds.

The $k-\omega$ SST model with low Reynolds number corrections is a low Reynolds number turbulence model whereas the intermittency model is a local correlation based transition model. In general, the local correlation based transition methods should predict better transition capabilities when compared to low turbulence model. However, in Figure 18, the $k-\omega$ SST model with corrections predicts slightly better drag data at high angles of attack when compared to the intermittency transition model. The reason for this behavior is currently not known and further investigation needs to be conducted to investigate this difference in data.

One of the major reasons to conduct the airfoil CFD analysis was to study the aerodynamic performance characteristics of the intermittency transition model available in ANSYS Fluent. The intermittency transition model captured the LSB and has good correlation with wind tunnel data at low to moderate angles of attack (-4° to 4°). Beyond 4° , the intermittency transition tends to over predict the drag data. This discrepancy may be attributed to two reasons: the typical numerical dissipation effects due to the employment of RANS modeling and the intermittency transition model errors. Furthermore, this discrepancy highlights the limitation of using intermittency transition model at high angles of attack where the airfoil experiences significant adverse pressure gradients and turbulent flow separation. The over-prediction of drag data may indicate the imbalance of laminar and turbulent regions about the airfoil predicted by the transition model i.e., the transition onset and length of transition might not have been determined accurately.

The COMP propeller blade has high pitch angles towards the blade root. Therefore, based on the airfoil results, the implementation of intermittency model could

affect the propeller axial force (torque) prediction. However, the transition characteristics might be affected significantly due to the spanwise turbulence variation (z – direction) and the same trends/discrepancies may not be present for the three-dimensional analysis.

6.2 COMP Propeller

6.2.1 Propeller Geometry

In Ghoddoussi's work, the wind tunnel test models consist of propellers with a spinner and nacelle [15]. The COMP propeller has four variants of propeller blade pitch angle (measured at reference station): 15°, 20°, 25°, and 30° [15]. The reference station for the blade pitch angles measurement is located at 0.75 times the propeller radius. In the current investigation, the COMP propeller with a blade pitch angle of 20° was chosen because the wind tunnel propeller slipstream characteristics are available only for this variant of the COMP propeller.

The first step was to generate the wind tunnel test model geometry for CFD analysis. Ghoddoussi provided a detailed description of steps to recreate the wind tunnel model in OpenSCAD. OpenSCAD is an open-source programming CAD software which outputs geometries in neutral file format such as Standard Tessellation Language (STL). However, due to the tessellated surfaces, it is difficult to directly handle STL format CAD in mesh generation software. Therefore, in the current investigation, the wind tunnel model geometry was recreated in CATIA v5 using the generative shape design module. In the wind tunnel model, a small gap exists between the spinner and nacelle. As this passage will not have significant effects on the propeller flow field, the geometry was modified to close this passage for the numerical model. This closed surface was named as "simplification surface." The recreated wind tunnel model with geometry modifications

is shown in Figure 25. Furthermore, the wind tunnel walls and support structures were not included in the numerical model. The resulting CAD was exported in STEP file format.

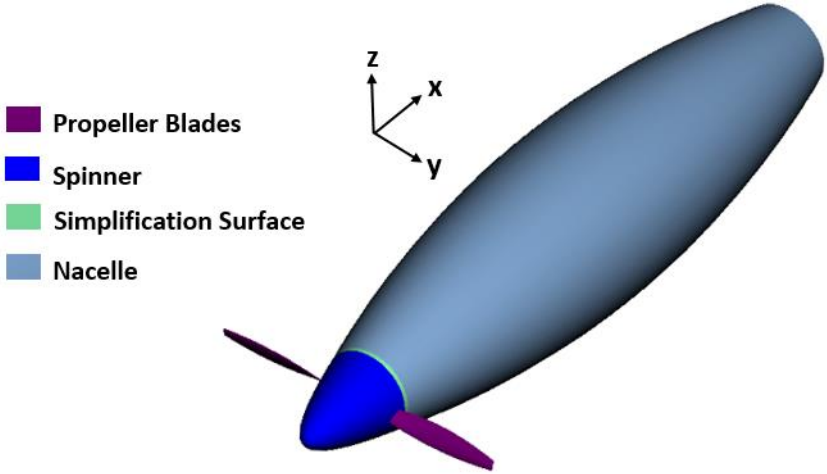


Figure 25. COMP geometry.

6.2.2 Secondary Characteristics Measurement Locations

The coordinate system, azimuth angle and slipstream velocity sign conventions provided for propeller secondary characteristics in Ghoudoussi’s document [15] are shown in Figure 26.

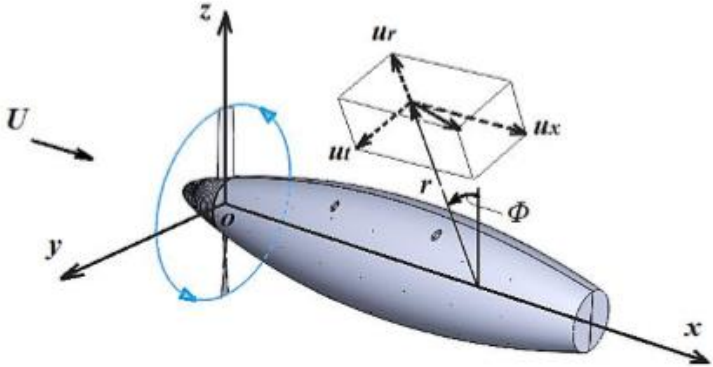


Figure 26. Sign conventions for propeller secondary characteristics provided in Reference [15].

The propeller wind tunnel data consists of secondary characteristics in terms of nacelle pressure distribution and slipstream velocities.

In the wind tunnel tests, the nacelle pressure data was collected about 4 longitudinal stations with varying azimuth angle, and extending along the complete nacelle length. This pressure distribution was measured by 8 pressure taps placed along each of the longitudinal stations. The details of the nacelle longitudinal stations is provided in Table 9 and represented in Figure 27.

TABLE 9
 NACELLE PRESSURE MEASUREMENT STATIONS

Reference label	Azimuth angle, Φ
NP_1	0°
NP_2	45°
NP_3	90°
NP_4	135°

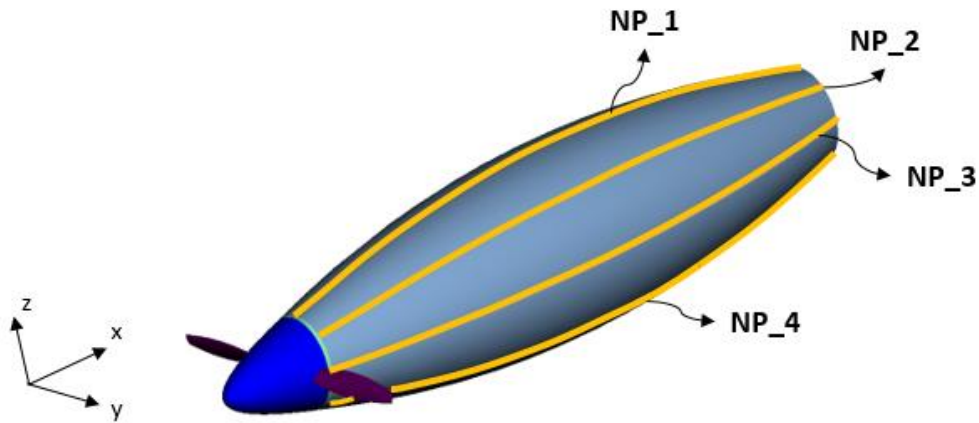


Figure 27. Nacelle pressure measurement locations.

The slipstream velocity components are expressed in cylindrical coordinate system, i.e., axial, tangential and radial components. These velocity components are measured about three cross sectional stations along the nacelle length. Furthermore, at

each cross sectional station, the slipstream velocities are provided for three azimuth angles, i.e., 0°, 90° and 270°. The nomenclature used in this document for slipstream velocity measurement locations are provided in Table 10 and shown in Figure 28.

The nacelle station, x/L , is the ratio of longitudinal distance from the nacelle leading edge (x) to the nacelle length (L). At these stations, each component of slipstream velocity is provided as a function of non-dimensional radius (r/R) which is defined as the ratio of radial distance from x -axis (“ r ” — shown in Figure 26) and the propeller radius (R), i.e., 0.1524 m.

In Figure 28, the red lines represent the stations about which the slipstream velocities were measured in the wind tunnel tests. The green lines represent the nacelle station and the blue circles have a diameter equal to 1.5 times the propeller radius (these circles indicate the end point of slipstream velocities measurement at each station).

TABLE 10

SLIPSTREAM VELOCITY MEASUREMENT STATIONS

Reference label	Nacelle station (x/L)	Azimuth angle, Φ
SV_1a	0.02	0°
SV_1b	0.02	90°
SV_1c	0.02	270°
SV_2a	0.49	0°
SV_2b	0.49	90°
SV_2c	0.49	270°
SV_3a	0.84	0°
SV_3b	0.84	90°
SV_3c	0.84	270°

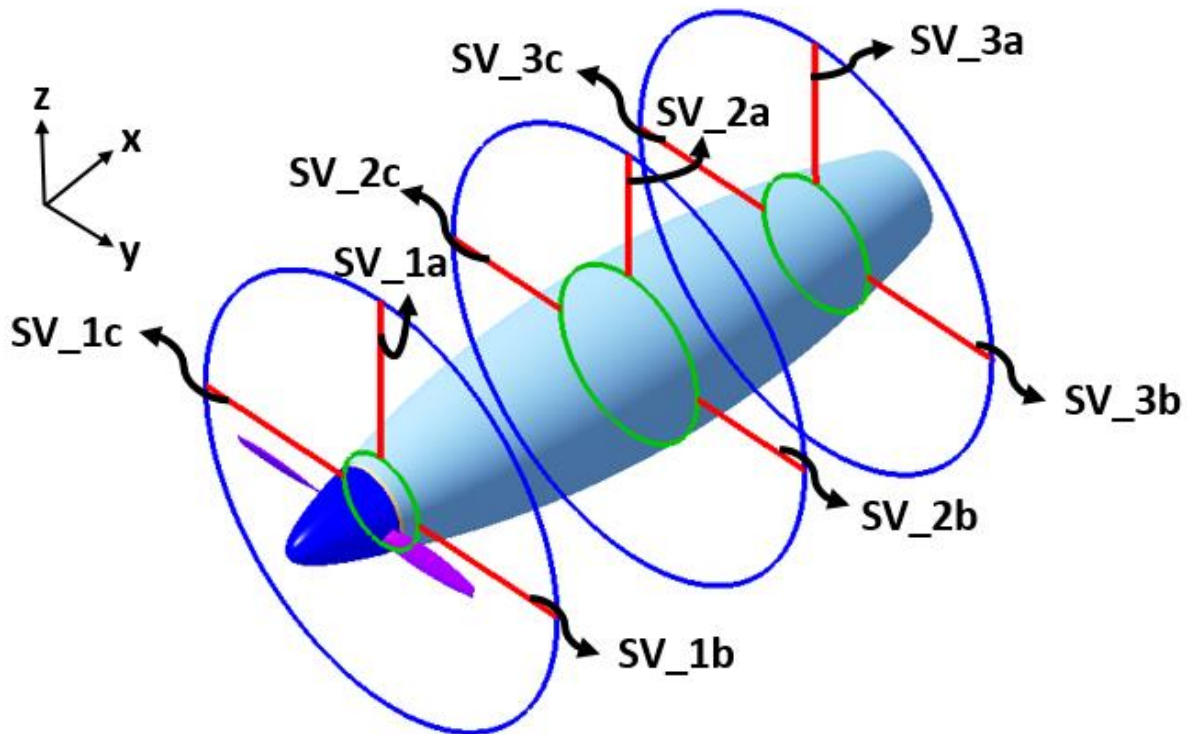


Figure 28. Slipstream velocity measurement stations.

6.2.3 Computational Fluid Dynamics

In the literature review, all the three CFD cases reviewed for propeller secondary characteristics estimation (provided in Section 3.2.2), chimera grids were used to simulate the propeller rotation. In rudimentary terms, a chimera grid for propeller simulations involves a multi-block approach in which the stationary regions of the numerical model are included in the background zone and the propeller is included in the component zone. However, in the current investigation, only unstructured grids were considered due to the limitations of resources. Few other methods in ANSYS Fluent to simulate propeller rotations include the Moving Reference Frame (MRF) and sliding mesh techniques. The sliding mesh approach provides time-accurate results whereas the MRF approach

provides time-averaged results. Therefore, due to better accuracy compared to MRF approach, the sliding mesh methodology was implemented in the current investigation

The computational domain type, extents and its associated boundary conditions for the propeller numerical simulations are shown in Figure 29. The computational domain extents were chosen based on information found in literature.

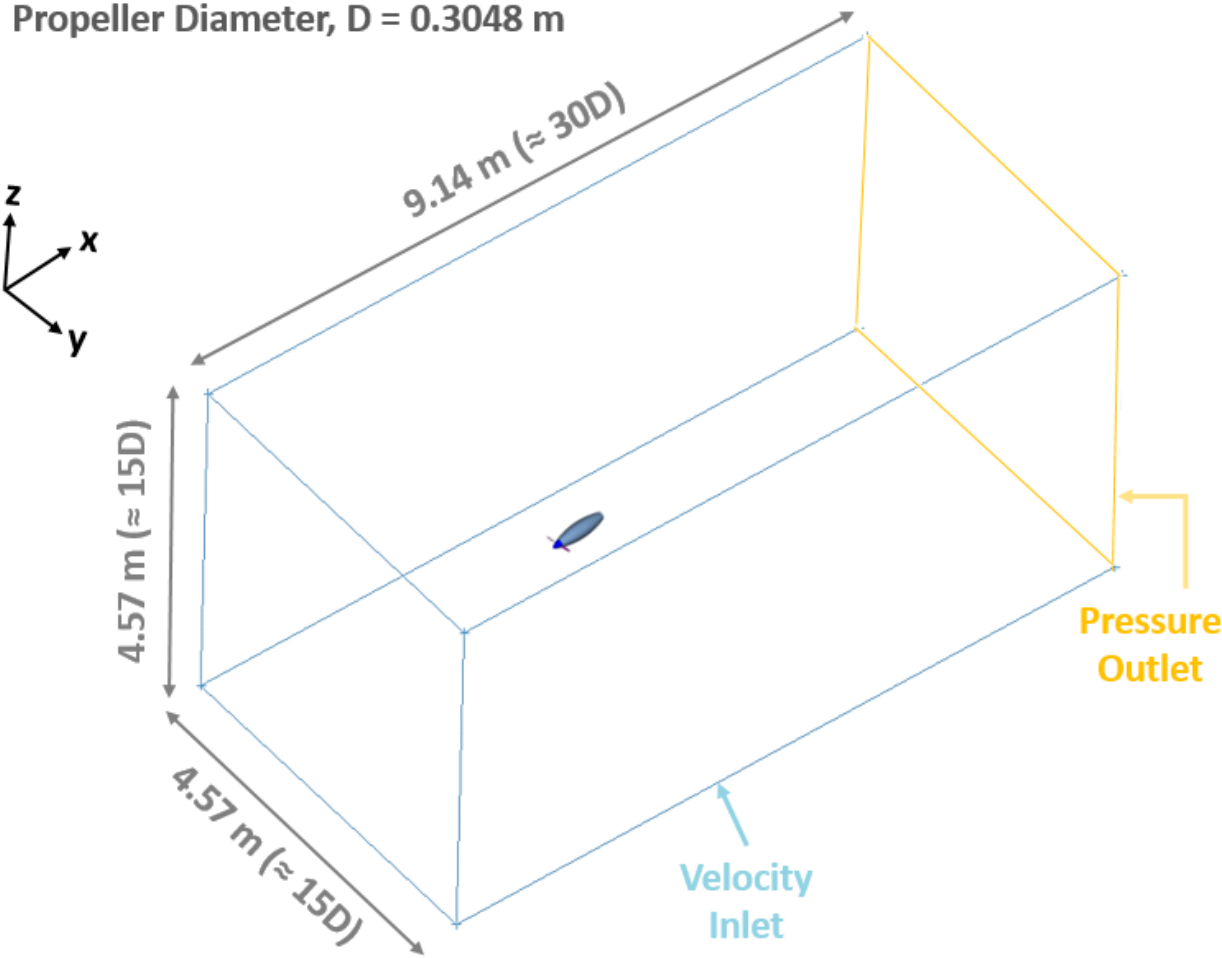


Figure 29. Numerical model details for COMP propeller CFD analysis.

The mesh consists of stationary and moving fluid domains for sliding mesh methodology. In the current propeller CFD simulations, the rotating (moving) domain is

assumed to encompass the propeller blades and spinner. Consequently, the simplification surface and nacelle are in the stationary domain. For simplicity, the rotation domain shape was assumed to be a cylinder. However, an inherent limitation associated with this assumption was that along with the propeller and spinner surfaces, all the volume cells in the cylindrical domain are rotating — which does not represent the actual flow scenario. The rotating and stationary fluid domain representations for the numerical model is shown in Figure 30.

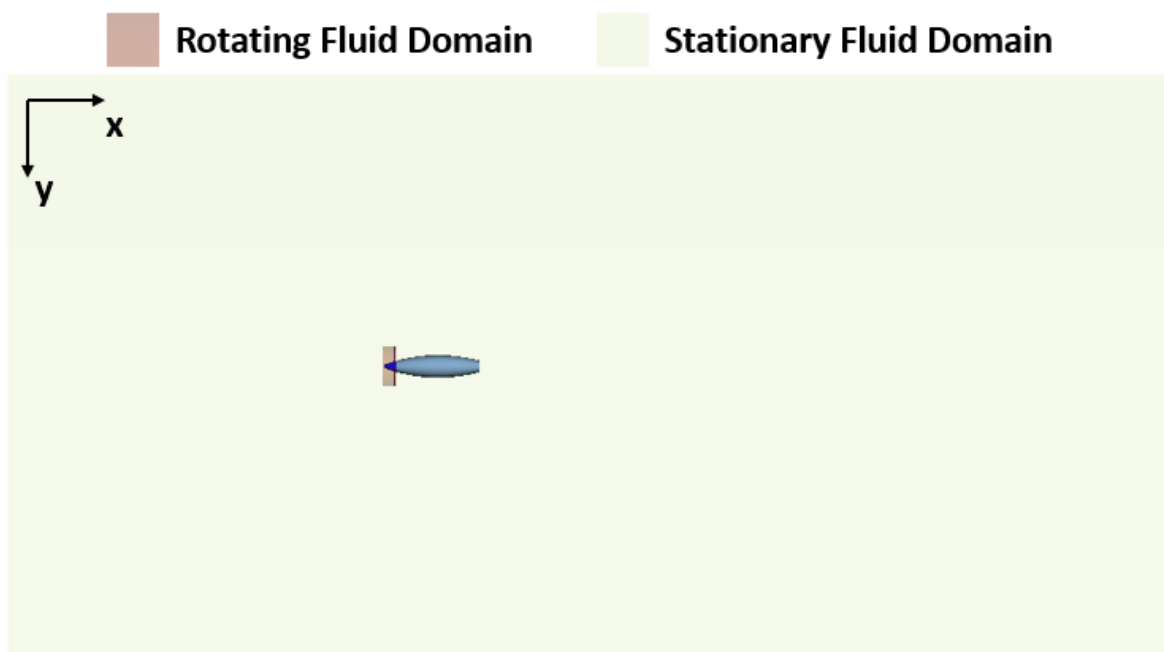


Figure 30. Schematic of fluid domains for sliding mesh technique.

The extents of the cylindrical domain were chosen such that at least two grid cells could be accommodated between the edges of propeller-spinner and the cylindrical domain itself. The extents of cylindrical domain are shown in Figure 31.

In a sliding mesh, the flow field information between the moving and stationary domains is exchanged via non-conformal interfaces. Therefore, in the present case, the surfaces of the cylindrical domain represent the non-conformal interfaces.

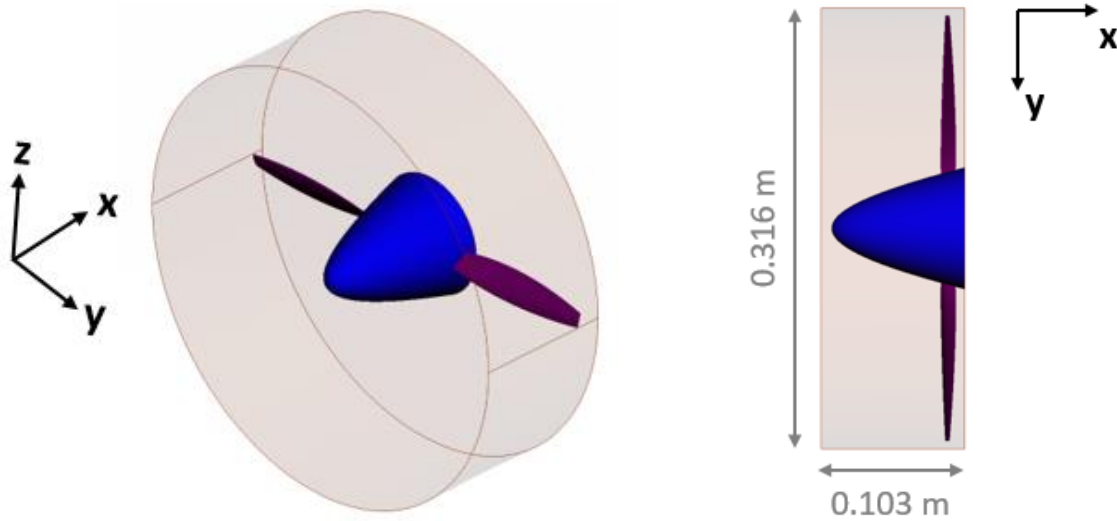


Figure 31. Rotating fluid domain components and extents.

The operating pressure, temperature and propeller rotational speed specified for the CFD analysis correspond to the wind tunnel operating conditions. For the given operating pressure and temperature, from the equation of state, the fluid density is approximately 1.146 kg/m^3 . Based on the operating conditions and a reference length of 0.0191 m (propeller chord length at 0.75 times of propeller radius), from equation (11), the propeller Reynolds number is approximately 92,300. Further, the propeller tip Mach number is 0.28. Therefore, these operating conditions represent a subsonic (incompressible) flow field.

Similar to the airfoil numerical analysis presented in Section 6.1.2, the computational boundaries for the propeller-nacelle study were also placed significantly far away from the propeller-nacelle in all directions because of the low operating velocity, as shown in Figure 29. From preliminary CFD analysis, it was observed that there were no significant pressure gradients across the computational domain boundaries indicating that the domain boundaries are located sufficiently far from the propeller. Therefore, this domain was used for all the propeller CFD analyses.

The meshes for all the propeller numerical simulations were generated using the BETA-CAE ANSA v17.0.3 software. In an attempt to capture the propeller wake, a cylindrical size box extending from the spinner to the downstream computational domain surface (outlet) was included. A fine volume mesh was required in the vicinity of the propeller and other wall surfaces, to capture the slipstream velocities accurately. As specifying a small mesh element size throughout the entire size box would drastically increase the overall mesh size, this cylindrical size box was divided into two parts as shown in Figure 32.

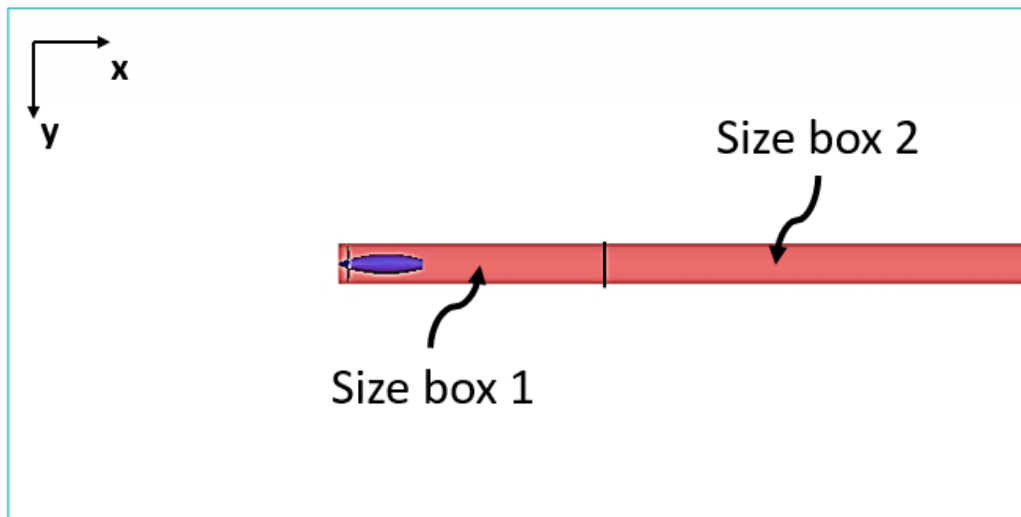


Figure 32. Size boxes to capture propeller wake.

Hybrid meshes were generated to capture the boundary layer characteristics using prism cells in the vicinity of the wall surfaces and tetra cells in the remaining region. A wall Y^+ less than 1 is desired to resolve the boundary layer accurately. For the given operating conditions and reference length of 0.0191 m, the first mesh cell was placed at a distance of 4×10^{-6} m normal to the wall surfaces to obtain a wall Y^+ of 1. To ensure that the wall Y^+ is less than 1, a first cell height of 2.5×10^{-6} m is specified for all the wall

surfaces. In addition, the specified number of layers and boundary layer growth rate were 20 and 1.2 respectively. The boundary layer growth was based on the exponential growth law. ANSA includes a feature of “additional outer layers” which provides a smooth transition between the prism and tetra cells. Therefore, in addition to the 20 layers, 10 outer layers were also included.

In the current investigation, the non-conformal interfaces were defined by importing rotating fluid domain and stationary fluid domain meshes separately in ANSYS Fluent. First, the rotating fluid domain mesh is imported and then the stationary fluid domain mesh is appended to the rotating fluid domain mesh. If the mesh connectivity was not defined correctly in the mesh generation phase, it would cause problems while defining interfaces in Fluent. One of the most problematic regions in terms of connectivity is the boundary layers on the interface, connecting both the rotating and stationary fluid domains. Therefore, to ensure a proper set-up of the numerical model for CFD analysis, the boundary layers for both rotating and stationary fluid domains were generated simultaneously using the batch mesh manager tool in ANSA. This was performed by including two “layer areas” under one “layers session” in the ANSA batch mesh manager. The first layer area consisted of propeller and spinner, whereas the second layer area was the simplification surface and nacelle. To obtain proper connectivity, the cylindrical domain has to be visible during boundary layer generation.

The cylindrical domain surfaces were assigned an interface boundary condition in ANSA. After the surface, prism layers and tetra volume mesh generation, the rotating and stationary fluid domains were exported out as separate mesh files.

The ANSYS Fluent settings used for the propeller numerical simulations were identical to the Eppler 387 CFD analysis (Section 6.1.2) because of the similar operating Reynolds number and implementation of the same turbulence model.

The sliding mesh approach is applicable only to unsteady calculations. The time-accurate CFD analysis were conducted using ANSYS Fluent Release 18.2 with double precision enabled. The pressure-based solver with incompressible-ideal-gas law density model was used. Based on the wind tunnel operating conditions, a dynamic viscosity of 1.8535×10^{-5} kg/m-s was obtained using the Sutherland's law. Therefore, in ANSYS FLUENT, a constant viscosity of 1.8535×10^{-5} kg/m-s was specified along with an operating pressure of 97,530 N/m². Based on the turbulence models comparison study in Section 6.1.2, the intermittency viscous model was used for propeller analysis. In the cell zone conditions, for volumes associated with the rotating components, the mesh motion option was enabled. In the mesh motion options, the rotation axis and rotational velocity were specified as x-axis and 6,000 RPM respectively.

When meshes were exported from ANSA, the cylindrical domain surface is split into two parts: one part containing only the quadrilateral cells (connecting the prism layers of the two fluid domains) and the other part containing only triangular cells (connecting the tetrahedral volume cells of the two domains). Therefore, two mesh interfaces were defined in ANSYS Fluent.

During the mesh generation, a single set of cell nodes on the interface connect the rotating and stationary fluid domains. However, during the simulation when the rotating region slides with respect to the stationary region, the cell nodes may not match at the

cylindrical domain interface. Therefore, the cylindrical surfaces were defined as non-conformal interfaces in ANSYS Fluent.

The wind tunnel data for COMP propeller consists of slipstream characteristics only for an advance ratio of 0.67. Therefore, the preliminary CFD analysis were conducted at the aforementioned advance ratio. For an operating Reynolds number of approximately 100,000 and propeller rotational velocity of 6,000 RPM, an operating velocity of 20.4 m/s is required to obtain an advance ratio of 0.67. Therefore, a freestream velocity of 20.42 m/s was specified at the inlet. The gauge pressure and thermal conditions at the inlet as well as outlet were 0 N/m² and 296.5 K respectively. Further, at both the inlet and outlet — the intermittency, turbulence intensity and viscosity ratio values were 0.5, 0.1%, and 1 respectively. In addition, all the wall surfaces were specified to have no-slip shear condition with zero heat flux and zero heat generation rate.

Due to the implementation of intermittency model, a coupled algorithm was used to aid in solver convergence. A second-order upwind scheme was used for the spatial discretization of all the scalar transport variables. Their gradients and derivatives were evaluated using the least squares cell-based scheme. The second-order pressure interpolation scheme was used for the pressure gradient term. In addition, a second-order implicit formulation was used for temporal discretization. The default solver residual values were used for convergence criteria. The variation of thrust and torque values were also monitored to ensure solver convergence.

A flow courant number of 100 was specified and the explicit relaxation factor for momentum was reduced from 0.75 to 0.6. Furthermore, the under-relaxations for density

was also reduced to 0.8. The solver default relaxation factors were used for all the remaining transport variables.

In Ghoudoussi's work [15], the azimuth angle parameter was defined as the angle between the pressure ports and the longitudinal plane (XZ plane). In the current investigation, a similar parameter is required to quantify the propeller angular position in CFD simulations. The blade orientation could also be quantified using the azimuth angle parameter. However, to avoid confusion, an additional parameter known as the blade orientation angle is used in the current investigation to identify propeller blade orientation.

As shown in Figure 33, the propeller blade orientation angle is assumed to be the angle between the line passing through both the propeller tips in the spanwise direction, and the y-axis. In the current investigation, the propeller rotation starts from the y-axis and rotates in the clockwise direction when viewed from the front.

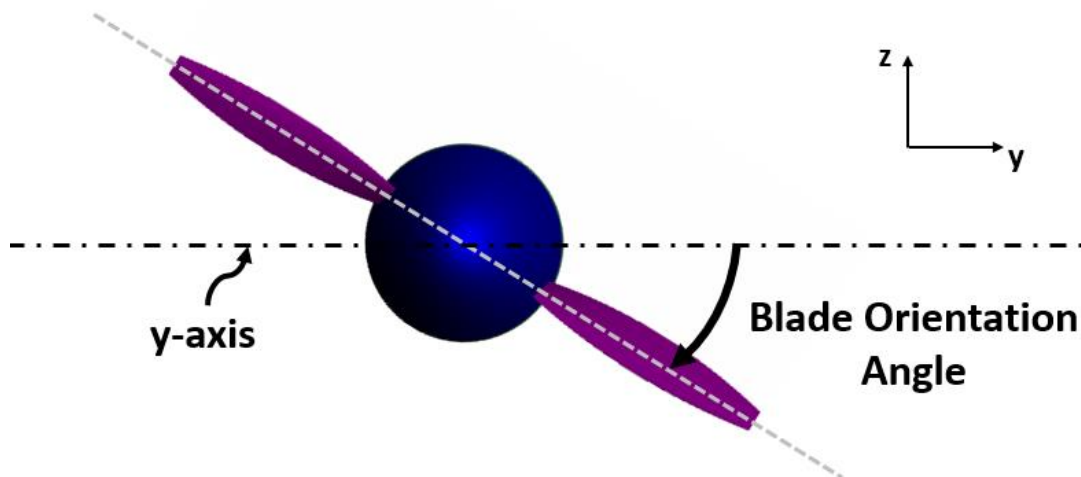


Figure 33. Propeller blade orientation angle.

The recommended time-step for propeller CFD analysis is the time taken to rotate the propeller by 1° [42]. In this case, the time taken to rotate the COMP propeller by 1°

with a propeller angular velocity of 6,000 RPM, is approximately 2.778×10^{-5} seconds. In addition, 5 inner iterations were allowed for each time-step.

In section 6.1.2, the solver outputs were exported as dimensionless coefficients (lift, drag and pitching moment coefficients). However, in the propeller analysis, the solver reference values were set to output the forces and moments instead of dimensionless coefficients. The propeller torque was measured about the x-axis.

6.2.3.1 Grid Independence Study

A grid independence study was conducted to check the effect of spatial discretization errors on the propeller primary as well as secondary characteristics. This study included three grids (coarse, medium and fine) with increasing grid resolution on the wall surfaces and the propeller wake region. The grid resolution was increased by reducing surface element size on wall surfaces, interfaces, computational domain and size boxes. The boundary layer mesh properties such as the first cell height, growth rate and number of layers were the same for all the three meshes. As shown in Figure 32, the coarse and medium meshes have two cylindrical size boxes to capture the propeller wake. However, an additional size box was included in the fine mesh to obtain a higher grid resolution in the propeller-wake region. For the fine mesh, size box 1 in Figure 32, was further split into two cylindrical domains and a significantly lower mesh size was allotted to the size box containing the propeller-nacelle geometry.

The mesh size details for each grid is provided in Table 11. In this table, the surface mesh size does not include computational domain surface elements. A typical surface mesh used in the current investigation is shown in Figure 34 and a comparison of grid resolution in the propeller-wake region for the three meshes is shown in Figure 35.

TABLE 11

DETAILS OF MESHES USED IN PROPELLER GRID CONVERGENCE STUDY

Mesh size	Coarse	Medium	Fine
Surface mesh (million cells)	≈ 0.16	≈ 0.36	≈ 0.49
Prism cells (million cells)	≈ 4.55	≈ 10.82	≈ 14.77
Total volume mesh (million cells)	≈ 6.90	≈ 17.04	≈ 43.91

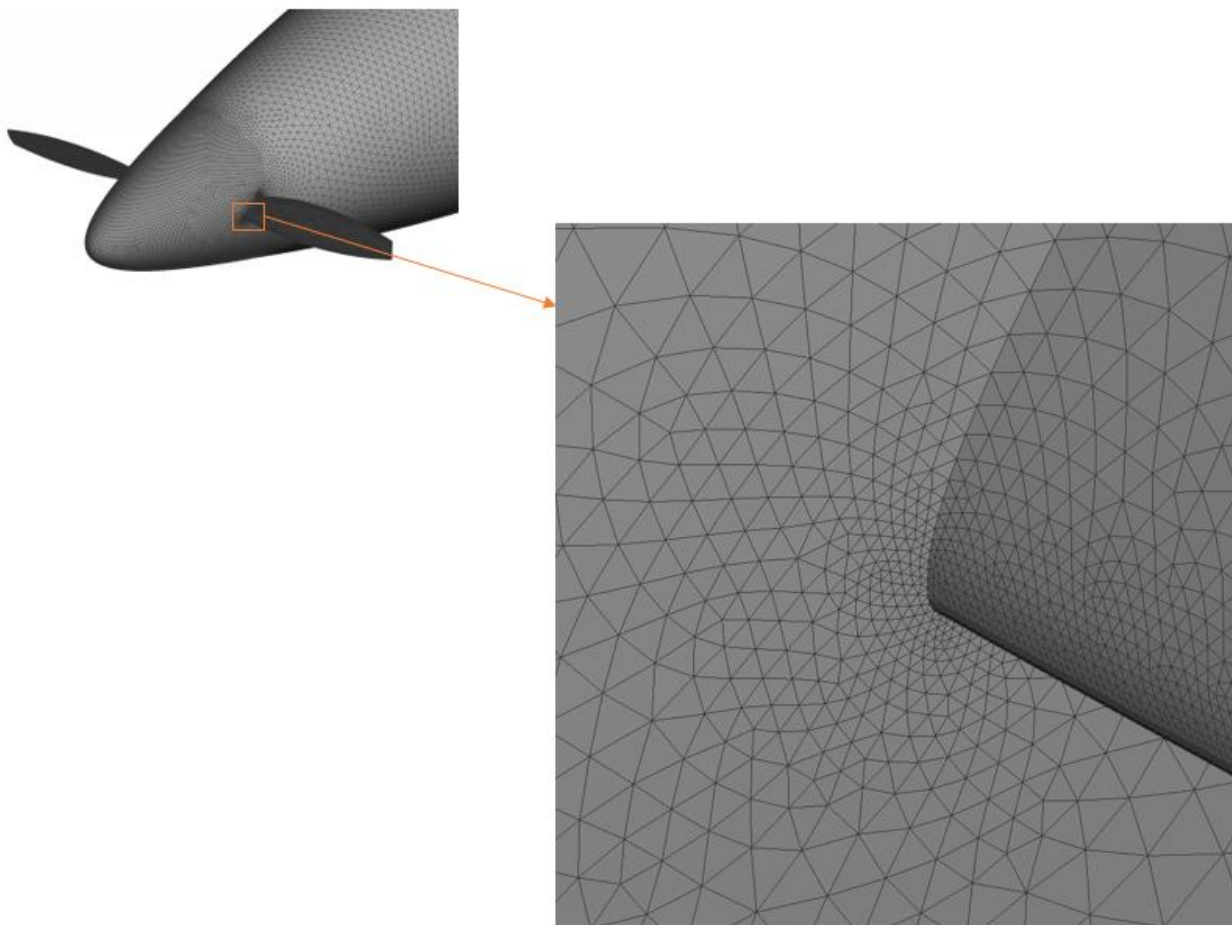
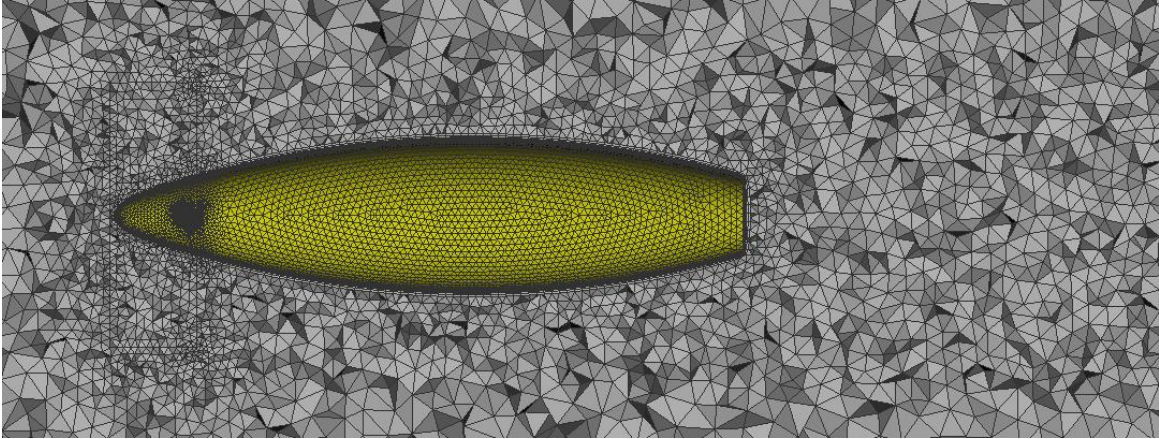
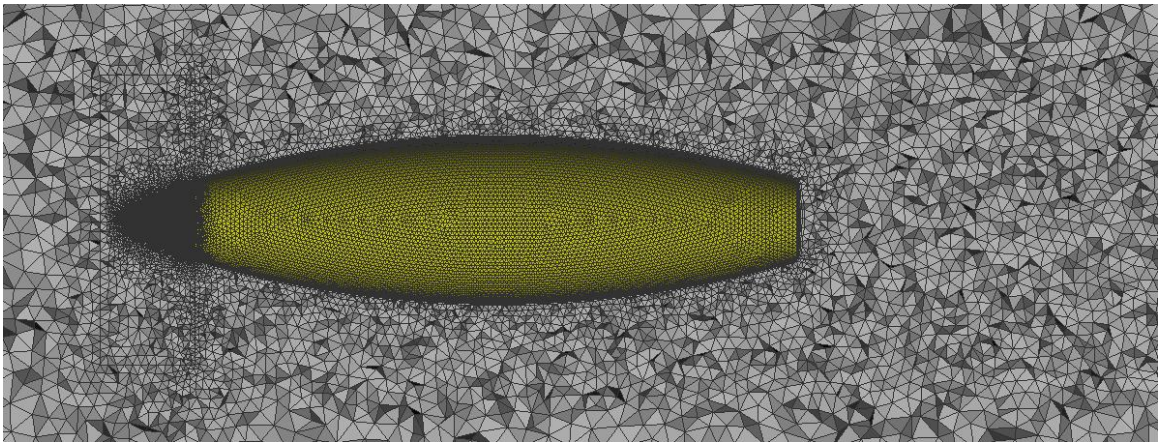


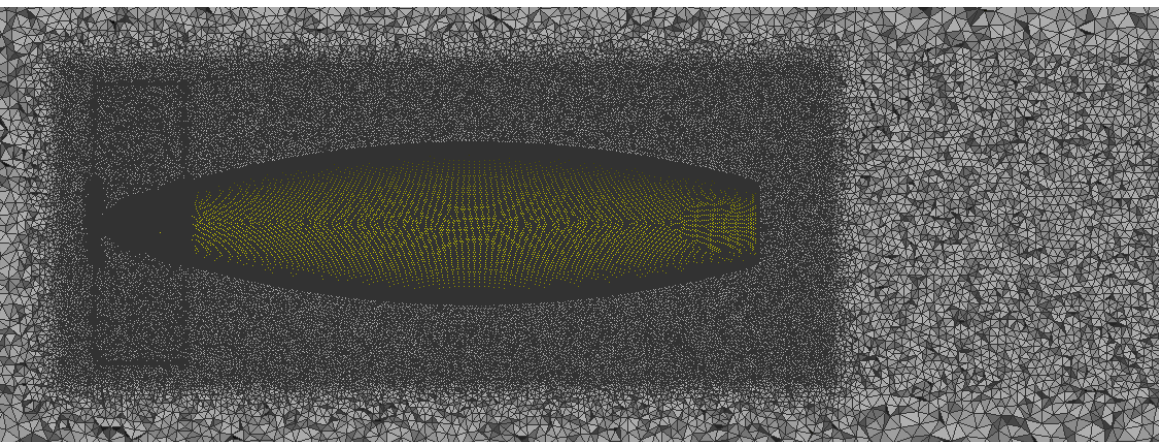
Figure 34. Schematic of surface mesh associated with medium mesh.



(a) Coarse mesh.



(b) Medium mesh.



(c) Fine mesh.

Figure 35. Comparison of grid resolution in propeller-wake region.

The transition of volume cells from prism layers to tetrahedral cells about a propeller blade section is shown in Figure 36.

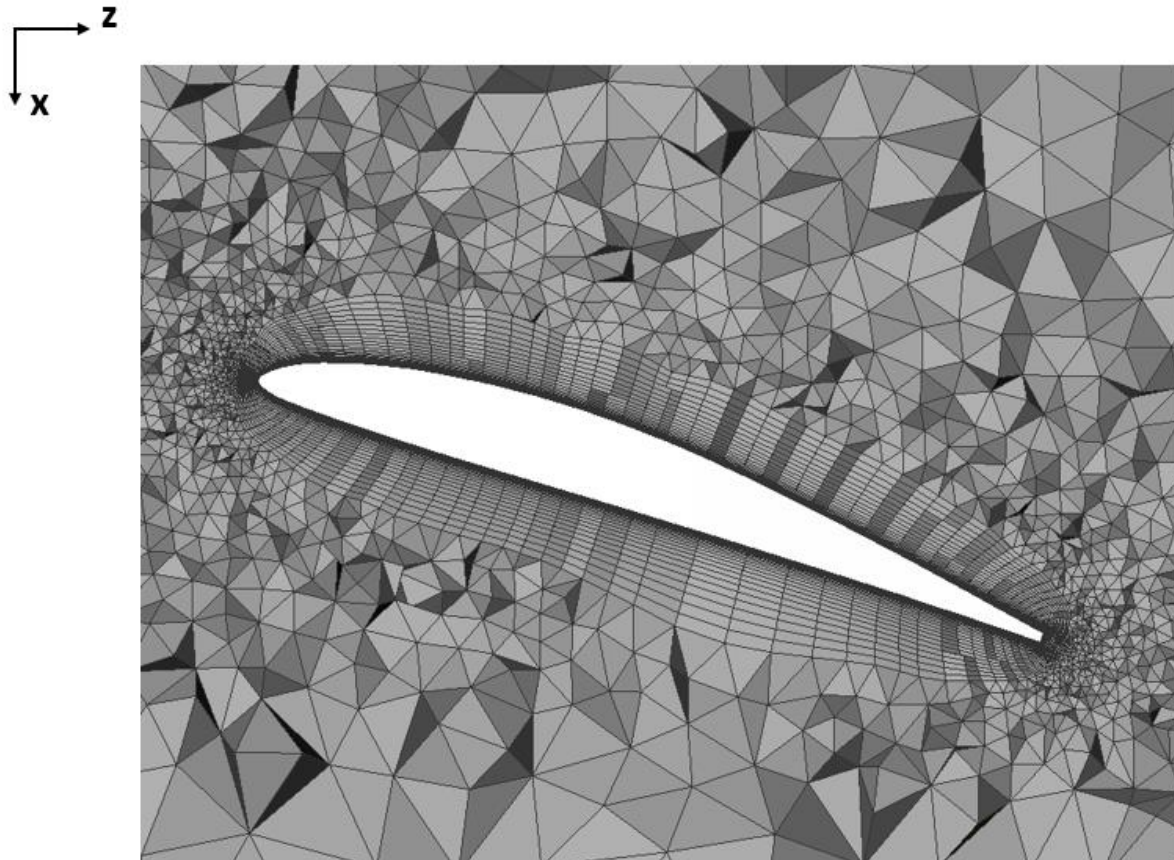


Figure 36. Schematic of volume cells transition in medium mesh.

The grid independence study was conducted for an advance ratio of 0.67. As the CFD simulations were conducted with a time-step size of 2.778×10^{-5} seconds, 360 time-steps are required to simulate one propeller rotation, i.e., one propeller rotation is completed in every 0.01 seconds. The simulations were stopped at the end of 8th propeller rotation as the propeller thrust and torque did not vary significantly beyond this point.

The time history of propeller thrust and torque — from the end of 1st to the end of 8th rotation are shown in Figures 37 and 38. These convergence histories correspond to the medium mesh. As the propeller thrust and torque are oscillating with constant

amplitude, these quantities were averaged from the end of 7th rotation to the end of 8th rotation, i.e., from 0.07 to 0.08 seconds.

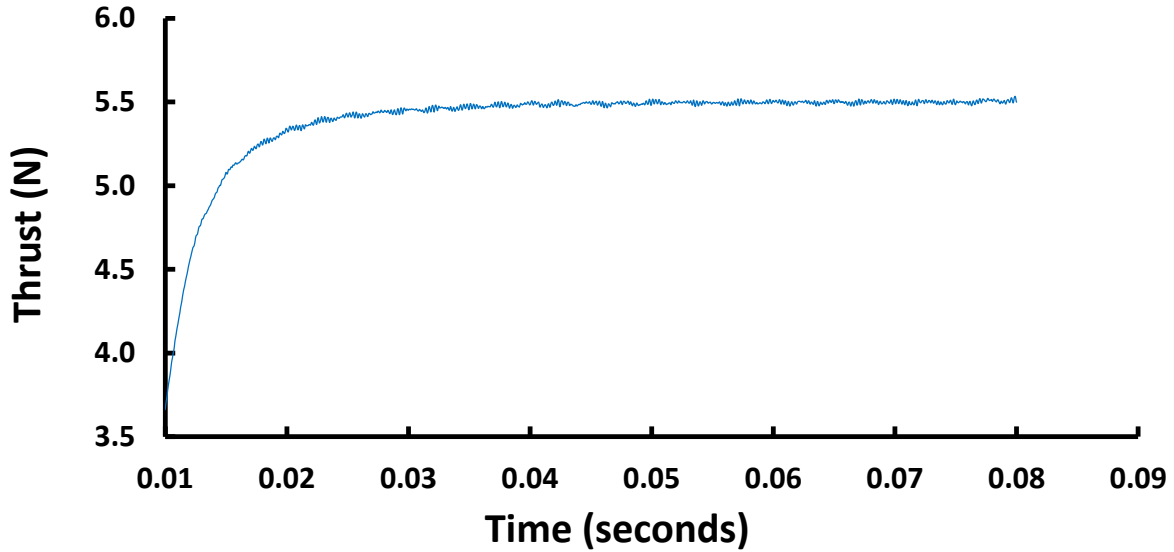


Figure 37. Time history of propeller thrust variation at $J = 0.67$.

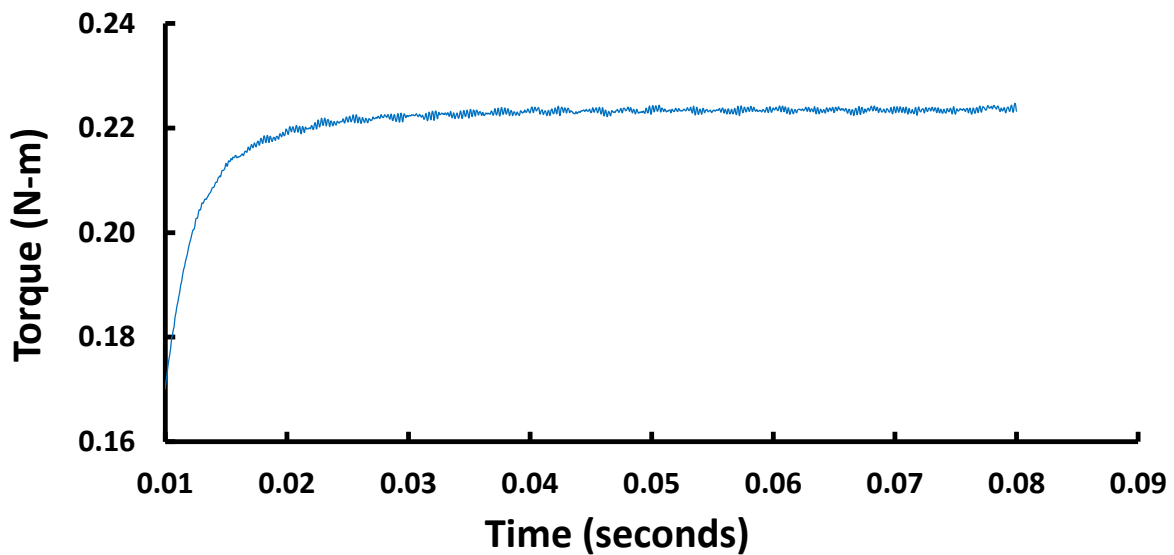


Figure 38. Time history of propeller torque variation at $J = 0.67$.

The first segment of the grid convergence study dealt with the variation of propeller primary characteristics (thrust and torque) with increasing grid resolution. The propeller

thrust and torque values obtained for the three meshes were compared with wind tunnel data in Figures 39 and 40. In these plots, “WT” indicates wind tunnel data.

The simulations corresponding to coarse and medium meshes were performed on Intel Xeon X5675 machine. The fine mesh has a significantly larger mesh size when compared to the coarse and medium meshes. Therefore, the fine mesh required greater computational power and it was not feasible to conduct CFD analysis for the fine mesh on 12 core Intel Xeon X5675 machine to obtain results in a reasonable time period. Consequently, the simulation for fine mesh was conducted on Intel Xeon E5-2699 v3 machine using 16 cores. The computational (wall-clock) time for each mesh is shown in Figure 41. It is to be noted that this computational time plot is provided only for illustration purposes only. It is not intended to compare the computation time for the three mesh cases as they were not conducted on similar machine configurations.

The variation in propeller thrust and torque values for increasing grid resolution was less than 5%. Therefore, grid convergence was achieved in terms of the propeller primary characteristics.

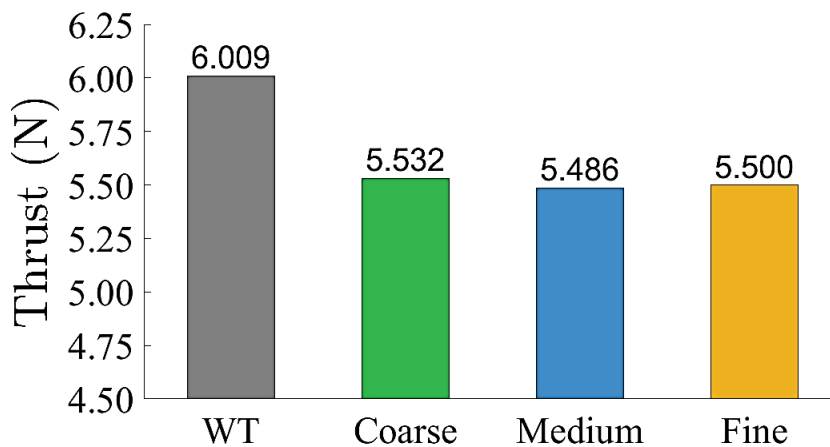


Figure 39. Variation in thrust force with varying mesh sizes.

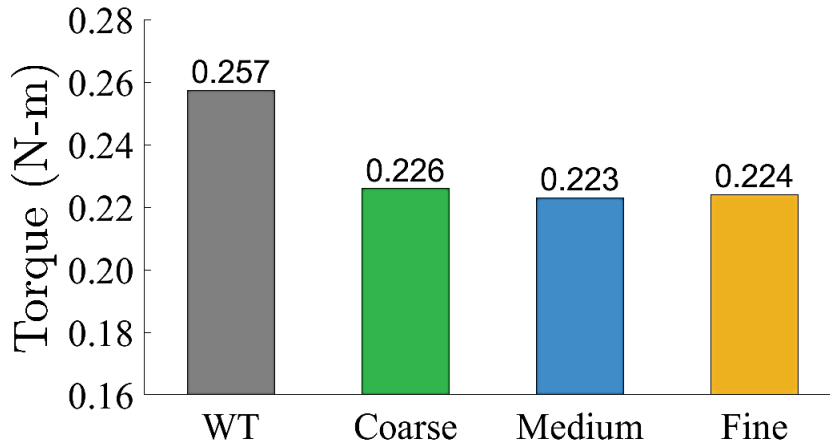
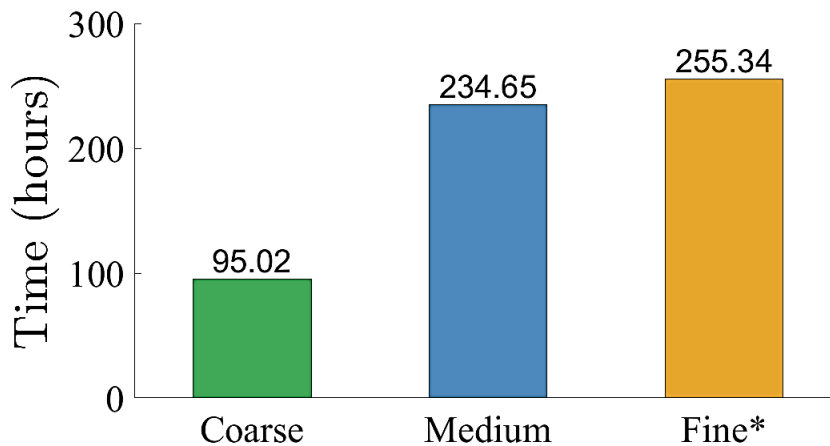


Figure 40. Variation in torque moment with varying mesh sizes.



* Unlike the coarse and medium meshes, the fine mesh simulation was performed using 16 cores on Intel Xeon E5-2699 v3 machine.

Figure 41. Computation time for the three meshes in the grid independence study.

The grid resolution in the propeller wake region may affect the secondary characteristics estimated using CFD analysis. Therefore, for the second segment of the grid convergence study, the variation in nacelle pressure about station NP_1, and slipstream velocity components at station SV_1a were considered. The secondary characteristics obtained for the three meshes are compared in Figures 42 to 45.

The secondary characteristics in Figures 42 to 45, represent the averaged values from the end of 7th rotation to the end of 8th rotation. These comparisons do not include wind tunnel because the subtle differences in the numerical results for each mesh is not noticeable if the wind tunnel data were also included in the plots. A detailed explanation of the propeller secondary characteristics averaging is provided in Section 6.2.3.2.

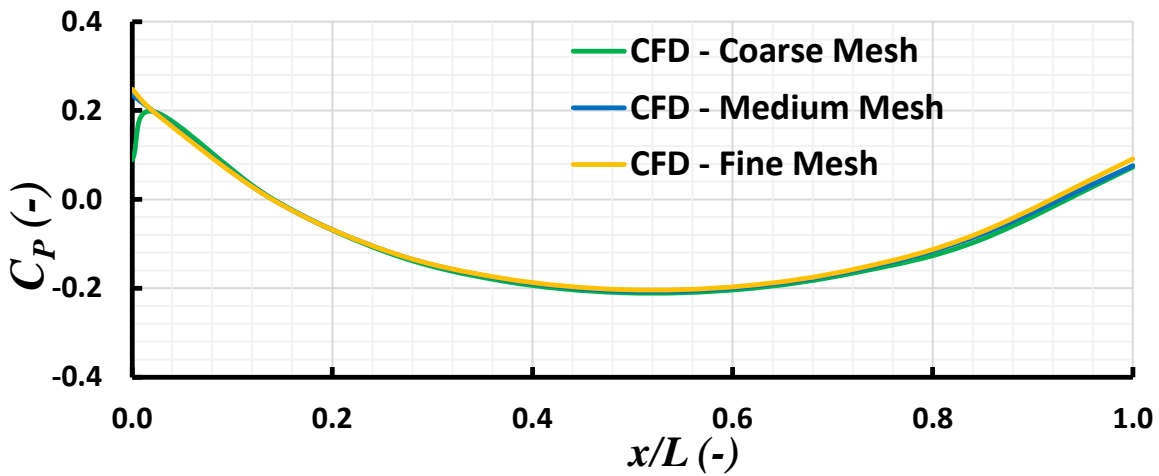


Figure 42. Comparison of nacelle pressure distribution at station NP_1.

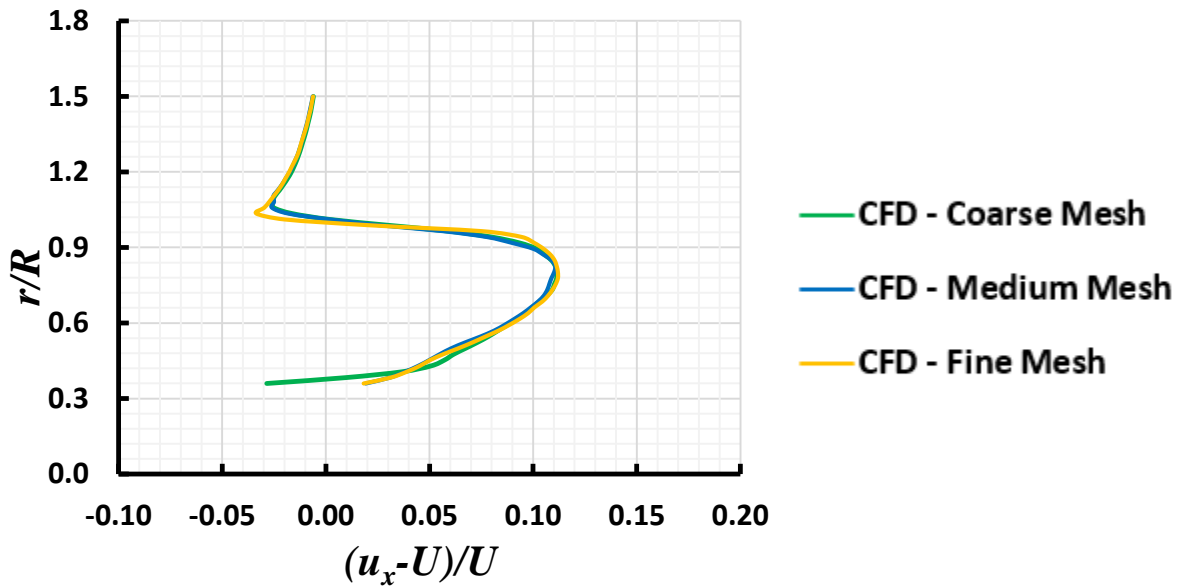


Figure 43. Comparison of axial slipstream velocity at station SV_1a.

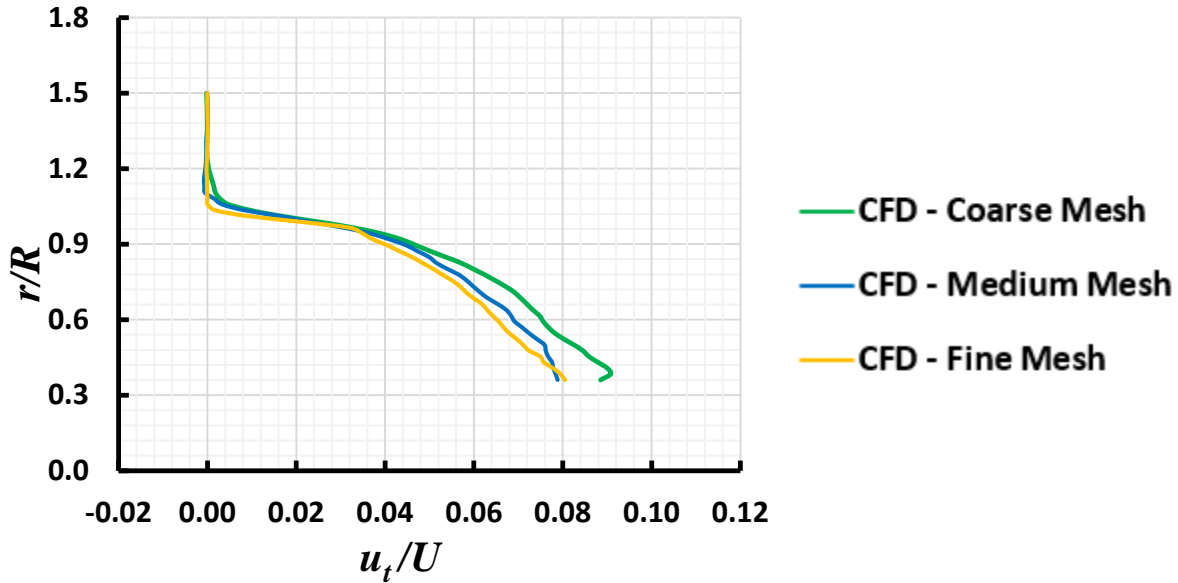


Figure 44. Comparison of tangential slipstream velocity at station SV_1a.

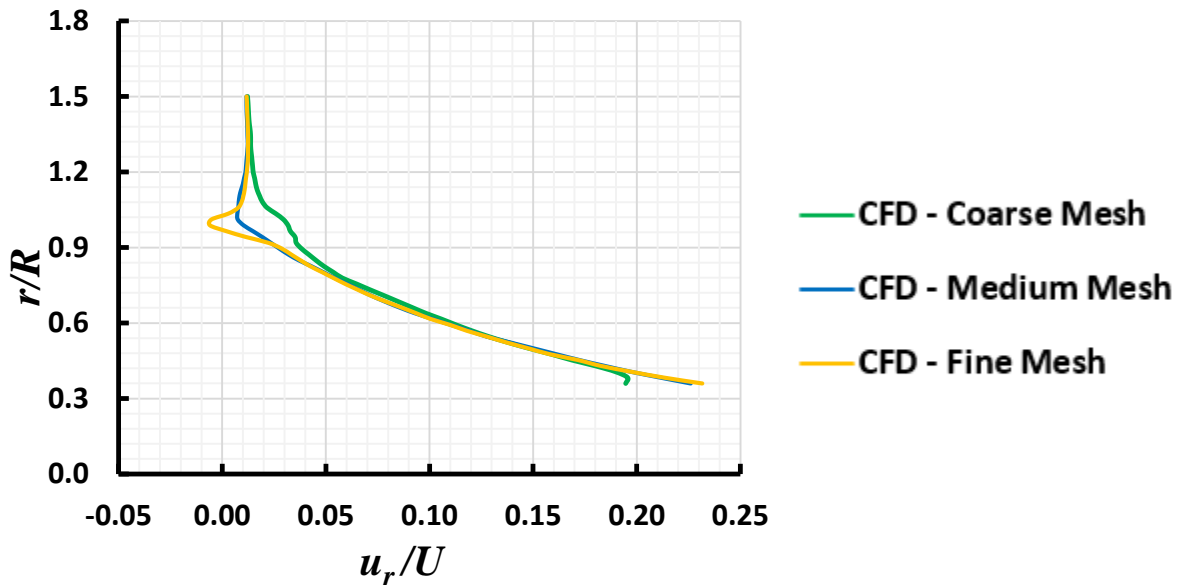


Figure 45. Comparison of radial slipstream velocity at station SV_1a.

The nacelle pressure distribution obtained for the coarse mesh deviates from the medium and fine meshes results at the nacelle leading edge extremity locations i.e., x/L varying from 0 to 0.02. In addition, the fine mesh predicts a slightly larger pressure suction for x/L greater than 0.85.

In the case of axial component of slipstream velocity, there is no significant variation in velocity for the non-dimensional radius distance varying from 0.38 to 1.5. However, near the wall surfaces, the coarse mesh results vary significantly compared to the medium and fine meshes. At high r/R values, the tangential velocities are identical for the three meshes. However, at low r/R values, the variation in tangential velocity from medium mesh to fine mesh is lower than the tangential velocity variation from coarse mesh to medium mesh. Therefore, the reducing variation with increasing grid resolution may indicate grid convergence. The non-dimensional radius r/R of 1, represents the radial location for the propeller blade tip. The radial velocities obtained from all the three meshes are identical throughout all the radial distances except at the propeller tip region. The variation in nacelle pressure distribution and slipstream velocity components highlight the sensitivity of propeller slipstream characteristics to grid resolution. Therefore, in spite of good grid convergence obtained for primary characteristics, the coarse mesh was not considered for further CFD analysis.

In the current investigation, the main objective of conducting further COMP CFD analysis were to:

- 1) Compare the propeller primary characteristics with wind tunnel data for varying advance ratios.
- 2) Compare the propeller secondary characteristics with wind tunnel data at an advance ratio of 0.67.

Based on the current grid convergence study, medium mesh results did not vary significantly compared to the fine mesh in terms of primary characteristics. Therefore, the medium mesh was used for predicting primary characteristics at different advance ratios.

Due to the availability of medium and fine mesh results from grid independence study, the propeller secondary characteristics for both medium and fine meshes were compared with wind tunnel data at an advance ratio of 0.67.

6.2.3.2 Assumptions for Propeller Secondary Characteristics Obtained from CFD Analysis

The two major assumptions for the numerical propeller secondary characteristics distributions in the current investigation were to:

- Exclude the slipstream velocities in the close vicinity of the wall region.
- Average the nacelle pressure and slipstream velocities for 1 propeller rotation.

As mentioned in Section 6.2.3, a no-slip wall boundary condition was prescribed on the wall surfaces in the COMP numerical model. A no-slip conditions indicates that the velocity on wall surfaces is zero in the CFD analysis. However, the wind tunnel data does not include slipstream velocities in the close vicinity of surfaces of the COMP model. Therefore, only for comparison purposes, the numerical slipstream velocities distributions presented in the current investigation does not include the zero-velocity at the wall surface. For example, at station SV_1a, the radial distance extremity limits are 0.0438 m (represents the radius of the nacelle cross section at $x/L=0.02$) and 0.228 m (represents the radius of blue circles shown in Figure 28). A typical axial slipstream velocity distribution at this station, for radial distance varying from 0.0438 m and 0.228 m is shown in Figure 46. This CFD data corresponds to fine mesh at an advance ratio of 0.67 at 0.07 seconds. The axial velocity (u_x) at the radial distance of 0.0438 m is 0 due to the no-slip wall conditions. Therefore, at this point, the axial velocity ratio is -1 .

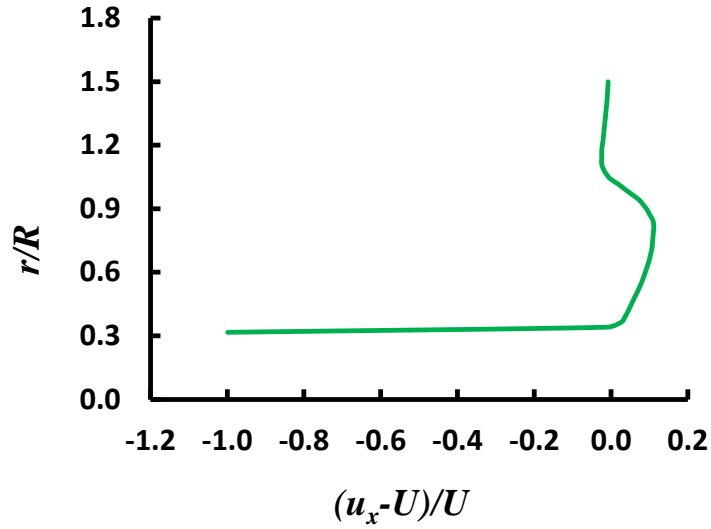


Figure 46. Axial slipstream velocity distribution with wall surface velocity.

Figure 47 illustrates the slipstream velocity data after eliminating the radial data in the vicinity of wall surface which, as shown in Figure 46 can be deemed insignificant. In Figure 47, the radial distance varies for 0.054 m to 0.228 m. Hence, in the current investigation, a small portion of radial distance near the wall surface was excluded for wind tunnel – CFD slipstream velocity comparisons.

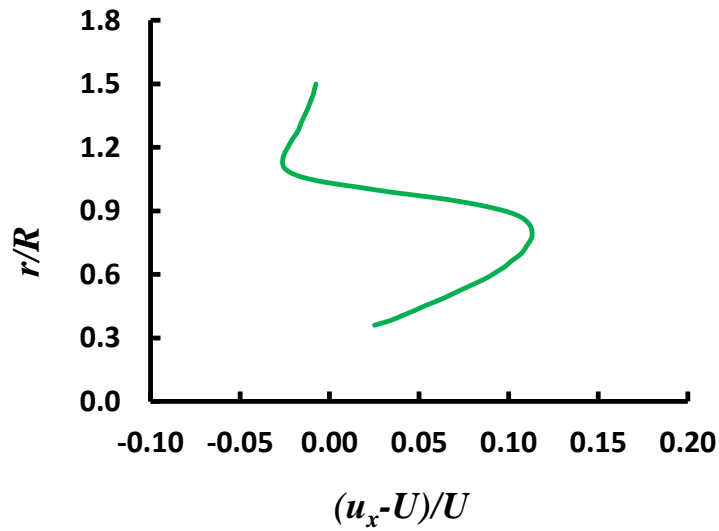


Figure 47. Axial slipstream velocity distribution without wall surface velocity.

During the CFD analysis, the propeller secondary characteristics data were saved for every 30° of propeller rotation in the 8th rotation. The nacelle pressure distribution and slipstream velocity components distributions during the 8th propeller rotation are shown in Figures 48 to 51. These plots correspond to the fine mesh results obtained at an advance ratio of 0.67. These distributions highlight the dependency of propeller secondary characteristics on the propeller blade orientation angle.

A significant variation in all the slipstream velocity components is observed for r/R varying from near the wall surface to the propeller tip. Therefore, in the current investigation, the propeller slipstream characteristics were averaged about the 12 intervals (every 30° of propeller rotation) in the 8th rotation. The corresponding averages are also highlighted in Figures 48 to 51.

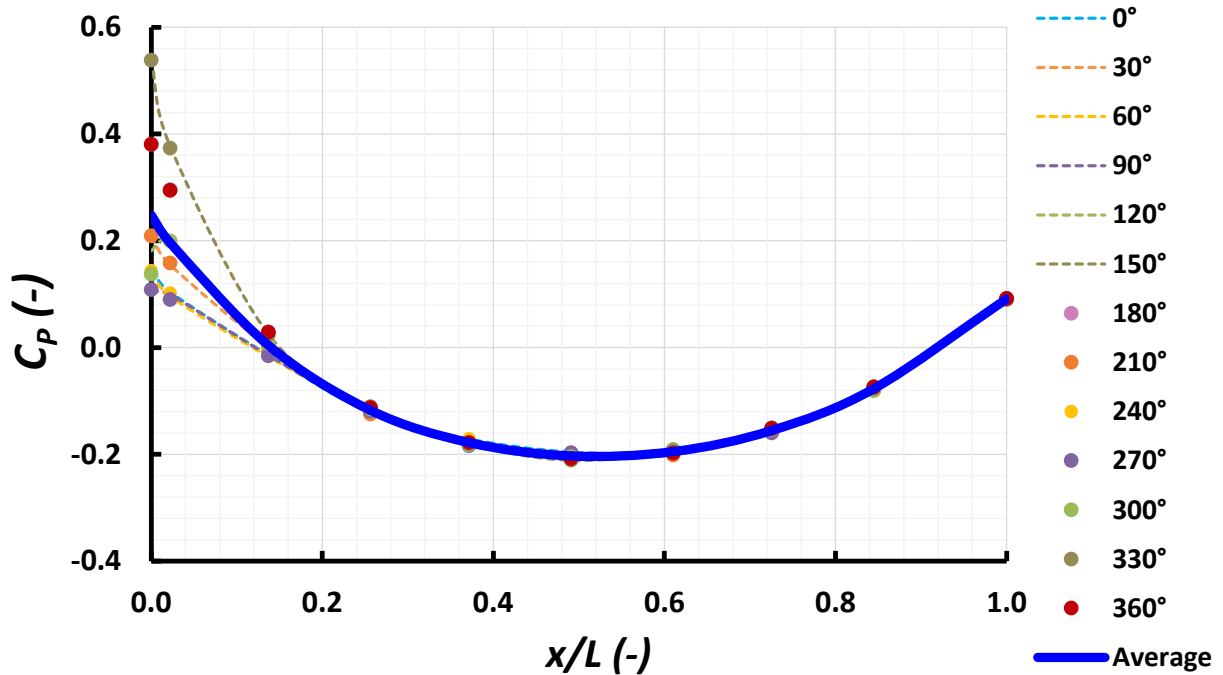


Figure 48. Variation of nacelle pressure during the 8th rotation at station NP_1.

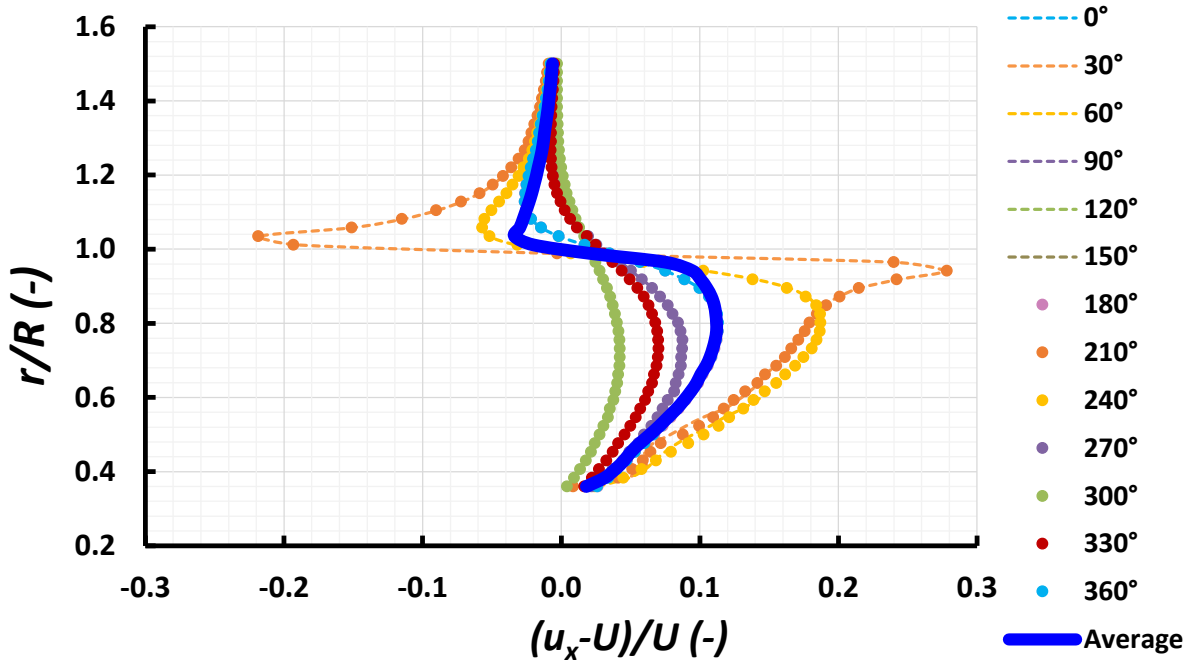


Figure 49. Variation of axial slipstream velocity during the 8th rotation at station SV_1a.

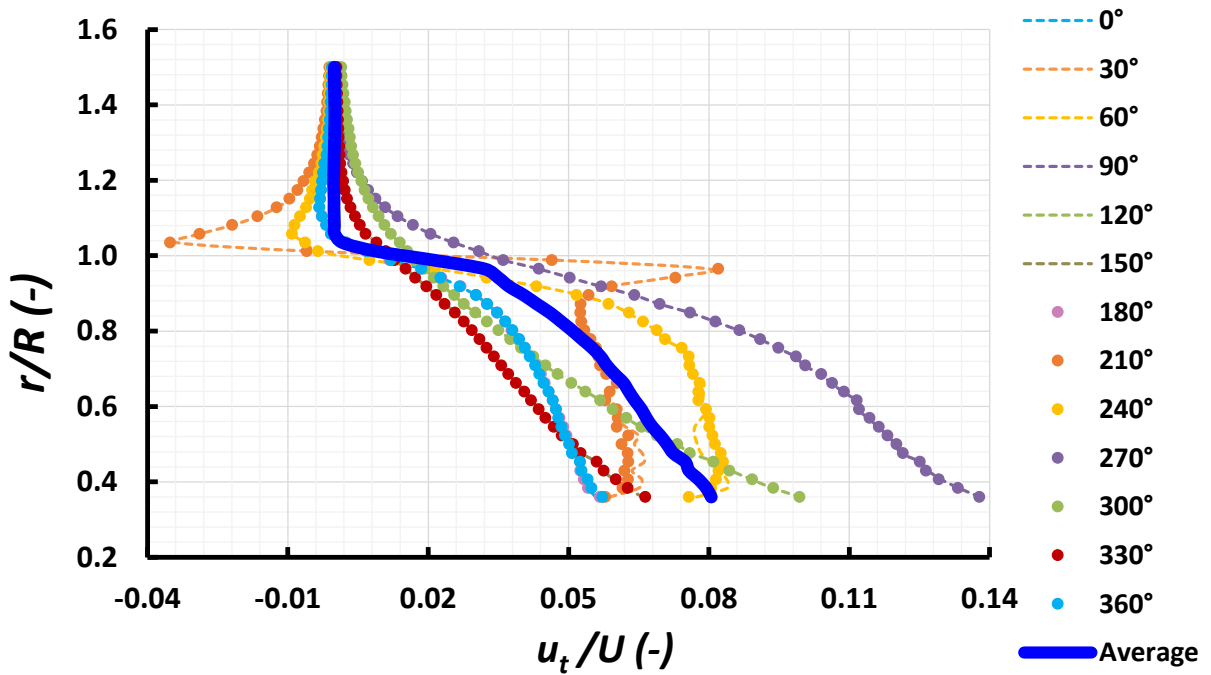


Figure 50. Variation of tangential slipstream velocity during the 8th rotation at station SV_1a.

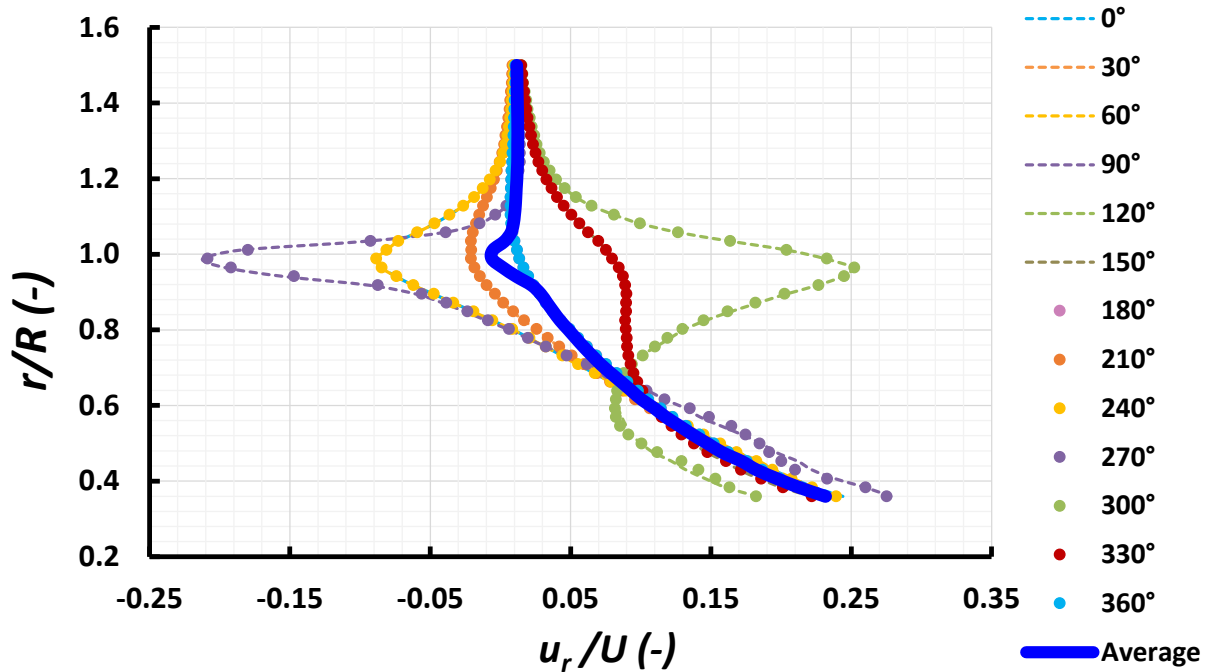


Figure 51. Variation of radial slipstream velocity during the 8th rotation at station SV_1a.

6.2.3.3 Flow Transition on the Propeller Blades

The implementation of intermittency transition model facilitates the capturing of both laminar and turbulent regions. The different flow regions on the propeller blade are visualized using the turbulent kinetic energy contour as shown in Figure 52. The range of turbulent kinetic energy quantity used for the contour is based on visualizations in Hansen's work [54]. In this contour, the blue region indicates laminar flow and red region indicates turbulent flow. A similar trend was observed on the second propeller blade.

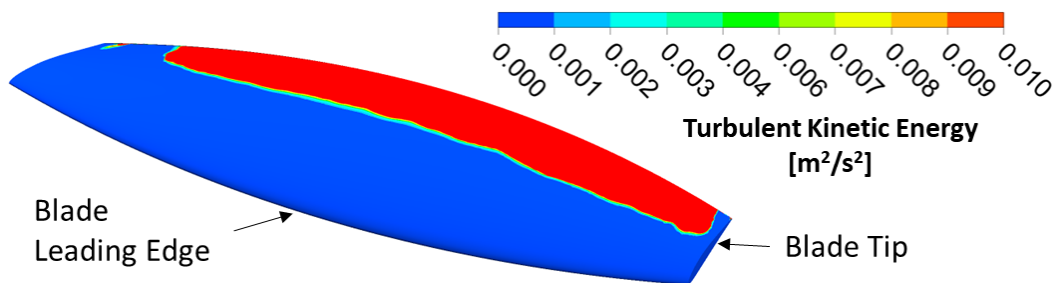


Figure 52. Different flow regions on the propeller blade – isometric view.

The flow regions on the upper (thrust) and lower (flat) surfaces of the propeller blade are shown in Figure 53.

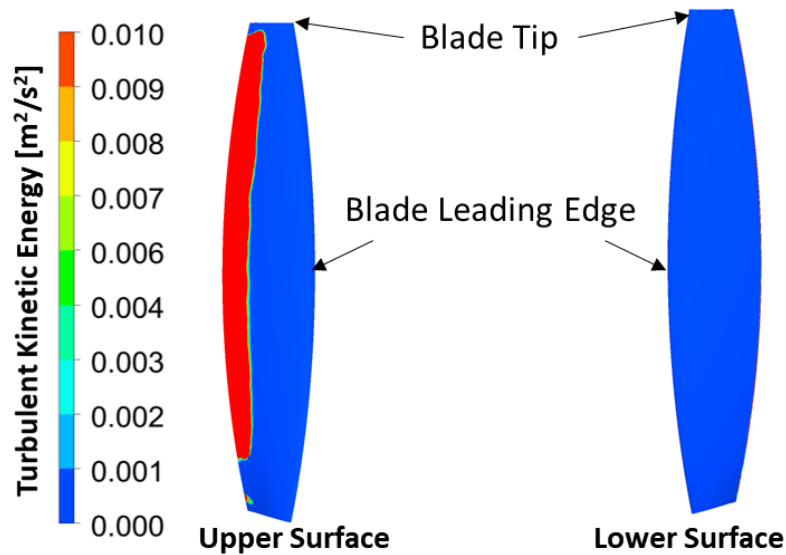


Figure 53. Different flow regions on the upper and lower surfaces of the propeller blade.

6.2.4 Comparison of Results

6.2.4.1 Propeller Primary Characteristics

The propeller thrust and power coefficients obtained using the medium mesh are compared with wind tunnel data in Figures 54 and 55. The propeller thrust and power coefficients were obtained using equations (8) and (9). In the current investigation, the advance ratio was varied by varying the freestream velocity for a constant propeller rotational speed.

The numerical thrust coefficient curve has a good qualitative and quantitative agreement with wind tunnel test data whereas the power coefficient curve has a good qualitative agreement. However, the numerical simulation tends to under predict power coefficient with respect to wind tunnel data.

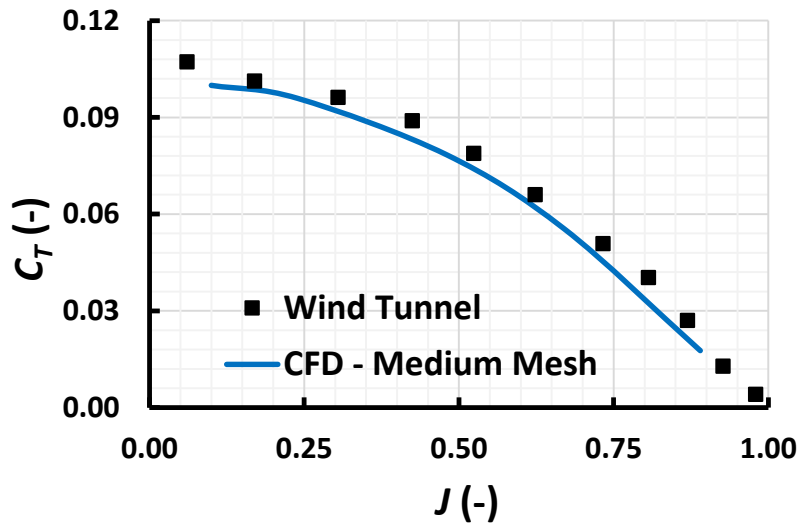


Figure 54. Variation of thrust coefficient with advance ratio.

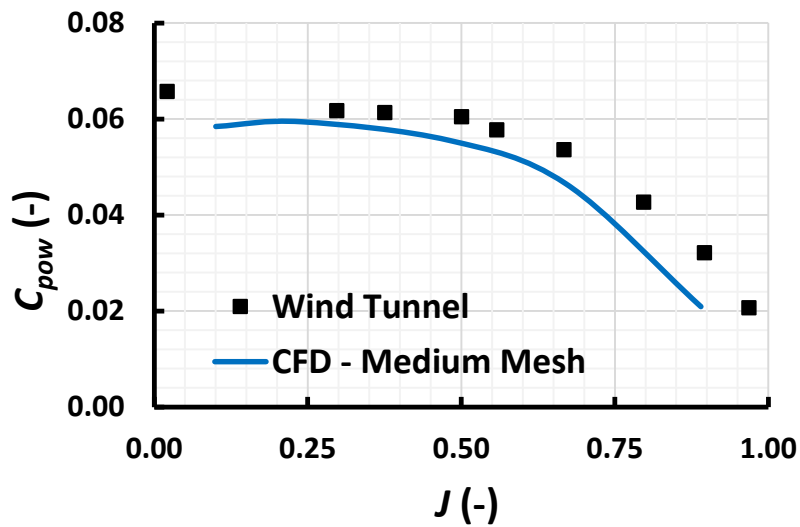


Figure 55. Variation of power coefficient with advance ratio.

The propeller thrust is primarily based on pressure difference about the blade faces, i.e., the pressure forces play a greater role than viscous forces in predicting thrust. However, the propeller power is dependent on both pressure and viscous forces and it is difficult to predict viscous contributions accurately using RANS methodology because of the inherent numerical dissipation effects associated with this methodology.

6.2.4.2 Propeller Secondary Characteristics

The wind tunnel data consists of two propeller secondary characteristics data: nacelle pressure distribution and slipstream velocities. First, the numerical pressure coefficients about the nacelle are compared with wind tunnel data. The reduction in static pressure caused by propeller rotation is shown in Figure 56.

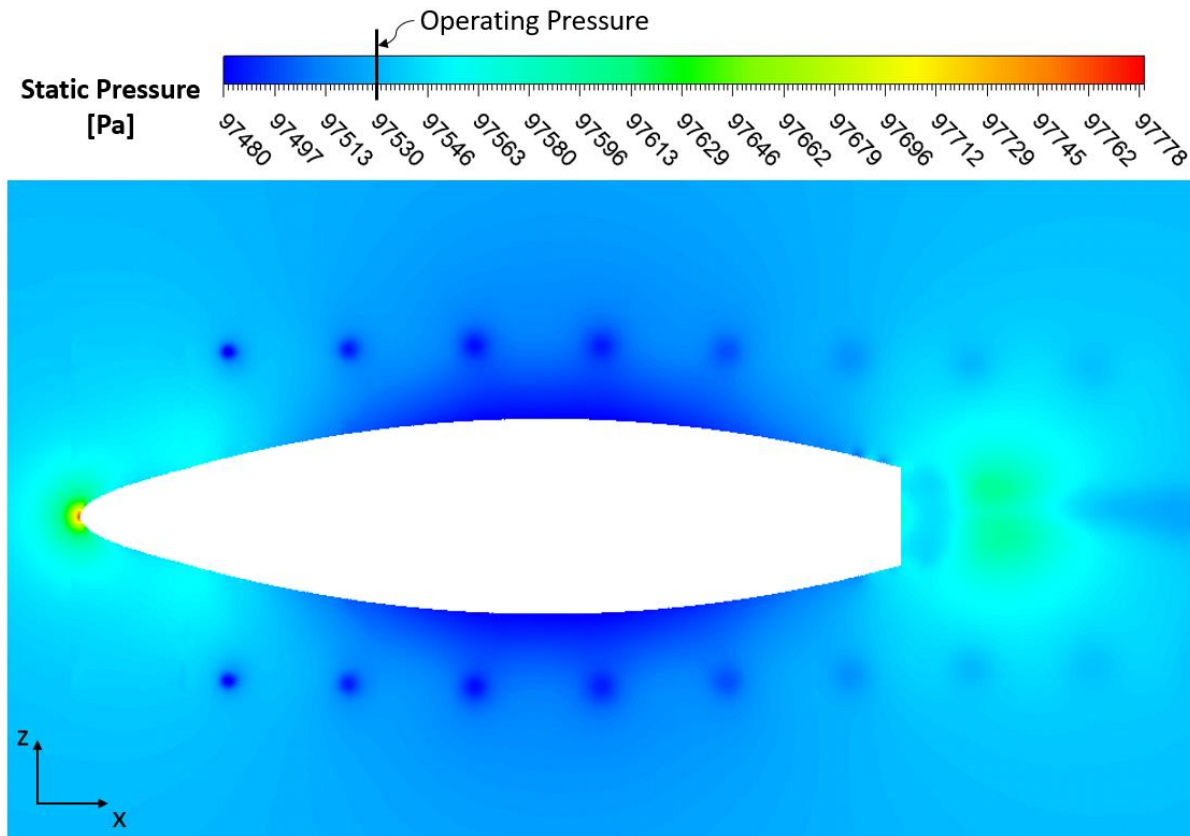


Figure 56. Static pressure contour on XZ plane at $y = 0$ m (for fine mesh at 0.08 seconds).

The static pressure reduces from the nacelle leading edge to the nacelle maximum diameter region (pressure suction region). Aft of the maximum diameter, the static pressure increases (pressure recovery region). The pressure coefficients are defined using equation (13). The reference pressure, density and velocity used for calculating pressure coefficients were 97,530 Pa, 1.146 kg/m³ and 20.422 m/s respectively.

The comparison of averaged nacelle pressure data with wind tunnel data is shown in Figures 57 to 60.

The fine mesh predicts a slightly higher pressure than the medium mesh for x/L greater than 0.85 at all the nacelle pressure measurement stations.

The CFD data has good correlation with the wind tunnel data. However, it is to be noted that accurate pressure distributions can be obtained using low-fidelity methods as well, which are relatively less computationally expensive. Therefore, the CFD nacelle pressure distributions are not discussed in detail.

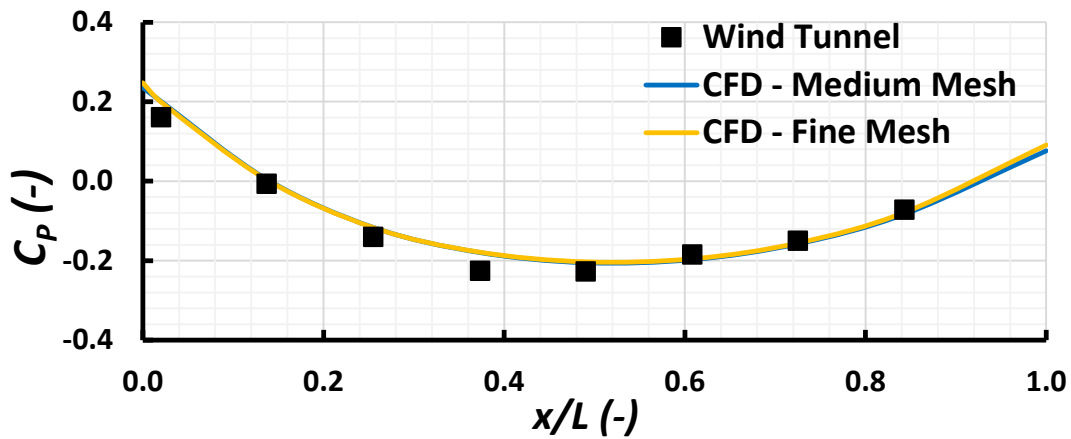


Figure 57. Nacelle pressure distribution at station NP_1.

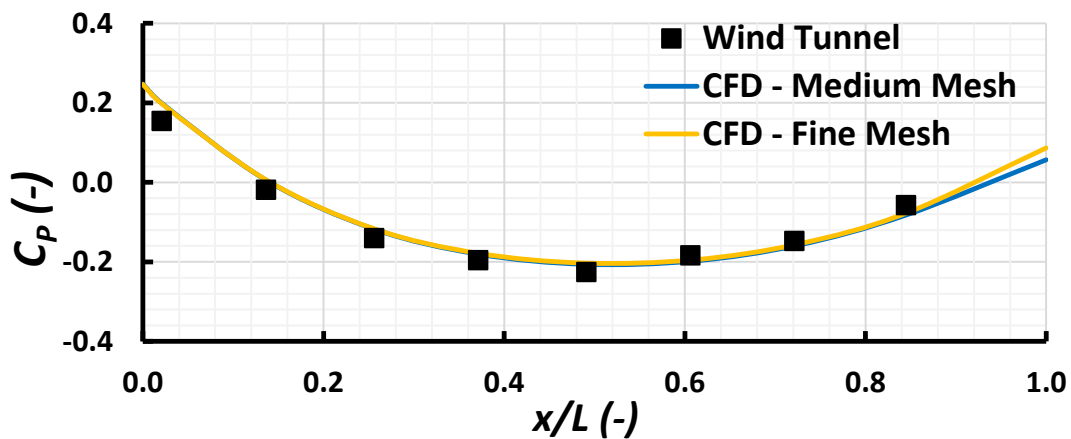


Figure 58. Nacelle pressure distribution at station NP_2.

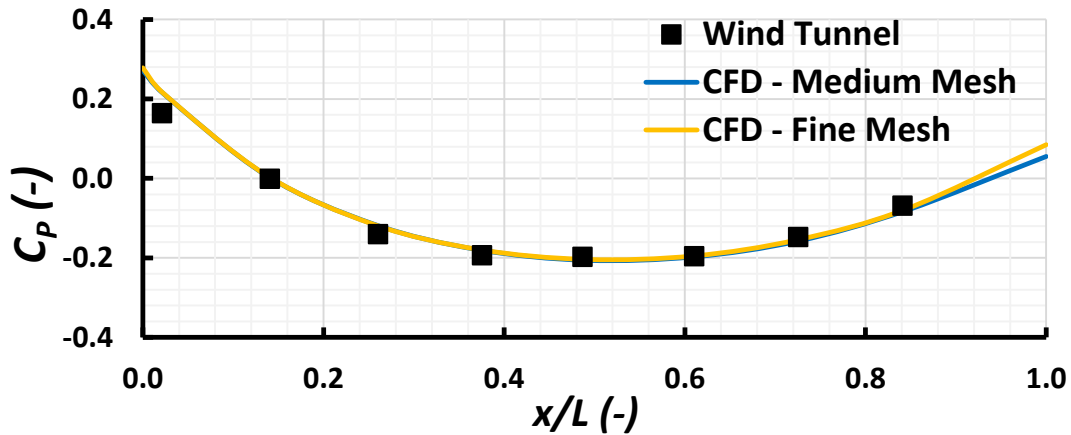


Figure 59. Nacelle pressure distribution at station NP_3.

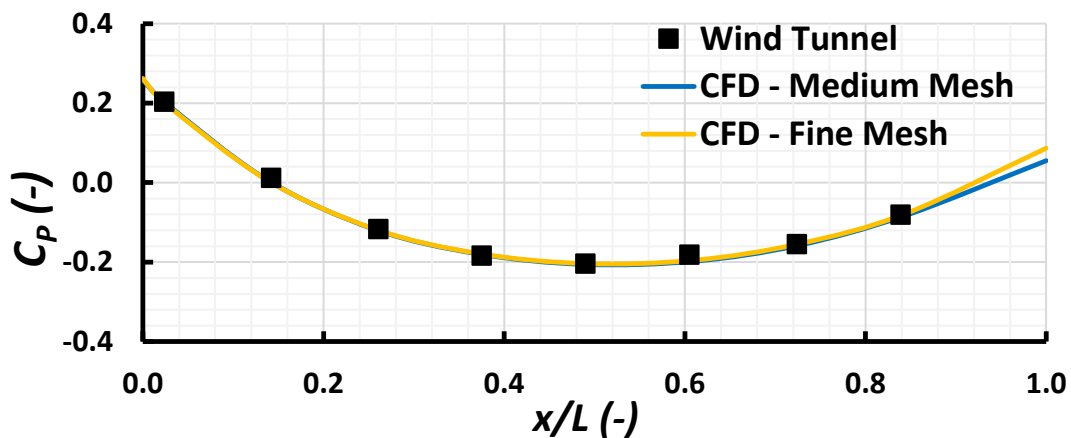


Figure 60. Nacelle pressure distribution at station NP_4.

In the current investigation, the vortex regions are represented using the “Q-criterion” method in ANSYS CFD-Post. The Q-criterion method identifies vortex regions when the second invariant of velocity gradient tensor is greater than zero [55]. In Figure 61, the propeller vortex regions correspond to fine mesh results obtained for an advance ratio of 0.67 at 0.08 seconds and a Q-criterion level of 3×10^{-5} . In general, the propeller vortical structures are very complex. In Figure 61, only the prominent blade tip vortex and blade trailing edge vortices near the propeller blades are shown.

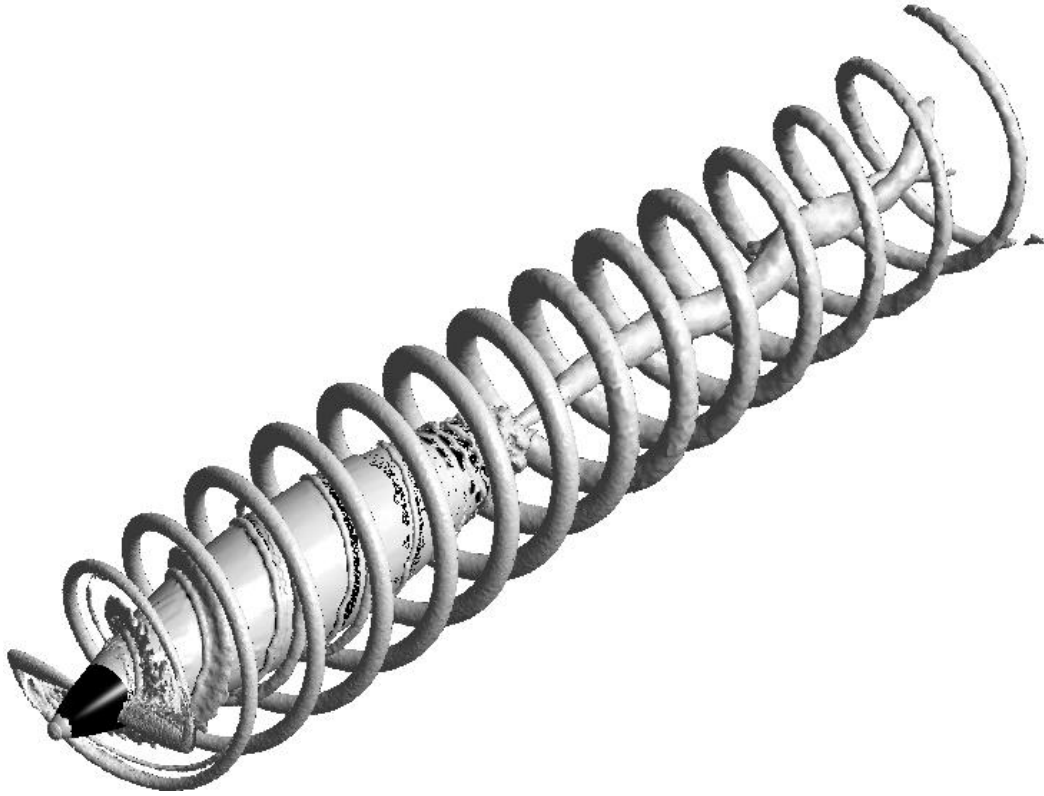


Figure 61. Propeller vorticity visualization.

As explained in Section 5.1, the vortex shedding from the propeller blades affect the downstream velocity distributions. For example, in Figure 62, the tangential velocity gradients due to propeller position and vortex are highlighted for an axial plane located at 0.014 m from the nacelle leading edge. Furthermore, the tangential velocity gradients on the axial plane due to propeller blade trailing edge and tip vortex is shown in detail in Figure 63. The axial velocity and radial velocity distributions are shown in Figures 64 and 65.

The propeller rotation generally increases the induced velocity in the slipstream region. Therefore, the slipstream might contract to maintain a constant mass flow rate in the propeller downstream region [56]. The slipstream contraction downstream of the nacelle can be observed in Figure 64.

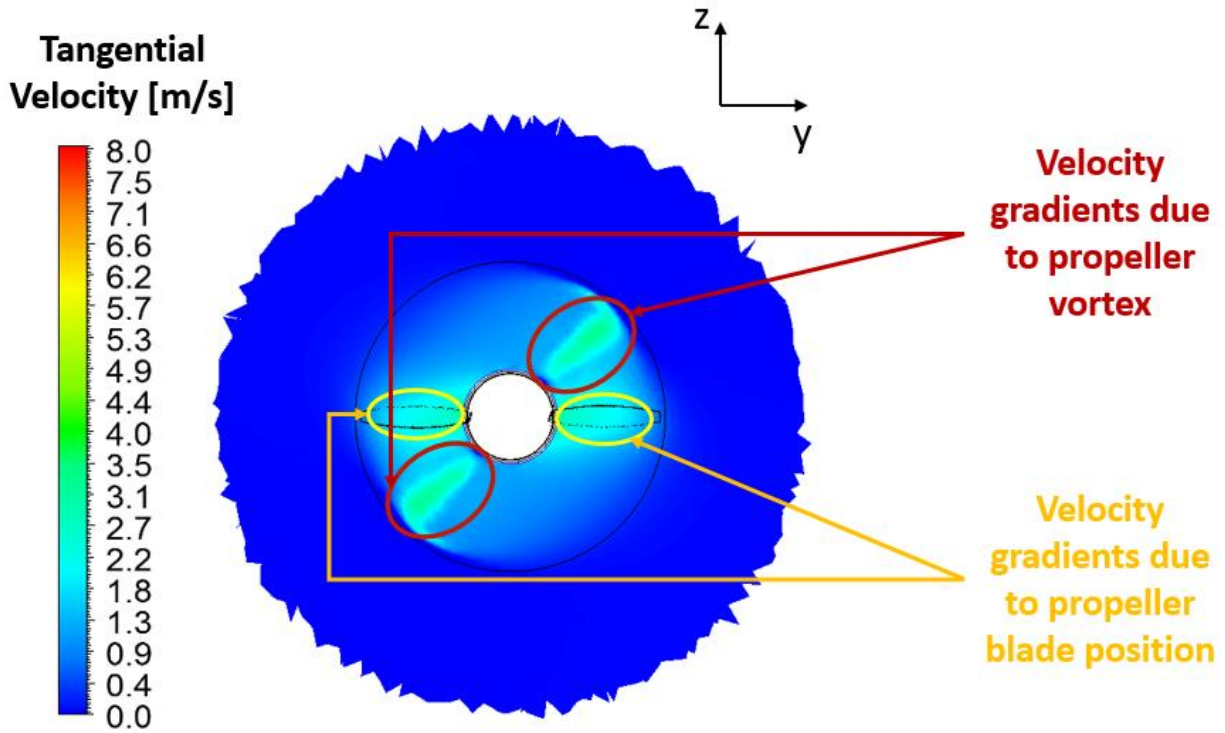


Figure 62. Tangential velocity contour on YZ plane at $x = 0.014$ m (for fine mesh at 0.08 seconds).

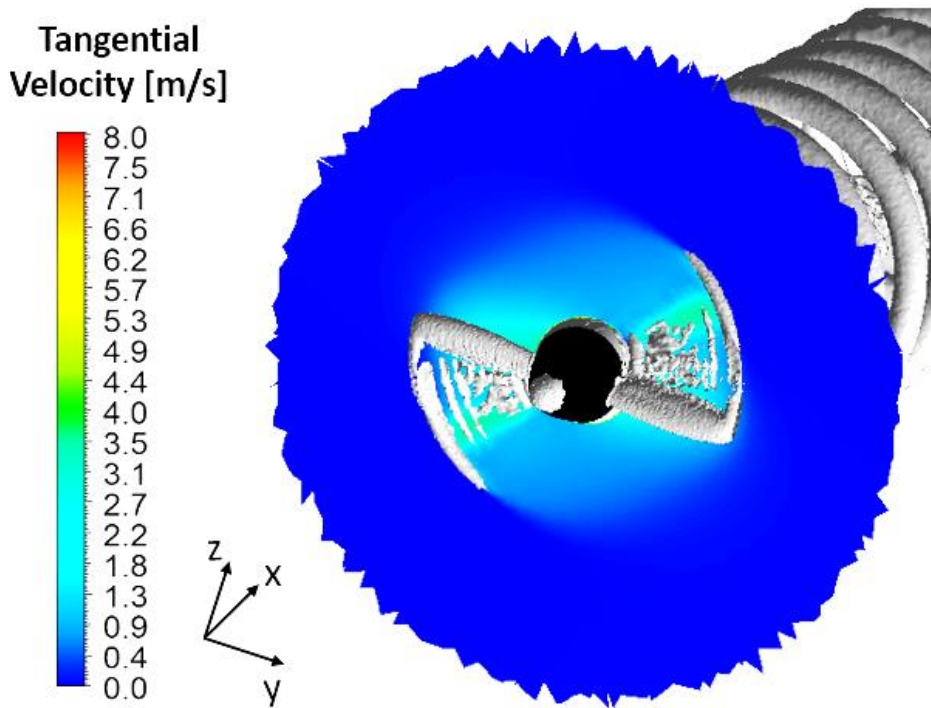


Figure 63. Schematic of tangential velocity gradients due to propeller vortex (for fine mesh at 0.08 seconds).

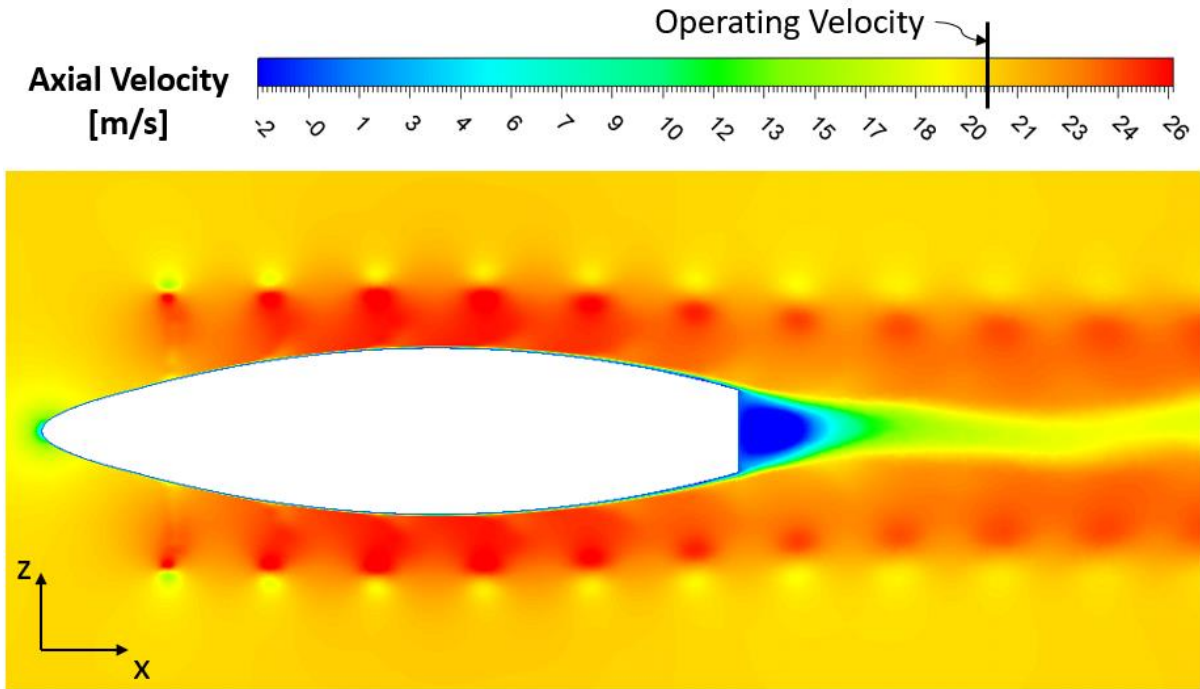


Figure 64. Axial velocity contour on XZ plane at $y = 0$ m (for fine mesh at 0.08 seconds).

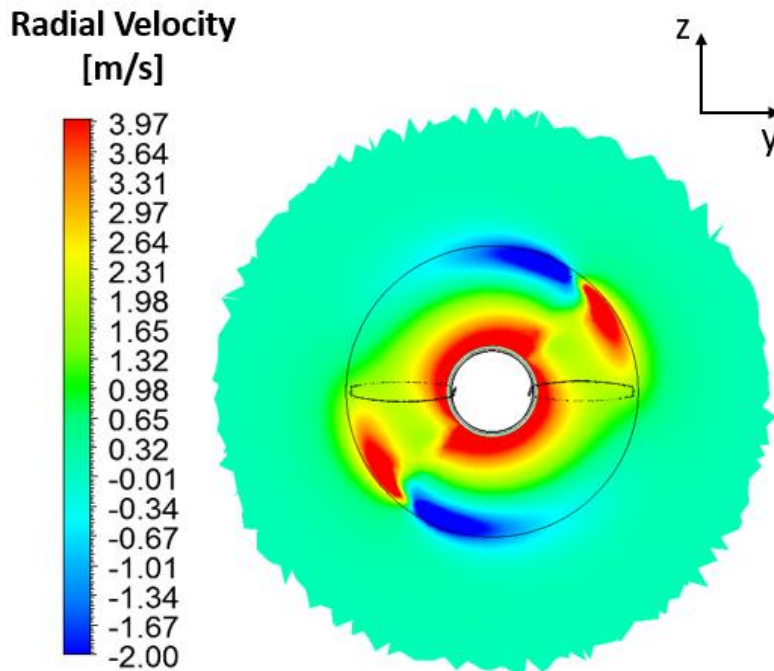


Figure 65. Radial velocity contour on YZ plane at $x = 0.014$ m (for fine mesh at 0.08 seconds).

The instantaneous velocity distributions shown in Figures 49 to 51, depicts the high sensitivity of velocity distributions to the propeller blade orientation angle which consequently dictates the propeller vortex orientation. Therefore, in the current investigation, a significant emphasis was placed on predicting the slipstream velocity radial distributions using CFD analysis. The wind tunnel data definitions for slipstream velocity component ratios as provided in Ghoudoussi's work [15] are given below:

$$\text{Axial velocity ratio} = \frac{u_x - U}{U} \quad (19)$$

$$\text{Tangential velocity ratio} = \frac{u_t}{U} \quad (20)$$

$$\text{Radial velocity ratio} = \frac{u_r}{U} \quad (21)$$

where

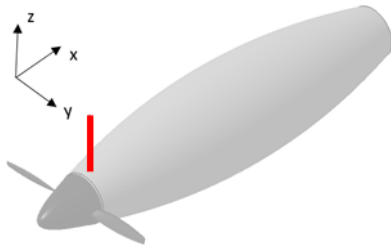
u_x Local axial velocity (m/s)

u_t Local tangential velocity (m/s)

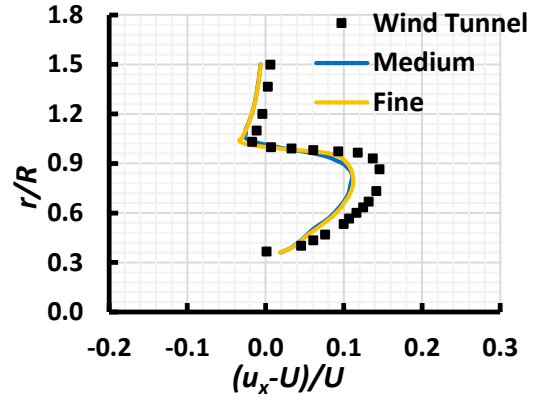
u_r Local radial velocity (m/s)

In the propeller slipstream region, the local axial velocities (u_x) are generally higher than the freestream velocity (U) i.e., u_x/U will be greater than 1. However, to maintain comparable velocity ratio ranges with tangential and radial velocity ratios, the axial velocity ratio is expressed in terms of difference between local axial velocity and freestream velocity.

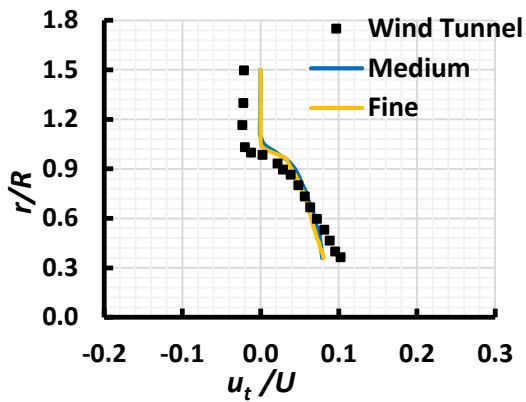
The slipstream velocities obtained using both the medium and fine mesh sizes are compared with the wind tunnel data as shown in Figures 66 to 74.



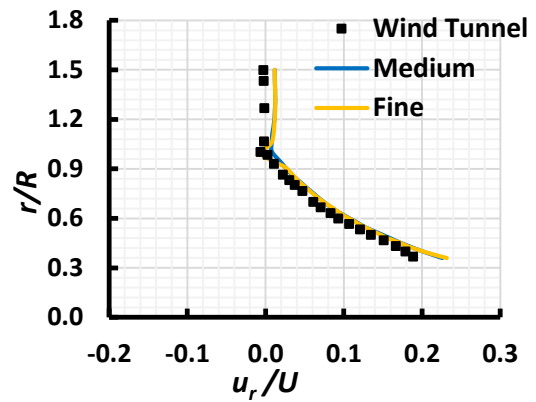
(a) Station location.



(b) Axial component.

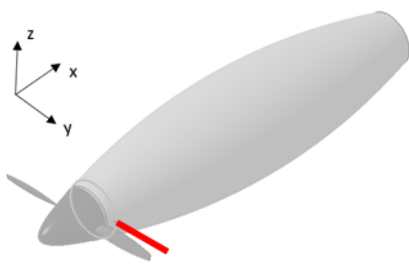


(c) Tangential component.

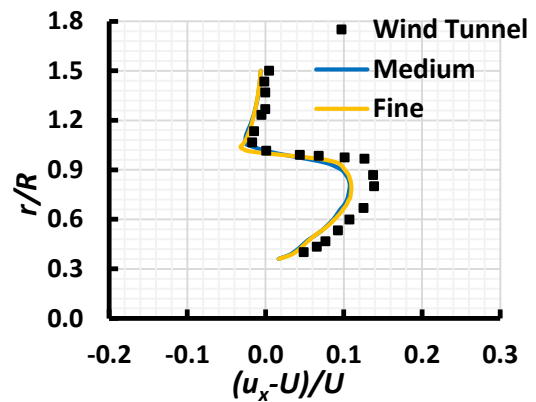


(d) Radial component.

Figure 66. Comparison of slipstream velocities at station SV_1a.

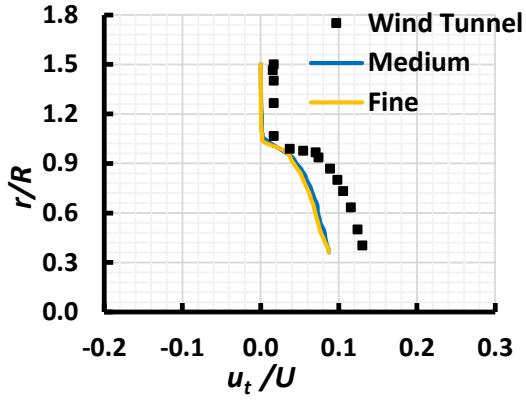


(a) Station location.

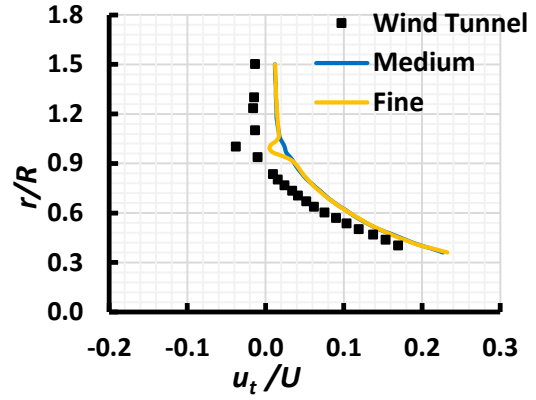


(b) Axial component.

Figure 67. Comparison of slipstream velocities at station SV_1b.

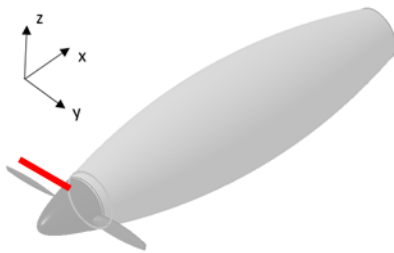


(c) Tangential component.

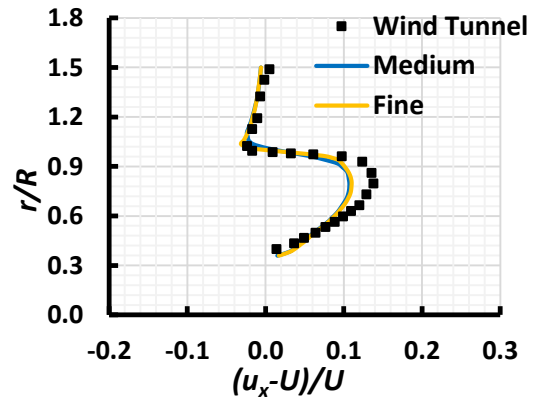


(d) Radial component.

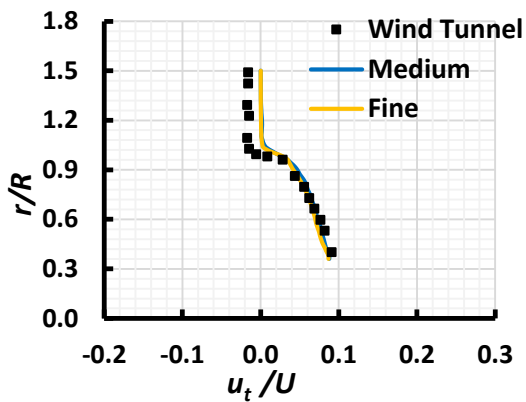
Figure 67 (continued)



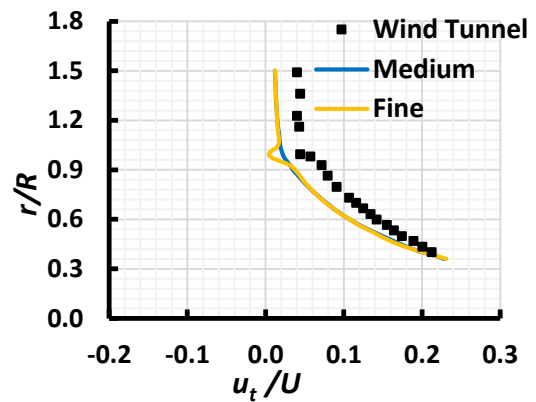
(a) Station location.



(b) Axial component.

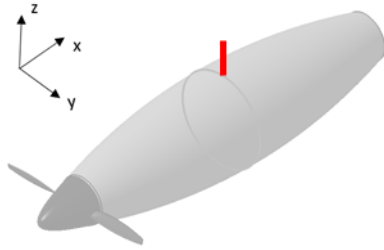


(c) Tangential component.

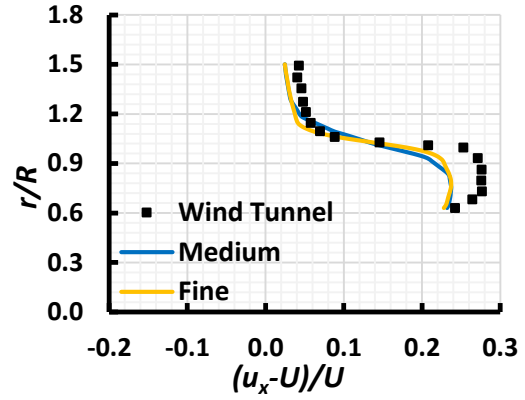


(d) Radial component.

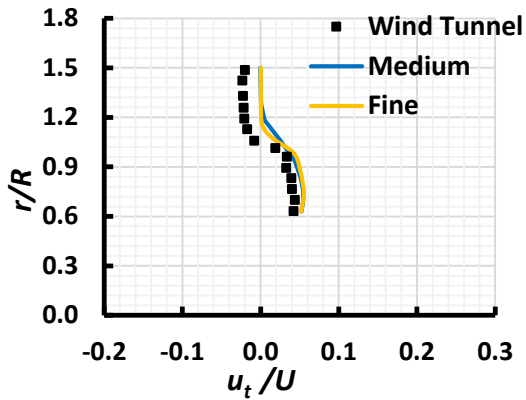
Figure 68. Comparison of slipstream velocities at station SV_1c.



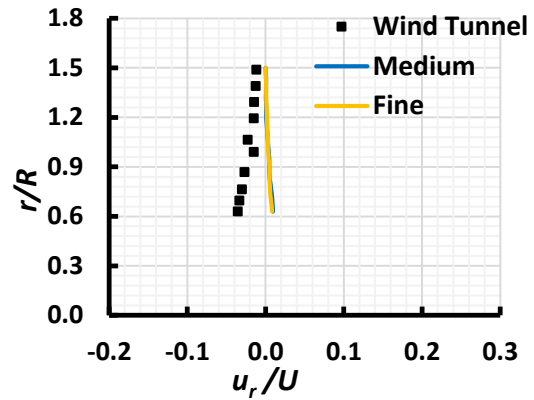
(a) Station location.



(b) Axial component.

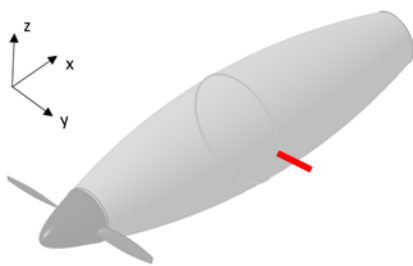


(c) Tangential component.

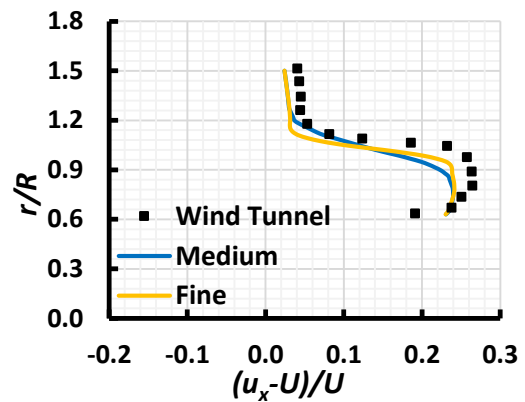


(d) Radial component.

Figure 69. Comparison of slipstream velocities at station SV_2a.

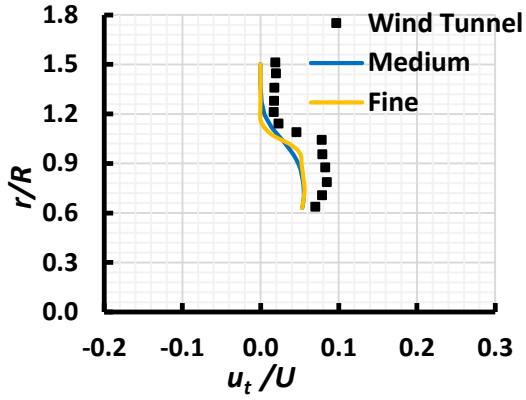


(a) Station location.

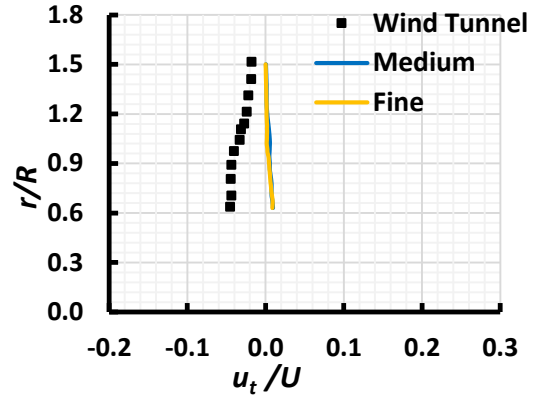


(b) Axial component.

Figure 70. Comparison of slipstream velocities at station SV_2b.

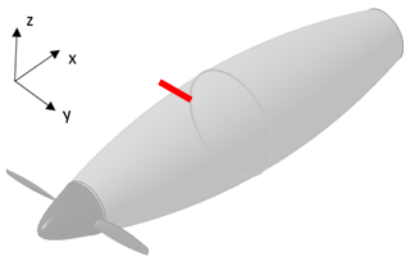


(c) Tangential component.

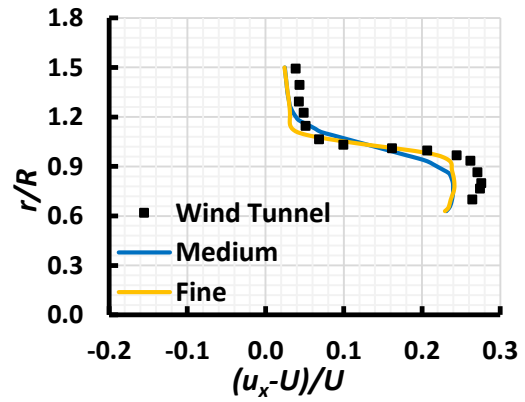


(d) Radial component.

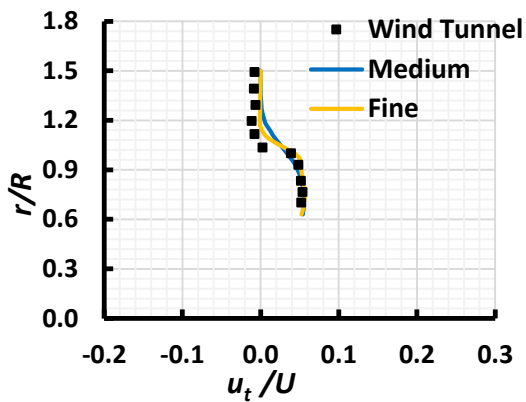
Figure 70 (continued)



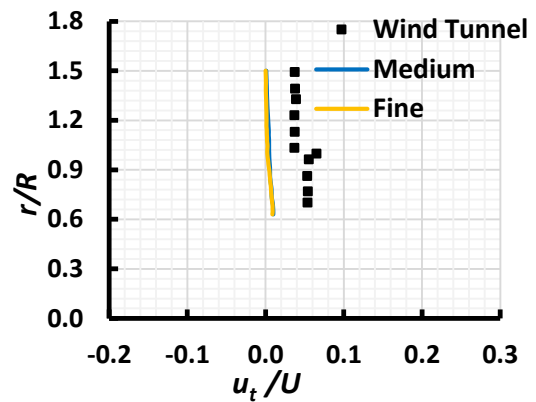
(a) Station location.



(b) Axial component.

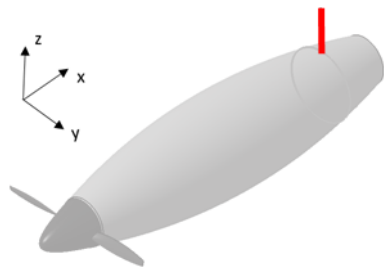


(c) Tangential component.

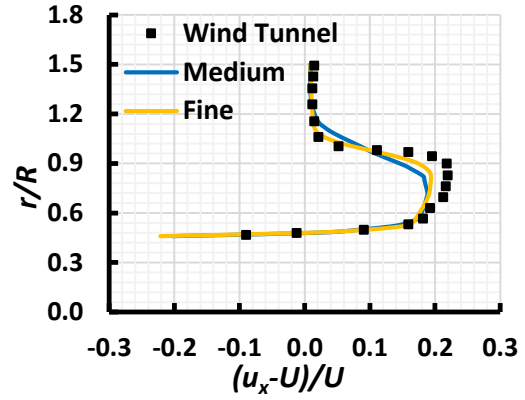


(d) Radial component.

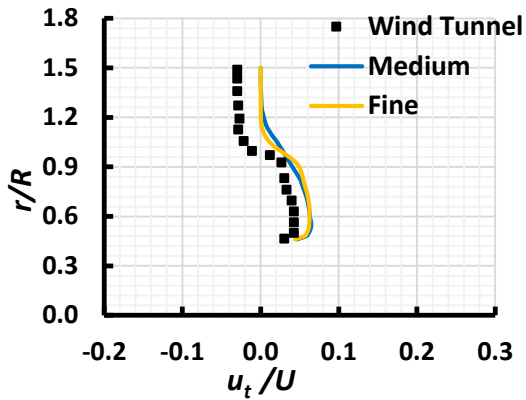
Figure 71. Comparison of slipstream velocities at station SV_2c.



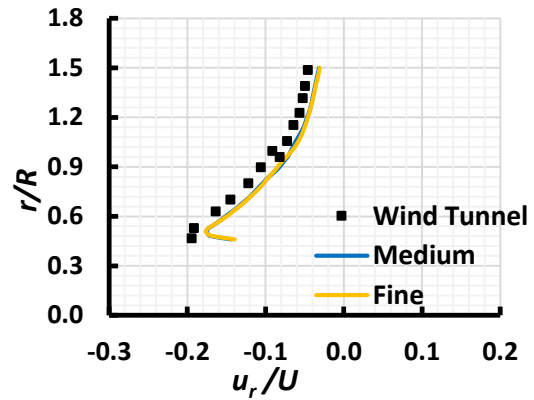
(a) Station location.



(b) Axial component.

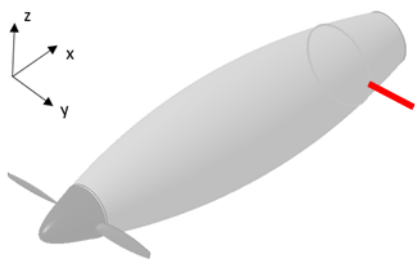


(c) Tangential component.

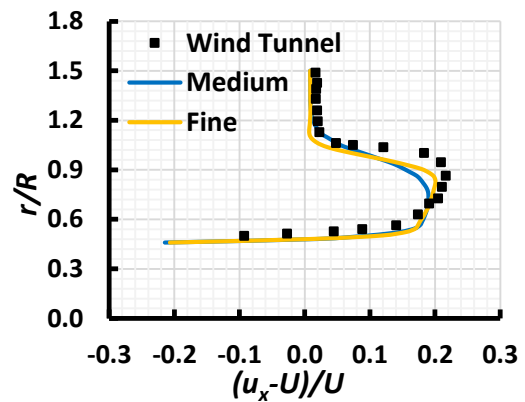


(d) Radial component.

Figure 72. Comparison of slipstream velocities at station SV_3a.

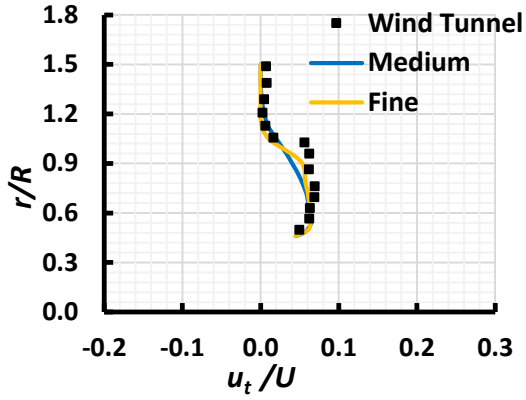


(a) Station location.

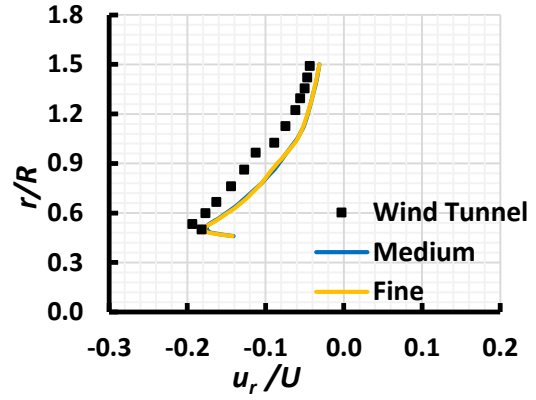


(b) Axial component.

Figure 73. Comparison of slipstream velocities at station SV_3b.

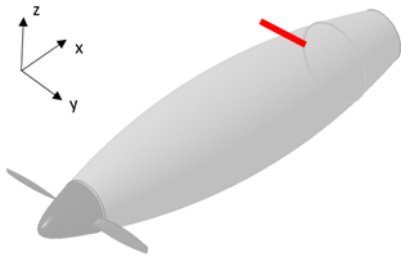


(c) Tangential component.

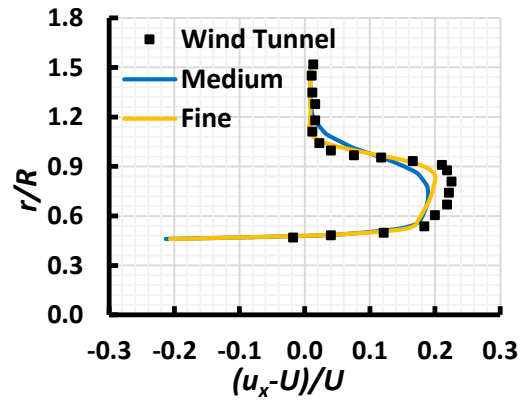


(d) Radial component.

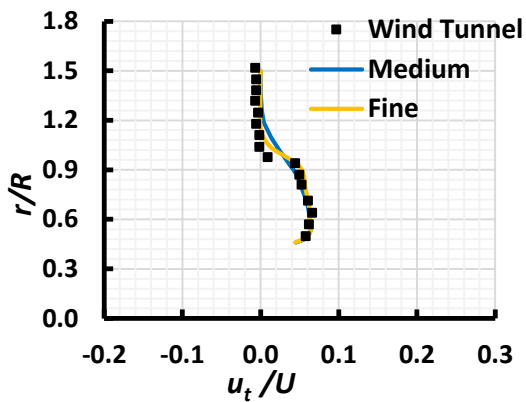
Figure 73 (continued)



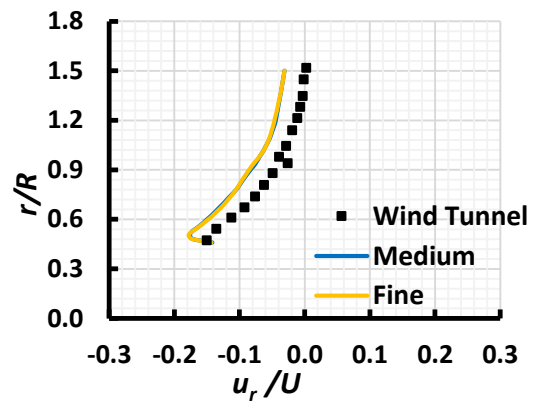
(a) Station location.



(b) Axial component.



(c) Tangential component.



(d) Radial component.

Figure 74. Comparison of slipstream velocities at station SV_3c.

The wind tunnel tests were conducted at an angle of attack of 0° . At zero angle of attack, the forces and moments generated about each propeller blade should be identical. As the current numerical model represents an axisymmetric geometry, it is assumed that the flow field downstream of the propeller blades may be symmetric i.e., the averaged flow field measurements at varying azimuthal angle needs to be similar at a given nacelle axial cross section. In the current investigation, in addition to comparing the numerical slipstream velocity distributions with wind tunnel data, the flow symmetry is discussed for both the numerical and wind tunnel data in terms of axial velocity distributions.

The conclusions that follow are based on the comparison of numerical results with wind tunnel data, as shown previously in Figures 66 to 74. The fine mesh tends to have a better qualitative and quantitative agreement with wind tunnel data due to the relatively larger grid resolution in the propeller wake region compared to the medium mesh.

The numerical simulations are able to capture the variation in axial velocity components along the nacelle length depicted by wind tunnel data i.e., increase in axial velocity from $x/L = 0.02$ to $x/L = 0.49$ and reduced values from $x/L = 0.49$ to $x/L=0.84$. Similar to wind tunnel data, the numerical maximum axial velocities occur at $x/L = 0.49$. At all the measurement stations, the numerical simulations under predict the peak magnitude of axial velocity. Furthermore, the difference between the peak magnitude of axial velocity predicted by numerical simulations and wind tunnel reduces with increase in axial distance of measurement station from the propeller blades. This could be attributed to the strength of the propeller vortices which generally dissipates as it travels downstream from the nacelle leading edge ($x/L = 0$) to nacelle trailing edge ($x/L = 1$). It is difficult to accurately capture the complicated propeller vortical structures using RANS

approach due to its associated limitations of turbulence models and numerical dissipation. The largest discrepancy in peak magnitude of axial velocity is observed at $x/L = 0.02$ where the propeller vortex strength is significantly larger when compared to the $x/L = 0.49$ and $x/L = 0.84$ locations. In addition, the numerical simulations under predict the axial velocities for r/R greater than 1 at $x/L = 0.49$. As of now, the reason of this discrepancy is not clear. It is also observed that the axial velocity obtained from fine mesh has improved correlation with wind tunnel data for increasing downstream axial distance from the propeller blade. The wind tunnel and numerical data have identical axial velocity distributions for varying azimuth angle (0° , 90° , and 180°) at each nacelle longitudinal cross section station showcasing flow symmetry characteristics.

In terms of tangential velocity, the numerical results have a reasonable qualitative agreement with wind tunnel data for all slipstream measurement stations. The numerical results have identical tangential velocity distributions for varying azimuth angle (0° , 90° , and 180°) at each x/L station. Unlike the axial velocity distribution, a clear trend cannot be established for the tangential velocity distributions. A slight difference exists for tangential velocity distributions at different azimuth angles from wind tunnel tests. For example, at $x/L = 0.02$ and 0.49 , the wind tunnel tangential velocities at an azimuth angle of 90° differs from measurements at azimuth angles of 0° and 270° . In addition, the wind tunnel tangential velocities for r/R greater than 1 have an irregular pattern for at least one of the azimuth angles at each x/L station, whereas in the numerical simulations, at all measurement stations, the tangential velocities tend to zero for r/R greater than 1. Due to these differences between numerical and test data patterns, consistent quantitative comparisons cannot be made for tangential velocity distributions.

In terms of radial velocity, the numerical results have a reasonable qualitative agreement with wind tunnel data for all the measurement stations except for stations at $x/L=0.49$. The order of magnitude of the radial velocities at the aforementioned station is significantly lower when compared to the radial velocity distributions at the rest of the measurement stations. It is challenging to capture these lower magnitude radial velocities accurately in both wind tunnel tests and numerical analysis. Due to the very low magnitude of tangential and radial velocities, it could be possible that the numerical dissipation inaccuracies of turbulence models itself may exceed the magnitude of these numerically estimated velocity components. The wind tunnel radial velocity distributions have an irregular pattern and/or unsymmetrical distribution for at least one azimuth angle at each x/L station. Therefore, similar to slipstream tangential velocities, consistent quantitative deductions cannot be made for slipstream radial velocity components as well.

A few uncertainties associated with the wind tunnel results include the unavailability of slipstream velocity data averaging procedure and repeatability results of the wake survey tests for COMP propeller. Based on the currently available wind tunnel and numerical results, it is not possible to produce reasonable quantitative deductions for tangential and radial slipstream velocity components. In order to achieve the aforementioned objective, further detailed wind tunnel and/or numerical investigations need to be conducted.

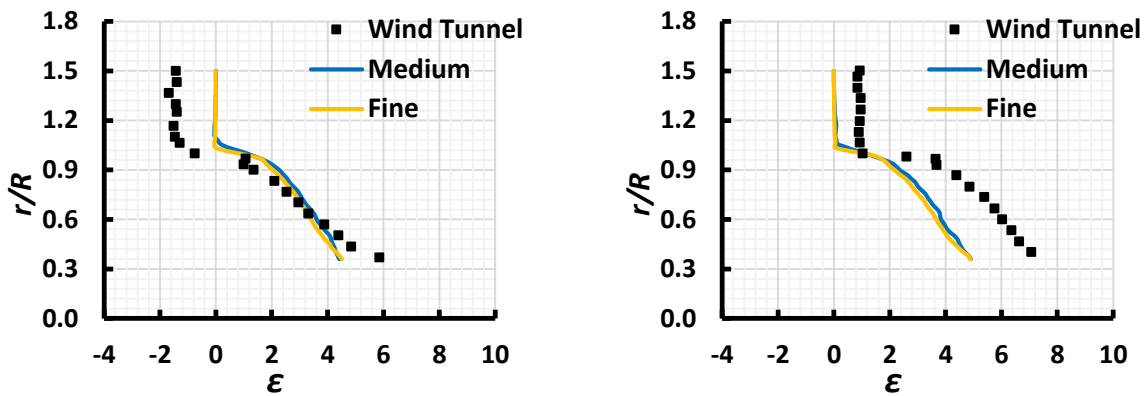
In general, among the 3 components of the slipstream velocity, the slipstream axial component plays a major role on the aerodynamics of downstream surfaces. As of now, insightful deductions have been accomplished for the axial velocity components and qualitative comparisons are available for tangential and radial slipstream components.

Therefore, further investigations are not conducted to obtain detailed performance/validity of RANS approach to predict accurate tangential and radial slipstream components.

In addition to slipstream velocities, the wind tunnel data also consists of swirl angle distribution data. The swirl angle (ε) definition is provided in equation (22).

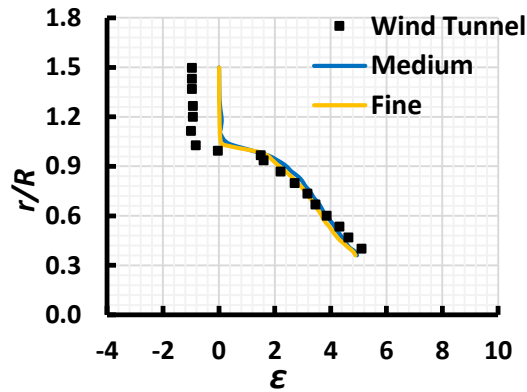
$$\varepsilon = \tan^{-1} \left(\frac{u_t}{u_x} \right) \quad (22)$$

The swirl angle results are compared with wind tunnel data in Figures 75 to 77.



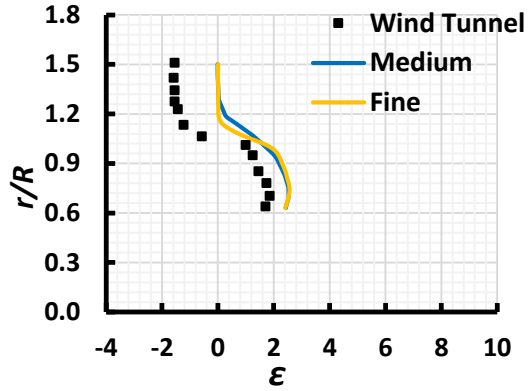
(a) Station SV_1a.

(b) Station SV_1b.

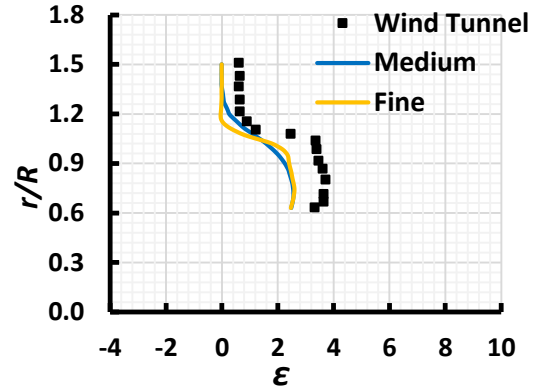


(c) Station SV_1c.

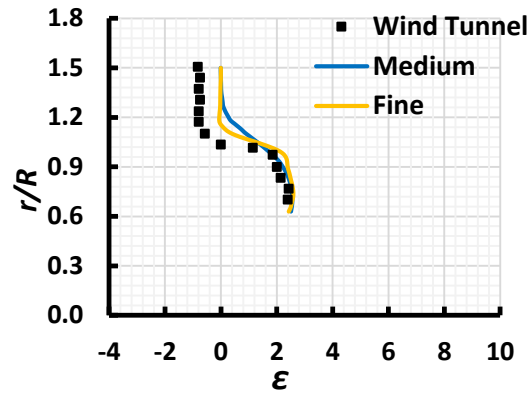
Figure 75. Swirl angles at $x/L = 0.02$.



(a) Station SV_2a.

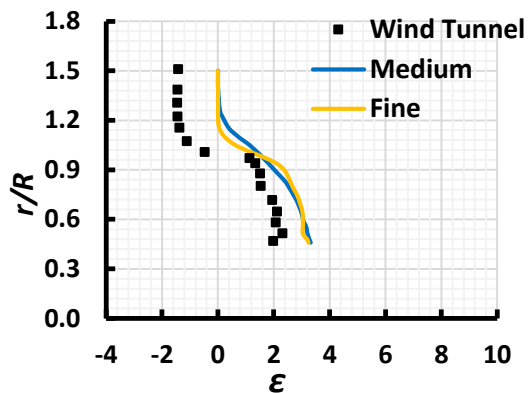


(b) Station SV_2b.

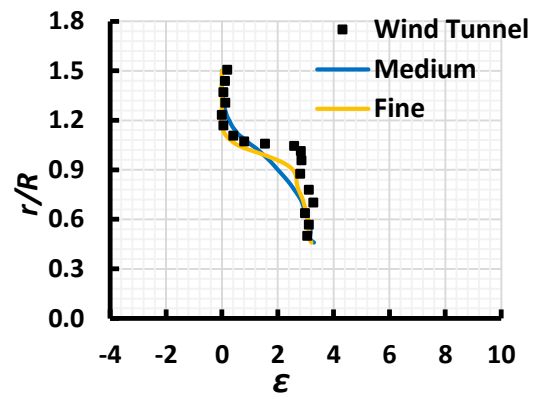


(c) Station SV_2c.

Figure 76. Swirl angles at $x/L = 0.49$.

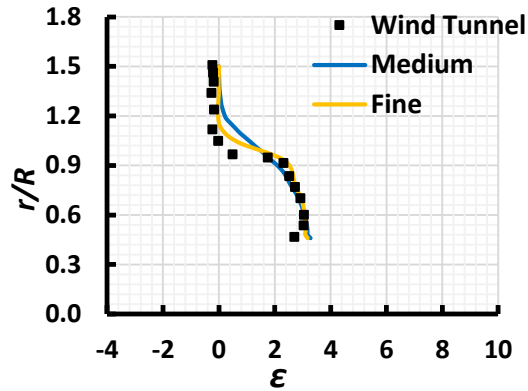


(a) Station SV_3a.



(b) Station SV_3b.

Figure 77. Swirl angles at $x/L = 0.84$.



(c) Station SV_3c.

Figure 77 (continued)

As the swirl angle is derived from axial and tangential velocity components, it serves as an auxiliary parameter to denote the slipstream characteristics. The deductions made for comparison of numerical axial and tangential slipstream components with wind tunnel data are applicable for the swirl angle as well. Therefore, for brevity, detailed discussion about comparisons of swirl angle with the wind tunnel are not included. The difference in wind tunnel swirl angle distributions for each x/L station highlights the slight discrepancies present in the wake survey measurements.

CHAPTER 7

CONCLUSIONS AND FUTURE WORK

The propeller wind tunnel data are available for low Reynolds numbers regime. In this flow regime, the flow may transition from laminar to turbulent flow. Therefore, initial time-accurate two-dimensional CFD simulations have been performed, on Eppler 387 airfoil, to assess the ANSYS Fluent transition modeling capabilities. In addition to implementation of high-fidelity method (CFD), the Eppler 387 airfoil aerodynamic characteristics were also estimated using a low-fidelity method (XFOIL). At low Reynolds, the LSB generally occurs at moderate angles of attack and a significant variation in airfoil drag is present when compared to the lift and pitching moment. Therefore, the different numerical methods were evaluated by comparing its associated airfoil drag with wind tunnel data.

The two-dimensional CFD simulations consisted of predicting the airfoil aerodynamic characteristics using three different viscous models: laminar, intermittency and $k-\omega$ SST with low Reynolds number corrections. A detailed grid independence and time-step independence studies were carried out.

Based on comparison with wind tunnel data, the airfoil study indicates that XFOIL, and CFD simulations based on coarse mesh and a large time-step size, can be used for such low Reynolds number airfoils in the conceptual design stages to rapidly obtain basic aerodynamic characteristics.

Based on the comparison of CFD results with wind tunnel and XFOIL data, the intermittency model is able to capture the aerodynamic flow fields of the airfoil better when

compared to the other two viscous models at low to moderate angles of attack. However, the intermittency model over predicted the drag data at high angles of attack.

The propeller wind tunnel model geometry was recreated to build a numerical model for CFD simulations. The intermittency viscous model was used for predicting the COMP propeller primary and secondary aerodynamic characteristics. The time-accurate sliding mesh methodology has successfully been implemented to model the propeller rotation in ANSYS Fluent. A detailed grid independence study was conducted to check the effect of grid resolution on propeller primary and secondary characteristics.

The predicted thrust coefficient curve is in good agreement with wind tunnel data. However, the CFD analysis under predicted the power coefficient values which may be attributed to the intermittency model implementation. The nacelle pressure distributions obtained using medium and fine meshes have a good correlation with the wind tunnel data. The effect of propeller blade orientation and propeller vortex on the slipstream velocities were highlighted. The slipstream velocity distributions obtained with medium and fine meshes were compared with the wind tunnel data. The predicted axial velocity components have a good qualitative correlation with wind tunnel data. However, the CFD simulations under predicted for the peak magnitude of axial velocities at almost every nacelle cross section. This discrepancy maybe due to the limitations of the RANS modeling approach to accurately capture vortex structures. Furthermore, the tangential and radial velocities also have a reasonable qualitative agreement with the wind tunnel data.

The propeller grid independence study indicates that CFD analysis with a coarse mesh could be conducted to obtain basic details of propeller primary aerodynamic

characteristics and slipstream velocity distributions with reasonable accuracy in the conceptual design phase. Furthermore, the accuracy of the slipstream velocity distributions is dependent on the mesh resolution. Therefore, the high grid resolution CFD analysis should be conducted in the detailed design phase.

Based on the results of the current investigations, the following topics could be investigated to obtain better numerical results for low Reynolds number airfoils and propellers:

- In the airfoil analysis, the variation in airfoil lift and drag with change in transition input variables (intermittency and viscosity ratio in boundary conditions) were checked only for an angle of attack of 4° . However, the transition model over predicted the drag data at high angles of attack. Therefore, a similar effort could be conducted to check the sensitivity of the transition model to these variables at high angles of attack.
- Conduct a detailed assessment of the numerical results for the laminar separation bubble such as the transition point and bubble length, and compare with experimental data. This could provide insightful information to understand the high drag values obtained using the transition model (check the extent of laminar and turbulent regions).
- Check the variation in propeller primary and secondary characteristics with a different rotational domain shape (cylinder was used in the current investigation).
- Check the effect of number of propeller rotations, number of inner iterations, and time-step size on propeller primary and secondary characteristics.

In terms of wind tunnel data, the information about repeatability of propeller secondary characteristics measurements could provide insightful information on the tolerances of wind tunnel data. Consequently, based on the repeatability information, a better judgement can be made to identify the acceptable percentage difference between numerical and wind tunnel data for slipstream velocity distributions. In addition to repeatability, if the procedure on averaging secondary characteristics in the wind tunnel tests are made available, the same procedure could be implemented for numerical simulation data. This practice would reduce data handling uncertainties when the numerical simulation data are being compared with wind tunnel data.

REFERENCES

REFERENCES

- [1] Bousquet, J.-M. and Gardarein, P., "Recent improvements in Propeller Aerodynamic computations," AIAA 18th Applied Aerodynamic Conference, Denver, CO, August 14-17, 2000.
- [2] Sforza, P. M., *Theory of Aerospace Propulsion*, 2nd Edition, Butterworth-Heinemann, 2016.
- [3] Bouquet, T., "Modelling the Propeller Slipstream Effect on the Longitudinal Stability and Control." Master Thesis, Delft University of Technology, 2016.
- [4] Chandra, Y., "Investigation of the Aerodynamic Performance of a DG808s UAS in Propeller Slipstream using Computational Fluid Dynamics," Master Thesis, University of Kansas, 2017.
- [5] Allen, H. J., "Estimation of the Forces and Moments Acting on Inclined Bodies of Revolution of High Fineness Ratio," NACA RM A9126, 1949.
- [6] Jorgensen. H., "Prediction of Static Aerodynamic Characteristics for Slender Bodies Alone and with Lifting Surfaces," NASA TR R-474, 1977.
- [7] Anderson, D. J., *Fundamentals of Aerodynamics*, 6th edition, McGraw-Hill Education, 2017.
- [8] Gur, O., and Rosen, A., "Comparison Between Blade-Element Models of Propellers," *The Aeronautical Journal*, Vol. 112, No. 1138, pp. 689-704, 2008.
- [9] Cho, J., and Williams., "Propeller-Wing Interaction Using a Frequency Domain Panel Method," *Journal of Aircraft*, Vol. 27, No. 3, pp. 196-203, 1990.
- [10] Thom, A. and Duraisamy, A., "Computational Investigation of Unsteadiness in Propeller Wake-Wing Interactions," *Journal of Aircraft*, Vol. 50, No. 3, pp. 985-988, 2013.
- [11] Veldhuis, L. L. M., "Review of Propeller-Wing Aerodynamic Interference," 24th *International Congress of the Aeronautical Sciences*, 2004.
- [12] Carroll, J. R., "Time-averaged Surrogate Modeling for Small Scale Propellers based on High-fidelity CFD Simulations," Ph.D. Dissertation, Mississippi State University, 2013.
- [13] Ferraro, G., Kipouros, T., Savill, M. A., Rampurwala, A., and Agostinelli, C., "Propeller-Wing Interaction Prediction for Early Design," 52nd Aerospace Science Meeting, AIAA SciTech Forum, Maryland, 2014.

REFERENCES (continued)

- [14] Lötstedt, P., "Accuracy of a Propeller Model in Inviscid Flow," *Journal of Aircraft*, Vol. 32, No. 6, 1995.
- [15] Ghoddoussi, A., "A More Comprehensive Database for Propeller Performance Validations at Low Reynolds Number," Ph.D. Dissertation, Wichita State University, 2016.
- [16] Gudmundsson, S., *General Aviation Aircraft Design – Applied Methods and Procedures*, 1st Edition, Butterworth-Heinemann, 2014.
- [17] Aerodynamics of Flight, Helicopter Flying Handbook, U.S. Department of Transportation, Federal Aviation Administration, FAA-H-8083-21A, 2012.
- [18] Phillips, F. W., *Mechanics of Flight*, 2nd Edition, John Wiley & Sons, 2010.
- [19] Selig, S. M., "Modeling Full-Envelope Aerodynamics of Small UAVs in Realtime," AIAA Atmospheric Flight Mechanics Conference, Toronto, Ontario, 2010.
- [20] McCormick, B. W., *Aerodynamics, Aeronautics and Flight Mechanics*, 2nd Edition, John Wiley & Sons, 1995.
- [21] Katz, J., and Plotkin, A., *Low-Speed Aerodynamics*, 2nd Edition, Cambridge University Press, 2001.
- [22] Carlton, J. S., *Marine Propellers and Propulsion*, 2nd Edition, Butterworth-Heinemann, 2007.
- [23] Rankine, W. J. M., On the Mechanical Principles of the Action of Propellers, *Transaction of the Institute of Naval Architects*, Vol. 6, pp. 13-39, 1865.
- [24] van Kuik, G. A. M., "On the Limitations of Froude's Actuator Disk Concept," Ph.D. Dissertation, Technische Universiteit Eindhoven, 1991.
- [25] Froude, R. E., On the Part Played in Propulsion by Difference in Pressure, *Transaction of the Institute of Naval Architects*, Vol.30, pp. 390-423, 1889.
- [26] Sørensen, J. N., *General Momentum Theory for Horizontal Axis Wind Turbines*, 1st Edition, Springer, 2016.
- [27] Conway, J. T., "Exact actuator disk solutions for non-uniform heavy loading and slipstream contraction," *Journal of Fluid Mechanics*, Vol. 365, pp. 235-267, 1998.
- [28] Froude, W., On the Elementary Relation Between Pitch, Slip and Propulsion Efficiency, *Transaction of the Institute of Naval Architects*, Vol. 19, pp. 22-33, 1878.

REFERENCES (continued)

- [29] Goldstein, S., Prandtl, L., On the Vortex Theory of Screw Propellers, *Proceedings of Royal Society of London*, Vol. 123, No. 792, pp. 440-465, 1929.
- [30] Lerbs, H. W., Moderately Loaded Propellers with a Finite Number of Blades and an Arbitrary Distribution of Circulations, *Transactions – Society of Naval Architects and Marine Engineers*, Vol. 60, pp. 73-117, 1952.
- [31] Strscheletsky, M., *Hydrodynamische Grundlagen zur Berechnung der Schiffschrauben*, Braun, 1950.
- [32] Bertram, V., *Practical Ship Hydrodynamics*, Butterworth-Heinemann, 2011.
- [33] Agostinelli, A., Allen, C. B., and Simeone, S., “A Fast Approach to Model the Effects of Propeller Slipstream in Wing Load Distribution,” 53rd AIAA Aerospace Sciences Meeting, Florida, 2015.
- [34] Bohari, B., Bronz, M., Benard, E., and Borlon, Q., “Conceptual Design of Distributed Propeller Aircraft: Linear Aerodynamic Model Verification of Propeller-Wing Interaction,” 7th European Conference for Aeronautics and Aerospace Sciences (EUCASS), Milan, 2017.
- [35] Stone, R. H., “Aerodynamic Modeling of the Wing-Propeller Interaction for a Tail-Sitter Unmanned Air Vehicle,” *Journal of Aircraft*, Vol. 45, No. 1, pp. 198-210, 2008.
- [36] Kutty, H. A., and Rajendran, P., “3D CFD Simulation and Experimental Validation of Small APC Slow Flyer Propeller Blade,” *Aerospace*, Vol. 4, No. 1, 2017.
- [37] Joung, T., Choi, H., Jung, S., Sammut, K., and He, F., “Verification of CFD analysis methods for predicting the drag force and thrust power of an underwater disk robot,” *International Journal of Naval Architecture and Ocean Engineering*, Vol. 6, No. 2, pp. 269-281, 2014.
- [38] Stuermer, A., and Rakowitz, M., “Unsteady Simulation of a Transport Aircraft Propeller Using MEGAFLOW,” In Flow Induced Unsteady Loads and the Impact on Military Applications, Meeting Proceedings RTO-MP-AVT-123, Paper 7, France, 2005.
- [39] Roosenboom, E. W. M., Stürmer, A., and Schröder, A., “Advanced Experimental and Numerical Validation and Analysis of Propeller Slipstream Flows,” *Journal of Aircraft*, Vol. 47, No. 1, pp. 284-291, 2010.
- [40] Malki, R., Williams, A. J., Croft, T. N., Togneri, M., and Masters, I., “A Coupled Blade Element Momentum – Computational Fluid Dynamics Model for Evaluating Tidal Stream Turbine Performance,” *Applied Mathematical Modelling*, Vol. 37, No. 5, pp. 3006-3020, 2012.

REFERENCES (continued)

- [41] Stuhlpfarrer, M., Valero-Andreu, A., and Breitsamter, C., “Numerical and Experimental Investigations of the Propeller Characteristics of an Electrically Powered Ultralight Aircraft,” *CEAS Aeronautical Journal*, Vol. 8, No. 3, pp. 441-460, 2017.
- [42] Carroll, J., and Marcum, D., “Developing a Surrogate-Based Time-Averaged Momentum Source Model from 3D CFD simulations of Small Scale Propellers,” *Lecture Notes in Engineering and Computer Science: Proceedings of the World Congress of Engineering*, pp. 1622-1627, London, 2013.
- [43] Christina, S., Dimitris, M., and Kyros, Y., “Computational Flow Analysis and Development of a Surrogate Model for the Prediction of the Fluid Flow and the 3D Flow Effects Around a Propeller,” *8th GRACM International Congress on Computational Mechanics*, 2015.
- [44] Ying, Z., Liang, Y., Shuo, Y., and Xinglin, Z., “Investigation on Different Methods for Numerical Simulation of Propeller Slipstream,” *Asia-Pacific International Symposium on Aerospace Technology (APISAT)*, Shanghai, 2014.
- [45] Drela, M., “XFOIL: An Analysis and Design System for Low Reynolds Number Airfoils,” *Low Reynolds Number Aerodynamics*, edited by Mueller, T. J., Lecture Notes in Engineering, Springer–Verlag, Vol. 54, pp. 1-12, 1989.
- [46] Drela, M., and Giles, M. B., “Viscous-Inviscid Analysis of Transonic and Low Reynolds Number Airfoils,” *AIAA Journal*, Vol. 25, No.10, pp. 1347-1355, 1987.
- [47] Kaynak, Ü., Baş, O., Cakmakcioglu, S., and Tuncer, I., “Transition Modeling for Low to High Speed Boundary Layer Flows with CFD Applications,” Chapter in book: *Boundary Layer Flows - Theory, Applications and Numerical Methods* [Working Title]. DOI: 10.5772/intechopen.83520, 2019.
- [48] XFOIL 6.9 Documentation, URL: web.mit.edu/drela/Public/web/xfoil/xfoil_doc.txt [cited: May 8, 2019].
- [49] ANSYS Fluent (includes ANSYS CFD-Post), Release 18.2, Help System, Fluent Theory Guide, ANSYS, Inc.
- [50] Selig, M. S., and McGranahan, B. D., “Wind Tunnel Aerodynamic Tests of Six Airfoils for Use on Small Wind Turbines,” *ASME Journal of Solar Energy Engineering*, Vol. 126, No. 4, pp. 986-1001, 2004.
- [51] Cole, G. M., and Mueller, T. J., “Experimental Measurements of the Laminar Separation Bubble on an Eppler 387 Airfoil at Low Reynolds Numbers,” NASA-CR-186263, 1990.

REFERENCES (continued)

- [52] Tank, J., Smith, L., and Spedding, G, R., "On the possibility (or lack thereof) of agreement between experiment and computation of flows over wings at moderate Reynolds number," *Interface Focus*, Vol. 7, No. 1, 2016.
- [53] Abobaker, M., Petrovic, Z., Fotev, V., Toumi, N., and Ivanovix, I., "Aerodynamic Characteristics of Low Reynolds Number Airfoils," *Technical Gazette*, Vol. 24, No. 1, pp. 111-118, 2017.
- [54] Hansen, T., "Modeling the Performance of the Standard Cirrus Glider using Navier-Stokes CFD," *Technical Soaring*, Vol. 38, No. 1, 2014.
- [55] ANSYS Fluent (includes ANSYS CFD-Post), Release 18.2, Help System, CFD-Post User's Guide, ANSYS, Inc.
- [56] Khan, W., Caverly, R., and Nahon, M., "Propeller Slipstream Model for Small Unmanned Aerial Vehicles," AIAA Modeling and Simulation Technologies Conference, Boston, 2013.